Joint two-dimensional resummation in qT and 0-jettiness at NNLL

Lustermans, G.; Michel, J.K.L.; Tackmann, F.J.; Waalewijn, W.J.

DOI
10.1007/JHEP03(2019)124

Publication date
2019

Document Version
Final published version

Published in
Journal of High Energy Physics

Published for SISSA by Springer

Received: January 21, 2019
Accepted: March 14, 2019
Published: March 21, 2019

Joint two-dimensional resummation in q_T and 0-jettiness at NNLL

Gillian Lustermans,[a,b] **Johannes K.L. Michel,**[c] **Frank J. Tackmann**[c] **and Wouter J. Waalewijn**[a,b]

[a] *Institute for Theoretical Physics Amsterdam and Delta Institute for Theoretical Physics, University of Amsterdam, Science Park 904, 1098 XH Amsterdam, The Netherlands*

[b] *Nikhef, Theory Group, Science Park 105, 1098 XG, Amsterdam, The Netherlands*

[c] *Theory Group, Deutsches Elektronen-Synchrotron (DESY), D-22607 Hamburg, Germany*

E-mail: g.h.h.lustermans@uva.nl, johannes.michel@desy.de, frank.tackmann@desy.de, w.j.waalewijn@uva.nl

Abstract: We consider Drell-Yan production $pp \to Z/\gamma^* \to \ell^+\ell^-$ with the simultaneous measurement of the Z-boson transverse momentum q_T and 0-jettiness $\mathcal{T}_0$. Since both observables resolve the initial-state QCD radiation, the double-differential cross section in q_T and $\mathcal{T}_0$ contains Sudakov double logarithms of both q_T/Q and $\mathcal{T}_0/Q$, where $Q \sim m_Z$ is the dilepton invariant mass. We simultaneously resum the logarithms in q_T and $\mathcal{T}_0$ to next-to-next-to-leading logarithmic order (NNLL) matched to next-to-leading fixed order (NLO). Our results provide the first genuinely two-dimensional analytic Sudakov resummation for initial-state radiation. Integrating the resummed double-differential spectrum with an appropriate scale choice over either $\mathcal{T}_0$ or q_T recovers the corresponding single-differential resummation for the remaining variable. We discuss in detail the required effective field theory setups and their combination using two-dimensional resummation profile scales. We also introduce a new method to perform the q_T resummation where the underlying resummation is carried out in impact-parameter space, but is consistently turned off depending on the momentum-space target value for q_T. Our methods apply at any order and for any color-singlet production process, such that our results can be systematically extended when the relevant perturbative ingredients become available.

Keywords: QCD Phenomenology

ArXiv ePrint: 1901.03331

https://doi.org/10.1007/JHEP03(2019)124

JHEP03(2019)124

Contents

1 Introduction **1**

2 Resummation framework **4**
- 2.1 Overview of parametric regimes 4
- 2.2 SCET$_{\rm I}$: $\mathcal{T} \ll q_T \sim \sqrt{Q\mathcal{T}}$ 6
- 2.3 SCET$_{\rm II}$: $\mathcal{T} \sim q_T \ll \sqrt{Q\mathcal{T}}$ 10
- 2.4 SCET$_{+}$: $\mathcal{T} \ll q_T \ll \sqrt{Q\mathcal{T}}$ 16
- 2.5 Outer space 18

3 Matching effective theories **19**
- 3.1 Structure of power corrections 19
- 3.2 Matching formula 23
- 3.3 Profile scales 24
- 3.4 Perturbative uncertainties 28
- 3.5 Differential and cumulant scale setting 29

4 Results **35**
- 4.1 Double spectrum and comparison with boundary theories 36
- 4.2 Single-differential spectra with a cut on the other variable 41

5 Conclusions **42**

A Plus distributions and Fourier transform **43**

B Perturbative ingredients **45**
- B.1 Anomalous dimensions 45
- B.2 Fixed-order ingredients 48
- B.3 Renormalization-group evolution 51
- B.4 Beam function convolutions with RG kernels 51

1 Introduction

The increasing accuracy of measurements at the LHC places high demands on the precision and versatility of theoretical predictions. Fixed-order perturbation theory has proven to be a powerful tool to describe a large number of LHC processes, provided the measurement is sufficiently inclusive. With increasing data sets, however, more fine-grained measurements become possible and increasingly differential quantities come into focus. These more exclusive cross sections often involve several physical scales set by the hard interaction and the differential measurements or cuts applied on the final state. When these scales are

JHEP03(2019)124

widely separated, the perturbative series at each order is dominated by logarithms of their ratios. The resummation of these logarithms to all orders is crucial to arrive at the best possible predictions.

The resummation for measurements sensitive to infrared (soft and/or collinear) physics can, in part, be achieved through the use of parton-shower Monte Carlo event generators; popular examples include Pythia [1, 2], Herwig [3, 4], or Sherpa [5]. Parton showers provide fully exclusive final states so that in principle, any desired measurements or cuts can be imposed on the generated events. Existing implementations of parton showers are only formally accurate at about leading-logarithmic (LL) level, depending on the shower's evolution variable (and other implementation details) and the observable in question. (A recent detailed analysis can be found in ref. [6].) Furthermore, estimating the perturbative uncertainties of parton showers is challenging, which is in part due to their limited perturbative accuracy.

Analytic methods for the higher-order resummation of infrared-sensitive observables are available. These include the CSS formalism [7–9], seminumerical methods based on the coherent-branching formalism [10–13], and methods using renormalization group evolution (RGE) in effective field theories (EFTs) of QCD such as soft-collinear effective theory (SCET) [14–19]. The common drawback of analytic resummation methods is that they only apply after a sufficient amount of emissions have been integrated over, which is why they have been primarily used for the resummation of single-differential observables. Their crucial advantage is that they can be systematically extended to higher orders, and theoretical uncertainties can be addressed in a more reliable way.

There has been much progress in extending analytic resummation methods to cases involving multiple resummation variables. Examples include the joint resummation of transverse momentum q_T and threshold (large x) logarithms [20–26], q_T and small x [27], N-jettiness (or jet mass) together with dijet invariant masses [28, 29], two angularities [30, 31], jet mass and jet radius [32], jet vetoes and jet rapidity [33, 34], or threshold and jet radius in inclusive jet production [35, 36]. Most of these examples either involve different variables that effectively resolve different subsequent emissions, or involve a primary resummation variable that is modified by an auxiliary measurement or constraint. Another well-understood case is when an infrared-sensitive measurement is separated into its contributions from mutually exclusive regions of phase space [37–39].[1]

In contrast, here we are interested in resolving emissions at the same level by simultaneously measuring two independent infrared-sensitive observables. Extending analytic resummation to such genuinely multi-dimensional resolution variables is of key theoretical concern, as it allows for a more complete description of the emission pattern beyond LL, effectively filling a gap between analytic resummations and parton showers. So far, this has been achieved at NNLL for the case of simultaneously measuring two angularities in e^+e^- collisions [31].

[1] Yet another case, which will not be relevant here, arises when different infrared-sensitive measurements are performed in different regions of phase space, which may require the resummation of nonglobal logarithms [40–45].

JHEP03(2019)124

In this paper, we consider Drell-Yan, $pp \to Z/\gamma^* \to \ell^+\ell^-$, with a simultaneous measurement of (1) the transverse momentum q_T of the Drell-Yan lepton pair and (2) the hadronic resolution variable 0-jettiness $\mathcal{T} \equiv \mathcal{T}_0$ [46, 47]. Achieving their combined resummation is important conceptually because q_T and $\mathcal{T}$ are prototypes for two large classes of infrared-sensitive observables: q_T constrains the transverse momentum of initial-state radiation, while $\mathcal{T}$ constrains its virtuality. These different behaviors lead to very different logarithmic structures already at LL, which in SCET is reflected in the RGE structure of two distinct effective theories, SCET_I and SCET_II. (For parton showers, these correspond to evolution variables based on either transverse momentum or virtuality, respectively.)

Beyond providing a prototype for combining SCET_I and SCET_II resummations, the joint resummation of q_T and $\mathcal{T}$ is also of direct phenomenological interest. First, they are important variables individually. The measurement of $\mathcal{T}$ in bins of q_T [48] can probe the so-called underlying event in hadronic collisions. Furthermore, the GENEVA Monte Carlo event generator [49, 50] uses $\mathcal{T}$ as the underlying resolution variable for the event generation, achieving NNLL′+NNLO accuracy in $\mathcal{T}$ in conjunction with fully showered and hadronized events. While other observables, such as q_T, benefit from the underlying high resummation order, they do not enjoy the same level of formal accuracy in GENEVA as $\mathcal{T}$ itself. The joint resummation of $\mathcal{T}$ and q_T to a given order enables extending the event generation in GENEVA to also be accurate in q_T to the same order.

The double-differential factorization for q_T and $\mathcal{T}$ was first considered in ref. [51]. There, the regions of phase space where q_T (SCET_II) and $\mathcal{T}$ (SCET_I) determine the resummation structure were identified, together with the appropriate intermediate effective theory SCET_+ [28, 51] that connects them. Here, we develop an explicit matching procedure that combines the three different theories, SCET_I, SCET_+, and SCET_II, such that the resummation structure of each is recovered in its respective region of phase space. In particular, our method ensures that the single-differential resummation in one variable is recovered upon integration over the other. We discuss in detail the technical challenges involved. These include the construction of appropriate two-dimensional profile scales to combine the SCET_II resummation for q_T, which is performed in position (impact-parameter) space, with the SCET_I resummation for $\mathcal{T}$, which is performed in momentum space, the estimation of perturbative uncertainties, and the matching to full QCD at large q_T and/or $\mathcal{T}$ in a flexible way and consistent with the corresponding single-differential cases. We obtain explicit numerical predictions for the double-differential $(q_T, \mathcal{T})$ spectrum, achieving its complete and fully two-dimensional Sudakov resummation at NNLL+NLO. Our main result is shown in figure 1, featuring a nice two-dimensional Sudakov peak structure.

We like to stress that our methods are completely general and can be applied to any color-singlet production process and at any order for which the relevant perturbative ingredients are available. (Some of the double-differential ingredients required at NNLL′ and N^3LL are already known [52].) Furthermore, our matching procedure is generic and can be applied to any type of two-dimensional resummation for which the relevant EFTs on the boundaries and in the bulk are known.

The remainder of the paper is organized as follows. In section 2, we discuss the three different parametric regimes and the factorization and resummation for each individually.

JHEP03(2019)124

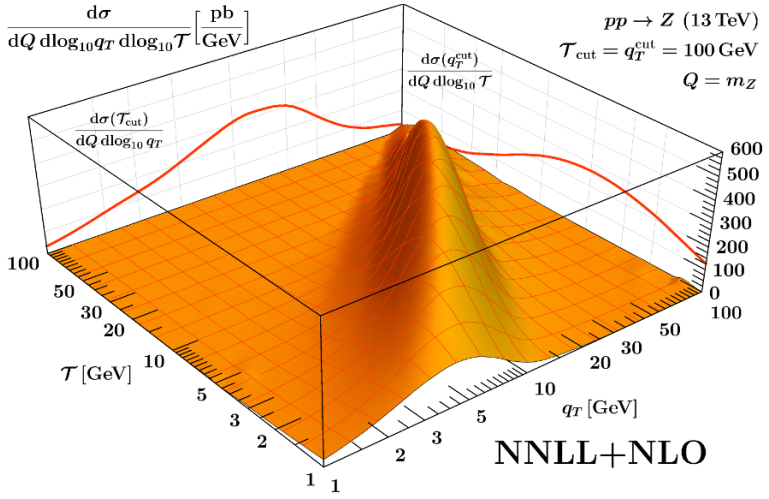

Figure 1. The Drell-Yan cross section double-differential in the transverse momentum q_T of the Z boson and the 0-jettiness event shape $\mathcal{T}$ at NNLL+NLO. For better visibility, the spectrum is plotted with respect to $\log_{10} q_T$ and $\log_{10} \mathcal{T}$. On the two side walls we show the corresponding single-differential spectra in q_T and $\mathcal{T}$ obtained by integrating the double-differential spectrum up to $\mathcal{T}_{\mathrm{cut}} = 100\,\mathrm{GeV}$ and $q_T^{\mathrm{cut}} = 100\,\mathrm{GeV}$, respectively.

In section 3, we then discuss in detail our method for consistently combining them to obtain a complete description of the two-dimensional $(q_T, \mathcal{T})$ plane. Our numerical results for the double-differential spectrum at NNLL+NLO are presented in section 4. We conclude in section 5. In appendix A we summarize our conventions for plus distributions and Fourier transforms. All required perturbative ingredients are collected in appendix B.

2 Resummation framework

2.1 Overview of parametric regimes

We consider color-singlet production at hadron colliders. Although the process dependence is not important for our discussion, we consider the example of Drell-Yan production, $pp \to Z/\gamma^*(\to \ell^+\ell^-)$, for concreteness. We measure the total invariant mass Q and rapidity Y of the color-singlet final state (the lepton pair). The two resolution variables we measure are the transverse momentum q_T of the color-singlet final state and the 0-jettiness $\mathcal{T}$ (aka beam thrust) [38, 46, 47, 53], defined as

$$\mathcal{T} \equiv \mathcal{T}_0 = \sum_i \min\left\{\frac{2q_a \cdot k_i}{Q_a}, \frac{2q_b \cdot k_i}{Q_b}\right\}. \tag{2.1}$$

The sum runs over all particles i with momentum k_i in the final state, excluding the color-singlet final state. We choose the massless reference momenta q_a and q_b as

$$q_a^\mu = \frac{Qe^{+Y}}{2} n_a^\mu, \qquad q_b^\mu = \frac{Qe^{-Y}}{2} n_b^\mu, \tag{2.2}$$

JHEP03(2019)124

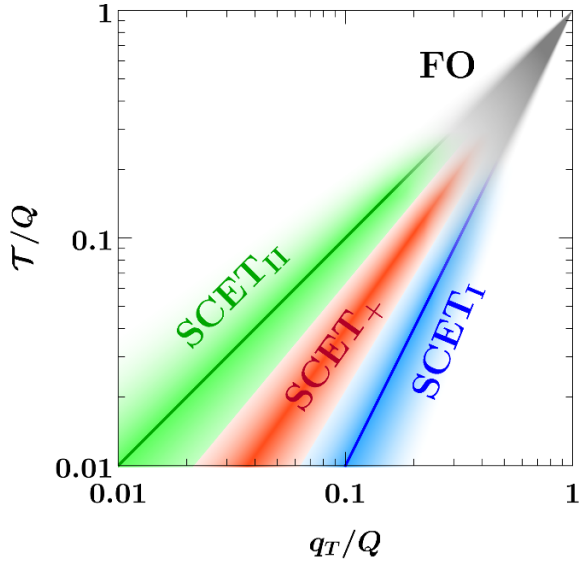

Figure 2. Parametric regimes in the $(q_T, \mathcal{T})$ plane and their SCET description. The solid lines correspond to the phase-space boundaries $q_T = \mathcal{T}$ (green) and $q_T = \sqrt{Q\mathcal{T}}$ (blue).

where $n_a^\mu = (1, +\hat{z})$ and $n_b^\mu = (1, -\hat{z})$ are lightlike vectors along the beam axis $\hat{z}$. For definiteness we use the leptonic definition of 0-jettiness for all numerical results in this paper, for which the measure factors $Q_{a,b}$ are simply given by

$$Q_a = Q_b = Q\,. \tag{2.3}$$

Our setup applies equally well to other definitions of $\mathcal{T}$, so we keep Q_a and Q_b (with $Q_a Q_b = Q^2$) generic for the rest of this section.

We are interested in the contribution of initial-state radiation (ISR) to the simultaneous measurement of $q_T, \mathcal{T} \ll Q$, where $Q \gg \Lambda_{\rm QCD}$ sets the scale of the hard interaction. The dynamics of perturbative ISR is then governed by three distinct momentum scales set by the measurement of q_T and $\mathcal{T}$. First, the typical transverse momentum of emissions that recoil against the lepton pair is set by q_T. Second, isotropic (soft) emissions at central rapidities can contribute to $\mathcal{T}$ via either of the projections onto q_a^μ and q_b^μ in eq. (2.1). This implies that their characteristic transverse momentum is $\sim \mathcal{T}$. Third, ISR with typical energy $\sim Q$ can contribute to $\mathcal{T}$ as long as it is collinear to either of the incoming beams, such that its contribution to $\mathcal{T}$ in eq. (2.1) is small. These collinear emissions then have a typical transverse momentum $\sim \sqrt{Q\mathcal{T}}$. The factorization and resummation structure of the cross section for $q_T, \mathcal{T} \ll Q$ depends on the parametric hierarchy between these scales. There are three relevant parametric regimes [51], which are illustrated in figure 2 and are discussed in the following.

In the first (blue) regime, $\mathcal{T} \ll q_T \sim \sqrt{Q\mathcal{T}}$, soft emissions with transverse momentum $\sim \mathcal{T}$ and collinear emissions with transverse momentum $\sim \sqrt{Q\mathcal{T}}$ both contribute to the $\mathcal{T}$ measurement. Due to the separation in transverse momentum, the q_T measurement is determined by collinear emissions, while soft emissions do not contribute to it. The

JHEP03(2019)124

appropriate EFT description for this regime is SCET_I. It has the same RG structure as the single-differential $\mathcal{T}$ spectrum, with q_T acting as an auxiliary variable. The SCET_I regime is discussed in more detail in section 2.2.

In the opposite (green) regime, $\mathcal{T} \sim q_T \ll \sqrt{Q\mathcal{T}}$, both soft and collinear emissions have transverse momentum $\sim q_T$ and thus contribute to q_T. On the other hand, only soft radiation at central rapidities contributes to $\mathcal{T}$, while the contribution from collinear radiation is suppressed. This regime is described by SCET_II, whose RG structure is analogous to that of the single-differential q_T spectrum, with $\mathcal{T}$ as the auxiliary variable. The SCET_II regime is discussed in more detail in section 2.3.

Third, the intermediate (orange) regime in the bulk, $\mathcal{T} \ll q_T \ll \sqrt{Q\mathcal{T}}$, shares features with both boundary cases. As in the SCET_I regime, central soft radiation contributes to $\mathcal{T}$, while as in the SCET_II regime, collinear radiation contributes to q_T. In addition, this regime requires a distinct collinear-soft mode at an intermediate rapidity scale that can contribute to both measurements [51]. The relevant EFT description is provided by SCET_+, which in this case shares elements of both SCET_I and SCET_II. The SCET_+ regime, as well as its relation to the regimes on the two boundaries, is discussed in section 2.4. We briefly comment on the regions beyond the phase-space boundaries (left blank in figure 2) in section 2.5.

All numerical results for the SCET predictions in the following are obtained from our implementation in `SCETlib` [54]. All fixed NLO results in full QCD are obtained from `MCFM 8.0` [55–57]. Throughout this paper we use `MMHT2014nnlo68cl` [58] NNLO PDFs with $\alpha_s(m_Z) = 0.118$ and five active quark flavors.

2.2 SCET_I: $\mathcal{T} \ll q_T \sim \sqrt{Q\mathcal{T}}$

In this regime, both soft and collinear modes are constrained by $\mathcal{T}$, while only collinear modes can contribute to q_T, whose characteristic transverse momentum $\sqrt{Q\mathcal{T}}$ coincides parametrically with q_T. The scaling of the relevant EFT modes reads

$$\begin{aligned} n_a\text{-collinear:} \quad & p^\mu \sim \left(\mathcal{T}, Q, \sqrt{Q\mathcal{T}}\right) \sim \left(\tfrac{q_T^2}{Q}, Q, q_T\right), \\ n_b\text{-collinear:} \quad & p^\mu \sim \left(Q, \mathcal{T}, \sqrt{Q\mathcal{T}}\right) \sim \left(Q, \tfrac{q_T^2}{Q}, q_T\right), \\ \text{soft:} \quad & p^\mu \sim \left(\mathcal{T}, \mathcal{T}, \mathcal{T}\right), \end{aligned} \tag{2.4}$$

in terms of lightcone coordinates defined by (with $n \equiv n_a$, $\bar{n} \equiv n_b$)

$$p^\mu = n{\cdot}p\,\frac{\bar{n}^\mu}{2} + \bar{n}{\cdot}p\,\frac{n^\mu}{2} + p_\perp^\mu \equiv (n{\cdot}p, \bar{n}{\cdot}p, p_\perp) \equiv (p^+, p^-, p_\perp)\,. \tag{2.5}$$

This leads to the following factorization formula for the cross section [46, 59],

$$\begin{aligned} \frac{\mathrm{d}\sigma_\text{I}}{\mathrm{d}Q\,\mathrm{d}Y\,\mathrm{d}q_T\,\mathrm{d}\mathcal{T}} = H_\kappa(Q,\mu) \int \mathrm{d}t_a \int \mathrm{d}^2\vec{k}_a\, B_a(t_a, x_a, \vec{k}_a, \mu) \int \mathrm{d}t_b \int \mathrm{d}^2\vec{k}_b\, B_b(t_b, x_b, \vec{k}_b, \mu) \\ \times \int \mathrm{d}k\, S_\kappa(k,\mu)\, \delta\big(q_T - |\vec{k}_a + \vec{k}_b|\big)\, \delta\left(\mathcal{T} - \frac{t_a}{Q_a} - \frac{t_b}{Q_b} - k\right), \end{aligned} \tag{2.6}$$

JHEP03(2019)124

which holds up to power corrections of the form[2]

$$\frac{\mathrm{d}\sigma}{\mathrm{d}Q\,\mathrm{d}Y\,\mathrm{d}q_T\,\mathrm{d}\mathcal{T}} = \frac{\mathrm{d}\sigma_{\mathrm{I}}}{\mathrm{d}Q\,\mathrm{d}Y\,\mathrm{d}q_T\,\mathrm{d}\mathcal{T}} \left[1 + \mathcal{O}\left(\frac{\mathcal{T}}{Q}, \frac{q_T^2}{Q^2}, \frac{\mathcal{T}^2}{q_T^2}\right)\right] . \tag{2.7}$$

The hard function $H_\kappa(Q,\mu)$ describes the short-distance scattering that produces the lepton pair through the off-shell γ^* or Z. In addition to Q, it depends on the partonic channel $\kappa \equiv \{a,b\}$, which is implicitly summed over all relevant combinations of quark and antiquark flavors a,b on the right-hand side of eq. (2.6). The beam functions $B_q(t,x,\vec{k}_T,\mu)$ describe extracting a quark (or antiquark) from the proton with momentum fraction x, virtuality t, and transverse momentum $\vec{k}_T$. The momentum fractions are directly related to Q and Y,

$$x_a = \frac{Q}{E_{\mathrm{cm}}}\, e^{+Y} , \qquad x_b = \frac{Q}{E_{\mathrm{cm}}}\, e^{-Y} . \tag{2.8}$$

The t and $\vec{k}_T$ encode the contribution of the collinear radiation to the $\mathcal{T}$ and q_T measurement, as captured by the measurement δ functions on the last line of eq. (2.6). For $t \sim k_T^2 \gg \Lambda^2_{\mathrm{QCD}}$, these beam functions can be matched onto PDFs [46, 59, 60],

$$B_q(t,x,\vec{k}_T,\mu) = \sum_j \int_x^1 \frac{\mathrm{d}z}{z}\, \mathcal{I}_{qj}(t,z,\vec{k}_T,\mu)\, f_j\Big(\frac{x}{z},\mu\Big) \left[1 + \mathcal{O}\left(\frac{\Lambda^2_{\mathrm{QCD}}}{t}, \frac{\Lambda^2_{\mathrm{QCD}}}{k_T^2}\right)\right] . \tag{2.9}$$

The soft function $S_\kappa(k,\mu)$ encodes the contribution from soft radiation to the 0-jettiness measurement, and depends on the color charge of the colliding partons.

The factorization in eq. (2.6) separates the physics at the canonical $\mathrm{SCET_I}$ scales

$$\mu_H^{\mathrm{I}} \sim Q , \qquad \mu_B^{\mathrm{I}} \sim \sqrt{Q\mathcal{T}} , \qquad \mu_S^{\mathrm{I}} \sim \mathcal{T} . \tag{2.10}$$

By evaluating the ingredients at their natural scale and evolving them to a common scale, all logarithms of $\mathcal{T}/Q \sim \mu_S^{\mathrm{I}}/\mu_H^{\mathrm{I}} \sim (\mu_B^{\mathrm{I}}/\mu_H^{\mathrm{I}})^2 \sim (\mu_S^{\mathrm{I}}/\mu_B^{\mathrm{I}})^2$ are resummed.

The hard and soft function in eq. (2.6) are the same as in the single-differential $\mathcal{T}$ spectrum and do not depend on q_T. The RG consistency of the cross section then implies that the RGE of the double-differential beam functions cannot depend on q_T, such that the overall RG structure of the cross section is equivalent to the single-differential case, i.e., q_T takes the role of an auxiliary measurement in the $\mathrm{SCET_I}$ resummation, with no large logarithms of q_T appearing in the cross section as long as $q_T \sim \sqrt{Q\mathcal{T}}$ is satisfied. We stress that eq. (2.6) nevertheless provides a nontrivial and genuinely double-differential extension of the single-differential case. This is already visible from the structure of power corrections in eq. (2.7). Furthermore, the q_T dependence does affect and is affected by the $\mathcal{T}$ resummation because the double-differential beam functions enter in a convolution with the beam and soft renormalization group kernels. Physically, they account for the total q_T recoil from all collinear emissions that are being resummed in $\mathcal{T}$.

The factorization of the double-differential spectrum in eq. (2.6) (and in the following sections) does not account for effects from Glauber gluon exchange. For active-parton

[2] Lorentz invariance suggests that power corrections in q_T always appear in terms of q_T^2. This distinction is irrelevant for our discussion.

JHEP03(2019)124

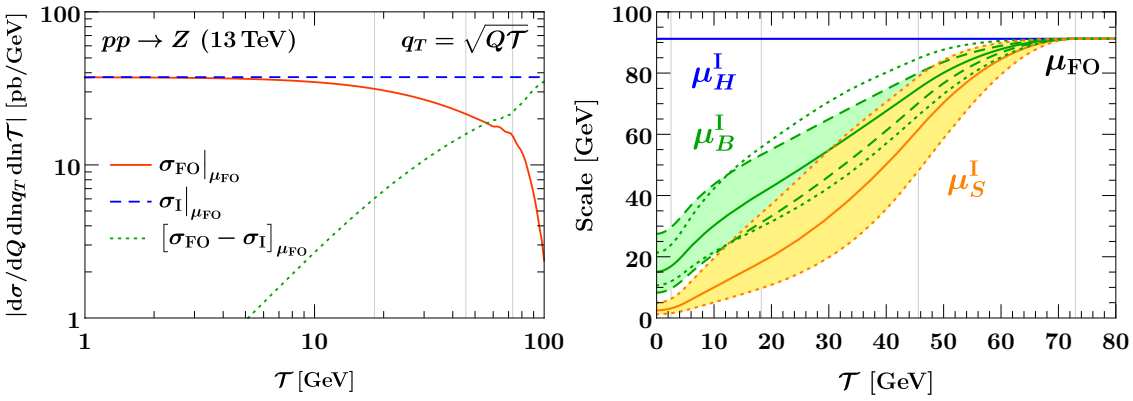

Figure 3. Left: comparison of singular and nonsingular contributions to the fixed $\mathcal{O}(\alpha_s)$ double spectrum as a function of $\mathcal{T}$, with $q_T = \sqrt{Q\mathcal{T}}$ kept fixed. The orange solid line shows the full QCD result and the dashed blue line the singular contributions contained in the $\mathrm{SCET_I}$ result eq. (2.6). The dotted green line shows their difference, which corresponds to the power corrections indicated in eq. (2.7). Right: $\mathrm{SCET_I}$ profile scales and their associated variations. The dotted lines (and the yellow band) indicate common up/down variations of $\mu_S^{\rm I}$ and $\mu_B^{\rm I}$ from varying α. The dashed lines (and the green band) are variations of β that only act on $\mu_B^{\rm I}$. In both plots, the thin vertical lines correspond to the transition points (x_0, x_1, x_2, x_3) given in the text.

scattering, they are expected to enter at $\mathcal{O}(\alpha_s^4)$ ($\mathrm{N^4LL'}$) [61, 62], which is well beyond the order we are interested in. They can be included using the Glauber operator framework of ref. [63]. For proton initial states the factorization formula also does not account for spectator forward scattering effects. Their complete treatment for the single-differential $\mathcal{T}$ spectrum is not yet available, but we expect that their treatment for the double-differential case would follow in a similar way.

Scale setting and fixed-order matching. To extend the description of the cross section to large $\mathcal{T} \sim q_T^2/Q \lesssim Q$, we have to reinstate the power corrections dropped in eq. (2.7). This is achieved by matching to the full fixed-order result, for which we use the standard additive matching,

$$\mathrm{d}\sigma_{\rm I}^{\rm match} = \mathrm{d}\sigma_{\rm I}\big|_{\mu^{\rm I}} + \big[\mathrm{d}\sigma_{\rm FO} - \mathrm{d}\sigma_{\rm I}\big]_{\mu_{\rm FO}}\,. \tag{2.11}$$

Here we abbreviated $\mathrm{d}\sigma \equiv \mathrm{d}\sigma/(\mathrm{d}Q\,\mathrm{d}Y\,\mathrm{d}q_T\,\mathrm{d}\mathcal{T})$, and $\mathrm{d}\sigma_{\rm FO}$ denotes the fixed-order cross section in full QCD. The scale subscripts on the right-hand side indicate whether $\mathrm{d}\sigma_{\rm I}$ is RG evolved using the $\mathrm{SCET_I}$ resummation scales $\mu^{\rm I}$, with their precise choices given below, or whether it is evaluated with all scales set to a common fixed-order scale $\mu_{\rm FO}$.

By construction, $\mathrm{d}\sigma_{\rm I}$ evaluated at common scales $\mu_{\rm FO}$ exactly reproduces the singular limit of $\mathrm{d}\sigma_{\rm FO}$, such that the term in square brackets in eq. (2.11) is a pure nonsingular power correction at small $\mathcal{T}$, which we can simply add to the resummed cross section. In the left panel of figure 3, we explicitly check that this is satisfied at fixed $\mathcal{O}(\alpha_s)$, and numerically assess the size of the power corrections. We compare the full QCD result (solid orange) to the $\mathrm{SCET_I}$ singular limit (dashed blue) as a function of $\mathcal{T}$, while keeping $q_T = \sqrt{Q\mathcal{T}}$ fixed

JHEP03(2019)124

to ensure that all classes of power corrections in eq. (2.7) uniformly vanish as $\mathcal{T} \to 0$. This is indeed satisfied, as the difference (dotted green) vanishes like a power.

For $\mathcal{T} \sim Q$, the SCET_I singular contribution and the power corrections are of the same size, implying that the resummation must be turned off to not upset the $\mathcal{O}(1)$ cancellation between them and correctly reproduce the fixed-order result. This is commonly achieved by using profile scales [64, 65], i.e., by having $\mu_B^\text{I} \equiv \mu_B^\text{I}(\mathcal{T})$ and $\mu_S^\text{I} \equiv \mu_S^\text{I}(\mathcal{T})$ transition from their canonical values eq. (2.10) at small $\mathcal{T}$ to a common high scale for large $\mathcal{T}$, schematically,

$$\mu_B^\text{I}(\mathcal{T}), \mu_S^\text{I}(\mathcal{T}) \to \mu_H^\text{I} = \mu_\text{FO} \quad \text{for} \quad \mathcal{T} \to Q\,. \tag{2.12}$$

As a result, the first and third term in eq. (2.11) exactly cancel in this limit, so the matched result reproduces $\mathrm{d}\sigma_\text{FO}$ as desired.

For the concrete choices of μ_B^I, μ_S^I we can rely on those used for the single-differential spectrum due to the equivalent RG structure. We use the profile scale setup developed for the closely related case of SCET_I-like jet vetoes in ref. [66] and used for the $\mathcal{T}$ resummation in GENEVA [50]. The profile scales are chosen as

$$\mu_S^\text{I} = \mu_\text{FO}\, f_\text{run}^\text{I}\left(\frac{\mathcal{T}}{Q}\right), \qquad \mu_B^\text{I} = \mu_\text{FO}\left[f_\text{run}^\text{I}\left(\frac{\mathcal{T}}{Q}\right)\right]^{1/2}, \qquad \mu_H^\text{I} = \mu_\text{FO}\,, \tag{2.13}$$

with the profile function f_run^I given by [67]

$$f_\text{run}^\text{I}(x) = \begin{cases} x_0\left(1+\frac{x^2}{4x_0^2}\right) & x \le 2x_0\,, \\ x & 2x_0 < x \le x_1\,, \\ x + \frac{(2-x_2-x_3)(x-x_1)^2}{2(x_2-x_1)(x_3-x_1)} & x_1 < x \le x_2\,, \\ 1 - \frac{(2-x_1-x_2)(x-x_3)^2}{2(x_3-x_1)(x_3-x_2)} & x_2 < x \le x_3\,, \\ 1 & x_3 < x\,. \end{cases} \tag{2.14}$$

Based on figure 3, we take $(x_1, x_2, x_3) = (0.2, 0.5, 0.8)$ for the transition points towards the fixed-order region $x \sim 1$. In addition, eq. (2.14) turns off the resummation in the nonperturbative region $x \lesssim 2x_0$, where we set $x_0 = 1\,\text{GeV}/Q$. This cuts off the nonperturbative region and ensures that RG running induced by perturbative anomalous dimensions always starts from a perturbative boundary condition. For μ_FO itself we use $\mu_\text{FO} = Q$ as the central scale. Our central scale choices are illustrated as solid lines in the right panel of figure 3.

Perturbative uncertainties. We estimate perturbative uncertainties in $\mathrm{d}\sigma_\text{I}^\text{match}$ by considering two different sources. The first uncertainty contribution Δ_I is inherent to the SCET_I resummation. It is estimated by varying the individual SCET_I scales while keeping μ_FO fixed, effectively probing the tower of higher-order logarithms that are being resummed. For this we use the profile scale variations [66]

$$\begin{aligned} \mu_S^\text{I} &= \mu_\text{FO}\left[f_\text{vary}\left(\frac{\mathcal{T}}{Q}\right)\right]^\alpha f_\text{run}^\text{I}\left(\frac{\mathcal{T}}{Q}\right), \\ \mu_B^\text{I} &= \mu_\text{FO}\left\{\left[f_\text{vary}\left(\frac{\mathcal{T}}{Q}\right)\right]^\alpha f_\text{run}^\text{I}\left(\frac{\mathcal{T}}{Q}\right)\right\}^{1/2-\beta}, \end{aligned} \tag{2.15}$$

JHEP03(2019)124

where $\alpha = \beta = 0$ corresponds to the central scale choice in eq. (2.13), and the variation factor is defined as

$$f_{\text{vary}}(x) = \begin{cases} 2(1 - x^2/x_3^2) & 0 \le x < x_3/2\,, \\ 1 + 2(1 - x/x_3)^2 & x_3/2 \le x < x_3\,, \\ 1 & x_3 \le x\,. \end{cases} \tag{2.16}$$

It approaches a factor of two in the resummation region at small x and reduces to unity toward the fixed-order regime at $x = x_3$, where the resummation is turned off. The estimate for Δ_{I} is obtained by computing $\mathrm{d}\sigma^{\text{I}}_{\text{match}}$ for each of the four profile scale variations

$$(\alpha, \beta) = \{(+1, 0), (-1, 0), (0, +1/6), (0, -1/6)\}\,, \tag{2.17}$$

and taking the maximum absolute deviation from the central result. These variations are also indicated in the right panel of figure 3. Note that for simplicity we do not perform explicit variations of the transition points since they are known to have a subdominant effect, and the uncertainty in the fixed-order matching is not essential to this paper.

For the second uncertainty contribution, Δ_{FO}, we consider common variations of μ_{FO} up and down by a factor of two in all pieces of eq. (2.11). Since μ_{FO} enters all μ^{I} scales as a common overall factor, they inherit the same variation, which keeps all resummed logarithms invariant. Hence, the μ_{FO} variation effectively probes the effect of missing higher-order corrections in the fixed-order contributions. The final uncertainty estimate for $\mathrm{d}\sigma^{\text{match}}_{\text{I}}$ is obtained by adding both contributions in quadrature,

$$\Delta^{\text{I}}_{\text{total}} = \Delta_{\text{I}} \oplus \Delta_{\text{FO}} \equiv \left(\Delta_{\text{I}}^2 + \Delta_{\text{FO}}^2\right)^{1/2}. \tag{2.18}$$

The matched result $\mathrm{d}\sigma^{\text{match}}_{\text{I}}$ in eq. (2.11) on its own constitutes a prediction for the double-differential spectrum that covers the part of phase space where $q_T \sim \sqrt{Q\mathcal{T}}$.

2.3 SCET$_{\text{II}}$: $\mathcal{T} \sim q_T \ll \sqrt{Q\mathcal{T}}$

In this regime, both soft and collinear emissions are constrained by q_T. Only soft radiation is constrained by the $\mathcal{T}$ measurement, while collinear radiation at transverse momenta $\sim q_T \ll \sqrt{Q\mathcal{T}}$ is not affected by it. The relevant EFT modes scale as

$$\begin{aligned} n_a\text{-collinear:} \quad & p^\mu \sim \left(\tfrac{q_T^2}{Q}, Q, q_T\right), \\ n_b\text{-collinear:} \quad & p^\mu \sim \left(Q, \tfrac{q_T^2}{Q}, q_T\right), \\ \text{soft:} \quad & p^\mu \sim \left(q_T, q_T, q_T\right) \sim \left(\mathcal{T}, \mathcal{T}, \mathcal{T}\right). \end{aligned} \tag{2.19}$$

In this case, the cross section factorizes as [51]

$$\begin{aligned} \frac{\mathrm{d}\sigma_{\text{II}}}{\mathrm{d}Q\,\mathrm{d}Y\,\mathrm{d}q_T\,\mathrm{d}\mathcal{T}} = H_\kappa(Q,\mu) \int \mathrm{d}^2\vec{k}_a\, B_a(\omega_a, \vec{k}_a, \mu, \nu) \int \mathrm{d}^2\vec{k}_b\, B_b(\omega_b, \vec{k}_b, \mu, \nu) \\ \times \int \mathrm{d}k \int \mathrm{d}^2\vec{k}_s\, S_\kappa(k, \vec{k}_s, \mu, \nu)\, \delta\big(q_T - |\vec{k}_a + \vec{k}_b + \vec{k}_s|\big)\, \delta\big(\mathcal{T} - k\big)\,. \end{aligned} \tag{2.20}$$

JHEP03(2019)124

The factorization receives power corrections of the form

$$\frac{\mathrm{d}\sigma}{\mathrm{d}Q\,\mathrm{d}Y\,\mathrm{d}q_T\,\mathrm{d}\mathcal{T}} = \frac{\mathrm{d}\sigma_{\mathrm{II}}}{\mathrm{d}Q\,\mathrm{d}Y\,\mathrm{d}q_T\,\mathrm{d}\mathcal{T}} \left[1 + \mathcal{O}\left(\frac{\mathcal{T}}{Q}, \frac{q_T^2}{\mathcal{T}Q}\right)\right] . \tag{2.21}$$

The hard function $H_\kappa(Q,\mu)$ is the same as in eq. (2.6). In $\mathrm{SCET_{II}}$ an additional regulator is required to handle rapidity divergences, for which we use the η regulator of refs. [68, 69] as implemented at two loops in ref. [70], with ν the corresponding rapidity renormalization scale. The $B_q(\omega, \vec{k}_T, \mu, \nu)$ are the same transverse momentum-dependent beam functions as in the single-differential q_T spectrum. The large momentum components ω in eq. (2.20) are given by

$$\omega_a = Qe^{+Y} = x_a E_{\mathrm{cm}} , \qquad \omega_b = Qe^{-Y} = x_b E_{\mathrm{cm}} , \tag{2.22}$$

and we suppress the trivial dependence of the beam function on E_{cm}. For $k_T^2 \gg \Lambda^2_{\mathrm{QCD}}$, the beam functions satisfy a matching relation similar to eq. (2.9) [69, 71–74],

$$B_q(\omega, \vec{k}_T, \mu, \nu) = \sum_j \int_x^1 \frac{\mathrm{d}z}{z}\, \mathcal{I}_{qj}(\omega, \vec{k}_T, z, \mu, \nu)\, f_j\left(\frac{\omega}{zE_{\mathrm{cm}}}, \mu\right) \left[1 + \mathcal{O}\left(\frac{\Lambda^2_{\mathrm{QCD}}}{k_T^2}\right)\right] . \tag{2.23}$$

The double-differential soft function $S_\kappa(k, \vec{k}_s, \mu, \nu)$ encodes the contribution of soft radiation to both $\mathcal{T}$ and q_T. The RG consistency of the cross section implies that its μ and ν RGEs do not depend on $\mathcal{T}$. Hence, the overall RG structure of the double-differential cross section is equivalent to the single-differential q_T spectrum, with $\mathcal{T}$ acting as an auxiliary measurement.

The factorization in eq. (2.20) separates the physics at the canonical $\mathrm{SCET_{II}}$ invariant-mass and rapidity scales

$$\begin{aligned} &\mu_H^{\mathrm{II}} \sim Q , \qquad \mu_B^{\mathrm{II}} \sim q_T , \qquad \mu_S^{\mathrm{II}} \sim q_T , \\ &\qquad\qquad \nu_B^{\mathrm{II}} \sim Q , \qquad \nu_S^{\mathrm{II}} \sim q_T . \end{aligned} \tag{2.24}$$

It has been known for a long time [75] that directly resumming the logarithms of q_T/Q in momentum space is challenging due to the vectorial nature of $\vec{q}_T$, though by now approaches for doing so exist [76, 77]. The same complications arise here for the double-differential spectrum. We bypass this issue, as is commonly done, by carrying out the resummation in conjugate (b_T) space [72, 78–80]. The Fourier transform from $\vec{q}_T$ to $\vec{b}_T$ turns the vectorial convolutions in eq. (2.20) into simple products at $b_T \equiv |\vec{b}_T|$. The canonical $\mathrm{SCET_{II}}$ scales in b_T-space are then given by

$$\begin{aligned} &\mu_H^{\mathrm{II}} \sim Q , \qquad \mu_B^{\mathrm{II}} \sim b_0/b_T , \qquad \mu_S^{\mathrm{II}} \sim b_0/b_T , \\ &\qquad\qquad \nu_B^{\mathrm{II}} \sim Q , \qquad \nu_S^{\mathrm{II}} \sim b_0/b_T , \end{aligned} \tag{2.25}$$

where $b_0 \equiv 2e^{-\gamma_E} \approx 1.12291$ is conventional. By evaluating the functions in the factorization theorem at their canonical scales and evolving them to a common scale in both μ and ν, all logarithms of $\mu_B/\mu_H \sim \mu_S/\mu_H \sim \nu_S/\nu_B \sim (b_0/b_T)/Q$ are resummed. In ref. [77] it

JHEP03(2019)124

was shown that the canonical resummation in b_T space is in fact equivalent to the exact solution of the RGE in momentum space, except for the fact that one effectively uses a shifted set of finite terms in the boundary conditions (similar to the difference between renormalization schemes). We exploit this and require that for $q_T \ll Q$, eq. (2.25) is exactly satisfied, such that the resummed q_T spectrum in this region is obtained from the inverse Fourier transform of the canonical b_T-space result.

A key feature of the resummed q_T spectrum is that the anomalous dimension γ_ν^i, driving the ν running of the soft (or beam) function at fixed μ, is itself perturbatively renormalized at its intrinsic scale μ_0 and requires resummation when $\mu_0 \neq \mu$. Specifically, in the exponent of the b_T-space rapidity evolution factor we have

$$\tilde{\gamma}_\nu^i(b_T, \mu) = -4\eta_\Gamma^i(\mu_0, \mu) + \tilde{\gamma}_{\nu,\mathrm{FO}}^i(b_T, \mu_0) + \tilde{\gamma}_{\nu,\mathrm{np}}^i(b_T)\,, \tag{2.26}$$

where all logarithms of μ/μ_0 are resummed inside

$$\eta_\Gamma^i(\mu_0, \mu) = \int_{\mu_0}^{\mu} \frac{\mathrm{d}\mu'}{\mu'}\, \Gamma_{\mathrm{cusp}}^i[\alpha_s(\mu')]\,. \tag{2.27}$$

[See eq. (4.26) in ref. [77] for the analogous expressions in momentum space.] The canonical choice of μ_0 that eliminates all large logarithms in the fixed-order boundary condition $\tilde{\gamma}_\nu^{\mathrm{FO}}(b_T, \mu_0)$ is

$$\mu_0 \sim b_0/b_T\,. \tag{2.28}$$

By choosing μ_0 as a function of b_T such that it freezes out to a perturbative value at large b_T, we avoid the Landau pole at $b_T \sim 1/\Lambda_{\mathrm{QCD}}$.[3] The mismatch to the full result can in principle be captured by a nonperturbative model $\tilde{\gamma}_{\nu,\mathrm{np}}^i(b_T)$, which can be extracted from experimental measurements at small q_T. Recently, it was shown that it could also be determined from lattice calculations [81]. For our purposes we set $\tilde{\gamma}_{\nu,\mathrm{np}}^i = 0$ for simplicity. (We similarly ignore nonperturbative effects in the $\mathrm{SCET_{II}}$ beam and soft function boundary conditions.) Our concrete choice of μ_0 is given below.

Scale setting and fixed-order matching. We again extend the description of the cross section to the fixed-order region $q_T \sim \mathcal{T} \lesssim Q$ by an additive matching,

$$\mathrm{d}\sigma_{\mathrm{II}}^{\mathrm{match}} = \mathrm{d}\sigma_{\mathrm{II}}\big|_{\mu^{\mathrm{II}}} + \big[\mathrm{d}\sigma_{\mathrm{FO}} - \mathrm{d}\sigma_{\mathrm{II}}\big]_{\mu_{\mathrm{FO}}}\,. \tag{2.29}$$

Here the subscript μ^{II} indicates that we evaluate $\mathrm{d}\sigma_{\mathrm{II}}$ at the $\mathrm{SCET_{II}}$ resummation scales μ^{II} (given below) in b_T space, and take a numerical inverse Fourier transform in the end. The subscript μ_{FO} indicates that it is instead evaluated at common fixed-order scales μ_{FO}, which can be done directly in momentum space.

Analogous to the discussion for $\mathrm{SCET_I}$, the term in square brackets in eq. (2.29) is by construction a pure nonsingular power correction at small q_T. This is illustrated in the left panel of figure 4, which shows that the difference (green dotted) between the full QCD

[3] In addition, this leaves fixed-order logarithms of $\mu_0 b_T$ in $\tilde{\gamma}_{\nu,\mathrm{FO}}^i$ that lead to an exponential suppression of the b_T space cross section as $b_T \to \infty$. This increases the numerical stability of the inverse Fourier transform.

JHEP03(2019)124

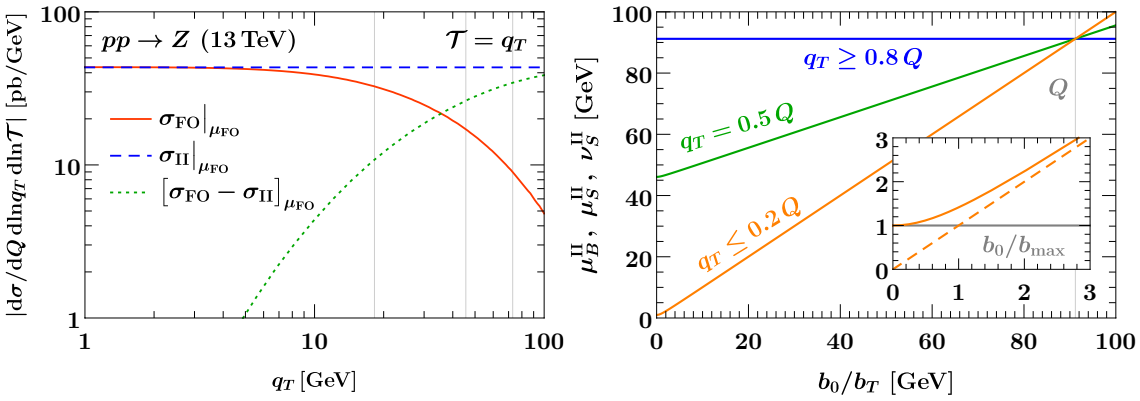

Figure 4. Left: comparison of singular and nonsingular contributions to the fixed $\mathcal{O}(\alpha_s)$ double spectrum as a function of q_T, with $\mathcal{T} = q_T$ kept fixed. The orange solid line shows the full QCD result and the dashed blue line the singular contributions contained in the $\mathrm{SCET_{II}}$ result eq. (2.20). The dotted green line shows their difference, which corresponds to the power corrections indicated in eq. (2.21). The thin vertical lines correspond to the transition points (x_1, x_2, x_3) given in the text. Right: $\mathrm{SCET_{II}}$ hybrid profile scales as a function of b_0/b_T for representative values of q_T. The thin vertical line in the main plot corresponds to Q. The inset shows the behavior of the profile in the nonperturbative region $b_0/b_T \sim \Lambda_{\rm QCD}$, where the gray horizontal line indicates the scale $b_0/b_{\rm max}$ at which we freeze out the resummation. The dashed orange line in the inset indicates the canonical value of $\mu_B^{\rm II}, \mu_S^{\rm II}, \nu_S^{\rm II}$.

result (solid orange) and the $\mathrm{SCET_{II}}$ singular result (dashed blue) indeed vanishes like a power as $q_T \to 0$ along the line of fixed $\mathcal{T} = q_T$.

Approaching $q_T \sim \mathcal{T} \sim Q$, the q_T resummation must again be turned off to ensure the delicate cancellations between singular and nonsingular contributions and to properly recover the correct fixed-order result for the spectrum. We achieve this by constructing hybrid profile scales that depend on both b_T and q_T, and undergo a continuous deformation away from the canonical b_T scales in eq. (2.24) as a function of the target q_T value, schematically,

$$\mu_{B,S}^{\rm II}(q_T, b_T)\,, \nu_{B,S}^{\rm II}(q_T, b_T) \to \mu_H^{\rm II} = \mu_{\rm FO} \quad \text{for} \quad q_T \to Q\,. \tag{2.30}$$

We note that μ_0 does not need to asymptote to $\mu_{\rm FO}$ towards large q_T because its effect on the matched result is already turned off as $\nu_S^{\rm II} \to \nu_B^{\rm II}$. In this limit, the first and last term in eq. (2.29) exactly cancel, leaving the fixed-order result $\mathrm{d}\sigma_{\rm FO}$.

Since the single-differential q_T resummation is not the main focus of this paper, we strive to achieve eq. (2.30) in the simplest possible way. Specifically, we choose central scales as

$$\mu_H^{\rm II} = \nu_B^{\rm II} = \mu_{\rm FO}\,, \quad \mu_B^{\rm II} = \mu_S^{\rm II} = \nu_S^{\rm II} = \mu_{\rm FO}\, f_{\rm run}^{\rm II}\left(\frac{q_T}{Q}, \frac{b_0}{b^*(b_T)\,Q}\right), \quad \mu_0 = \frac{b_0}{b^*(b_T)}\,, \tag{2.31}$$

where $f_{\rm run}^{\rm II}$ is a hybrid profile function given by

$$f_{\rm run}^{\rm II}(x, y) = 1 + g_{\rm run}(x)(y - 1)\,. \tag{2.32}$$

JHEP03(2019)124

It controls the amount of resummation by adjusting the slope of the scales in b_T space as a function of q_T/Q via the function

$$g_{\text{run}}(x) = \begin{cases} 1 & 0 < x \leq x_1\,, \\ 1 - \frac{(x-x_1)^2}{(x_2-x_1)(x_3-x_1)} & x_1 < x \leq x_2\,, \\ \frac{(x-x_3)^2}{(x_3-x_1)(x_3-x_2)} & x_2 < x \leq x_3\,, \\ 0 & x_3 \leq x\,. \end{cases} \tag{2.33}$$

As a result, for $q_T \leq x_1 Q$, the slope is unity yielding the canonical resummation, while for $q_T \geq x_3 Q$, the slope vanishes so the resummation is fully turned off. In between, the slope smoothly transitions from one to zero, which transitions the resummation from being canonical to being turned off. This is illustrated in the right panel of figure 4. We use the same transition points $(x_1, x_2, x_3) = (0.2, 0.5, 0.8)$ as for SCET_I, which is supported by figure 4.

We note that our approach differs from the hybrid profile scales introduced in ref. [82]. While the latter also satisfy the requirement in eq. (2.30), they do not reproduce the exact canonical b_T-space scales for $q_T \ll Q$ because they introduce a profile shape directly in b_T space.

As discussed below eq. (2.28), we require a nonperturbative prescription when the canonical value of μ_0 (or μ_S^{II}, or μ_B^{II}) approaches the Landau pole $b_0/b_T \sim \Lambda_{\text{QCD}}$. This is encoded in evaluating the hybrid scales at $b^*(b_T)$ rather than b_T itself,

$$b^*(b_T) = \frac{b_T}{\sqrt{1 + b_T^2/b_{\text{max}}^2}}\,, \tag{2.34}$$

where $b_0/b_{\text{max}} \gtrsim \Lambda_{\text{QCD}}$ ensures that all scales are canonical for small $b_T \approx b^*$, but remain perturbative for large b_T where $b^* \to b_{\text{max}}$, as shown in the inset in the right panel of figure 4. In practice we pick

$$b_0/b_{\text{max}} = 1\,\text{GeV}\,, \tag{2.35}$$

in keeping with our choice of nonperturbative turn-off parameter in the SCET_I case. The functional form of eq. (2.34) is the same as in the standard b^* prescription [79, 80], although any other functional form with the same asymptotic behavior is also viable. We stress, however, that a key difference in our case is that b^* only affects the scales, so it essentially serves the same purpose as the x_0 nonperturbative cutoff in the SCET_I scales in eq. (2.14). By contrast, the standard b^* prescription corresponds to a *global* replacement of b_T by b^*, including the measurement itself. For the single-differential q_T spectrum, this global replacement induces power corrections $\mathcal{O}(b_T^2/b_{\text{max}}^2)$ that scale like a generic nonperturbative contribution. While they might complicate the extraction of nonperturbative model parameters from data [83], they are not a critical issue.

For the double-differential case, we find that a standard b^* prescription does in fact not work. This is because substituting b^* for b_T in the physical measurement renders Fourier integrals of the double-differential SCET_II soft function divergent, at least at fixed order (i.e., without Sudakov suppression). This can be seen from eqs. (B.40) and (B.41), which

JHEP03(2019)124

only depend on $x = b_T\mathcal{T}$. Substituting b^* for b_T makes them asymptote to a constant for any given $\mathcal{T}$, which upsets their required asymptotic behavior $\sim 1/x^2$. Physically this means that the deformation of the measurement at large b_T also deforms the observable of interest, i.e., the dependence on $\mathcal{T}$.

Perturbative uncertainties. To estimate the resummation uncertainty for $\mathrm{d}\sigma_{\mathrm{II}}^{\mathrm{match}}$, we adopt the set of profile scale variations introduced for the $\mathrm{SCET}_{\mathrm{II}}$-like jet veto in ref. [67]. They are given by

$$\begin{aligned}
\mu_S^{\mathrm{II}} &= \mu_{\mathrm{FO}} \left[f_{\mathrm{vary}}\Big(\frac{q_T}{Q}\Big)\right]^{v_{\mu_S}} f_{\mathrm{run}}^{\mathrm{II}}\Big(\frac{q_T}{Q}, \frac{b_0}{b^*Q}\Big)\,,\\
\nu_S^{\mathrm{II}} &= \mu_{\mathrm{FO}} \left[f_{\mathrm{vary}}\Big(\frac{q_T}{Q}\Big)\right]^{v_{\nu_S}} f_{\mathrm{run}}^{\mathrm{II}}\Big(\frac{q_T}{Q}, \frac{b_0}{b^*Q}\Big)\,,\\
\mu_B^{\mathrm{II}} &= \mu_{\mathrm{FO}} \left[f_{\mathrm{vary}}\Big(\frac{q_T}{Q}\Big)\right]^{v_{\mu_B}} f_{\mathrm{run}}^{\mathrm{II}}\Big(\frac{q_T}{Q}, \frac{b_0}{b^*Q}\Big)\,,\\
\nu_B^{\mathrm{II}} &= \mu_{\mathrm{FO}} \left[f_{\mathrm{vary}}\Big(\frac{q_T}{Q}\Big)\right]^{v_{\nu_B}}\,,
\end{aligned} \tag{2.36}$$

where each of the four variation exponents can be $v_i = \{+1, 0, -1\}$, and f_{vary} was given in eq. (2.16). The central scale choice corresponds to $(v_{\mu_S}, v_{\nu_S}, v_{\mu_B}, v_{\nu_B}) = (0, 0, 0, 0)$, and a priori there are 80 possible different combinations of the v_i. Since the arguments of the resummed logarithms are ratios of scales, some combinations of scale variations will lead to variations of these arguments that are larger than a factor of two, and therefore should be excluded [67]. After dropping these combinations we are left with 36 different scale variations for the $\mathrm{SCET}_{\mathrm{II}}$ regime. We add two independent variations of $b_0/b_{\max} = \{0.5\,\mathrm{GeV}, 2\,\mathrm{GeV}\}$ to probe the uncertainty in our nonperturbative prescription. The $\mathrm{SCET}_{\mathrm{II}}$ resummation uncertainty Δ_{II} is then determined as the maximum absolute deviation from the central result among all 38 variations. For simplicity we again refrain from variations of the transition points. As for $\mathrm{SCET}_{\mathrm{I}}$, Δ_{FO} is estimated by overall variations of μ_{FO} by a factor of two, which is inherited by all $\mathrm{SCET}_{\mathrm{II}}$ scales, so it probes the fixed-order uncertainties while leaving the resummed logarithms invariant. The total uncertainty estimate for $\mathrm{d}\sigma_{\mathrm{II}}^{\mathrm{match}}$ is then obtained as

$$\Delta_{\mathrm{total}}^{\mathrm{II}} = \Delta_{\mathrm{II}} \oplus \Delta_{\mathrm{FO}}\,. \tag{2.37}$$

The matched result $\mathrm{d}\sigma_{\mathrm{II}}^{\mathrm{match}}$ in eq. (2.29) provides a prediction for the double-differential spectrum that covers the part of phase space where $\mathcal{T} \sim q_T$.

Results for the single-differential spectrum. Since we are using a new method to perform the q_T resummation, we also briefly consider the single-differential q_T spectrum as a sanity check of our setup. The setup described in this section immediately carries over to the single-differential spectrum. In figure 5 we show the q_T spectrum at the NNLL+NLO order we are aiming for for the double-differential spectrum, as well as one order lower at NLL, and with the uncertainties estimated as described above. The results look very reasonable, providing us with confidence in our q_T resummation procedure. Note that there is a slight pinch in the uncertainty bands around $q_T = 15\,\mathrm{GeV}$, indicating that the uncertainties there are likely a bit underestimated. This is an artifact of scale variations that is not unusual to be seen in resummed spectrum predictions.

JHEP03(2019)124

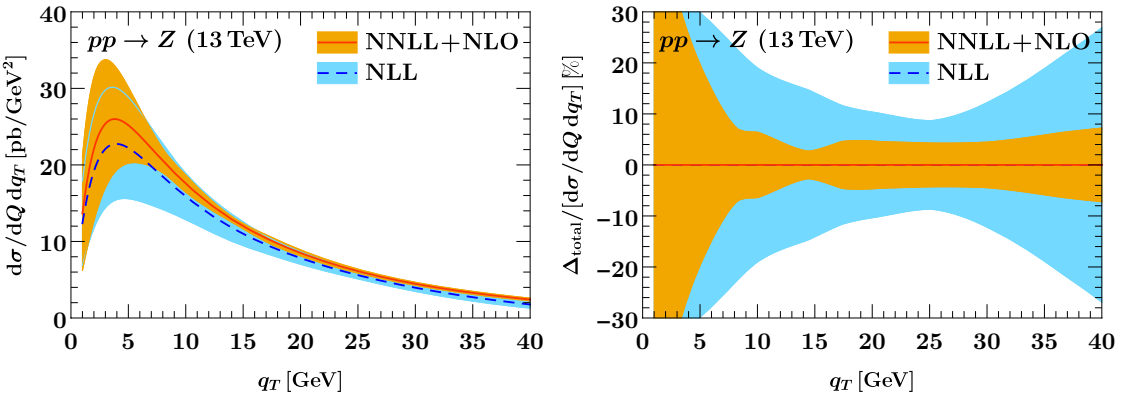

Figure 5. The single-differential q_T spectrum at NLL (blue) and NNLL+NLO (orange), using the q_T resummation method described in the text. The bands indicate $\Delta_{\mathrm{II}} \oplus \Delta_{\mathrm{FO}}$. In the right panel, the uncertainties are shown as percent differences relative to the central result at each order.

2.4 SCET$_+$: $\mathcal{T} \ll q_T \ll \sqrt{Q\mathcal{T}}$

This regime is characterized by the presence of intermediate collinear-soft modes that contribute both to the q_T and the $\mathcal{T}$ measurement, which uniquely fixes their scaling. Central soft modes only contribute to $\mathcal{T}$ as in SCET$_{\mathrm{I}}$, while the energetic collinear modes only contribute to q_T as in SCET$_{\mathrm{II}}$,

$$\begin{aligned}
&n_a\text{-collinear:} \quad p^\mu \sim \Big(\tfrac{q_T^2}{Q}, Q, q_T\Big), && n_a\text{-collinear-soft:} \quad p^\mu \sim \Big(\mathcal{T}, \tfrac{q_T^2}{\mathcal{T}}, q_T\Big),\\
&n_b\text{-collinear:} \quad p^\mu \sim \Big(Q, \tfrac{q_T^2}{Q}, q_T\Big), && n_b\text{-collinear-soft:} \quad p^\mu \sim \Big(\tfrac{q_T^2}{\mathcal{T}}, \mathcal{T}, q_T\Big),\\
&\text{soft:} \quad p^\mu \sim \Big(\mathcal{T}, \mathcal{T}, \mathcal{T}\Big).
\end{aligned} \tag{2.38}$$

The collinear-soft modes have the same virtuality as the collinear modes, $p^2 \sim q_T^2$, but live at more central rapidity $e^{|y|} \sim q_T/\mathcal{T}$, which is small compared to the rapidity $e^{|y|} \sim Q/q_T$ of the collinear modes. Hence, the two have a SCET$_{\mathrm{II}}$-like relation and become a single collinear mode in the SCET$_{\mathrm{I}}$ limit $q_T \sim \sqrt{Q\mathcal{T}}$. At the same time, the collinear-soft and soft modes have a SCET$_{\mathrm{I}}$-like relation, being separated in virtuality, and become a single soft mode in the SCET$_{\mathrm{II}}$ limit $\mathcal{T} \sim q_T$. In this way, SCET$_+$ is able to connect the SCET$_{\mathrm{I}}$ and SCET$_{\mathrm{II}}$ regimes. This is similar to the collinear-soft mode originally introduced in ref. [28], which instead connected two SCET$_{\mathrm{I}}$ theories.

The cross section in SCET$_+$ factorizes as [51]

$$\begin{aligned}
\frac{\mathrm{d}\sigma_+}{\mathrm{d}Q\,\mathrm{d}Y\,\mathrm{d}q_T\,\mathrm{d}\mathcal{T}} &= H_\kappa(Q,\mu) \int \mathrm{d}^2\vec{k}_a\, B_a(\omega_a, \vec{k}_a, \mu, \nu) \int \mathrm{d}^2\vec{k}_b\, B_b(\omega_b, \vec{k}_b, \mu, \nu)\\
&\times \int \mathrm{d}\ell_a^+ \int \mathrm{d}^2\vec{\ell}_a\, \mathcal{S}_\kappa(\ell_a^+, \vec{\ell}_a, \mu, \nu) \int \mathrm{d}\ell_b^- \int \mathrm{d}^2\vec{\ell}_b\, \mathcal{S}_\kappa(\ell_b^-, \vec{\ell}_b, \mu, \nu)\\
&\times \int \mathrm{d}k\, S_\kappa(k,\mu)\, \delta\big(q_T - |\vec{k}_a + \vec{k}_b + \vec{\ell}_a + \vec{\ell}_b|\big)\, \delta\left(\mathcal{T} - \frac{\omega_a \ell_a^+}{Q_a} - \frac{\omega_b \ell_b^-}{Q_b} - k\right),
\end{aligned} \tag{2.39}$$

JHEP03(2019)124

which holds up to power corrections

$$\frac{\mathrm{d}\sigma}{\mathrm{d}Q\,\mathrm{d}Y\,\mathrm{d}q_T\,\mathrm{d}\mathcal{T}} = \frac{\mathrm{d}\sigma_+}{\mathrm{d}Q\,\mathrm{d}Y\,\mathrm{d}q_T\,\mathrm{d}\mathcal{T}} \left[1 + \mathcal{O}\left(\frac{q_T^2}{\mathcal{T}Q}, \frac{\mathcal{T}^2}{q_T^2}\right)\right] . \tag{2.40}$$

The hard function is the same as before. The beam functions are the q_T-dependent ones from $\mathrm{SCET_{II}}$, while the soft function is the $\mathcal{T}$-dependent one from $\mathrm{SCET_I}$. The new ingredient is the double-differential collinear-soft function $\mathcal{S}_\kappa(k, \vec{k}_T, \mu, \nu)$, which encodes the contributions of the collinear-soft modes to both q_T and $\mathcal{T}$. Like the soft function it is defined as a matrix element of eikonal Wilson lines, but like the beam functions it describes radiation that goes into a definite hemisphere.

Equation (2.39) can be interpreted as a refactorization of the double-differential $\mathrm{SCET_I}$ and $\mathrm{SCET_{II}}$ cross sections [51], which precisely reflects the relation between the EFT modes described above. Expanding the $\mathrm{SCET_I}$ double-differential beam function in the limit $q_T \ll \sqrt{Q\mathcal{T}}$, it factorizes into the $\mathrm{SCET_{II}}$ beam function and the collinear-soft function,

$$B_q(\omega k, \omega E_{\mathrm{cm}}, \vec{k}_T, \mu) = \int \mathrm{d}^2\vec{\ell}_T\, B_q(\omega, \vec{k}_T - \vec{\ell}_T, \mu, \nu)\, \mathcal{S}_\kappa(k, \vec{\ell}_T, \mu, \nu) \left[1 + \mathcal{O}\left(\frac{k_T^2}{\omega k}\right)\right] . \tag{2.41}$$

The ν dependence of the two terms on the right-hand side must cancel, while their μ dependence must combine into that of the left-hand side. This allows us to derive the RGE for the collinear-soft function given in eq. (B.18).

Similarly, expanding the $\mathrm{SCET_{II}}$ double-differential soft function in the limit $\mathcal{T} \ll q_T$, it factorizes into the $\mathrm{SCET_I}$ soft function and the two n_a-collinear-soft and n_b-collinear-soft functions,

$$\begin{aligned} S_\kappa(k, \vec{k}_T, \mu, \nu) = \int \mathrm{d}^2\vec{\ell}_T \int \mathrm{d}\ell_a^+\, \mathcal{S}_\kappa(\ell_a^+, \vec{\ell}_T, \mu, \nu) \int \mathrm{d}\ell_b^-\, \mathcal{S}_\kappa(\ell_b^-, \vec{k}_T - \vec{\ell}_T, \mu, \nu) \\ \times S_\kappa\left(k - \frac{\omega_a \ell_a^+}{Q_a} - \frac{\omega_b \ell_b^-}{Q_b}\right) \left[1 + \mathcal{O}\left(\frac{k^2}{k_T^2}\right)\right] . \end{aligned} \tag{2.42}$$

Since the left-hand side does not depend on $\omega_{a,b}$ and $Q_{a,b}$, this dependence must also drop out on the right-hand side, and therefore in the whole $\mathrm{SCET_+}$ cross section in eq. (2.39). To see this explicitly, first recall that $\omega_a \omega_b = Q_a Q_b = Q^2$. In addition, boost invariance at the level of the collinear-soft matrix element implies that $\mathrm{d}\ell_a^+\, \mathcal{S}_\kappa(\ell_a^+, \vec{k}_T, \mu, \nu)$ can only depend on the product $\ell_a^+ \nu$ (and analogously for ℓ_b^-).[4] Hence, we can rewrite

$$\begin{aligned} &\mathrm{d}\ell_a^+\, \mathcal{S}_\kappa(\ell_a^+, \vec{\ell}_a, \mu, \nu)\, \mathrm{d}\ell_b^-\, \mathcal{S}_\kappa(\ell_b^-, \vec{\ell}_b, \mu, \nu)\, \delta\left(\mathcal{T} - \frac{\omega_a \ell_a^+}{Q_a} - \frac{\omega_b \ell_b^-}{Q_b} - k\right) \\ &\quad = \mathrm{d}k_a^+\, \mathcal{S}_\kappa\left(k_a^+, \vec{\ell}_a, \mu, \frac{Q_a \nu}{\omega_a}\right) \mathrm{d}k_b^-\, \mathcal{S}_\kappa\left(k_b^-, \vec{\ell}_b, \mu, \frac{Q_b \nu}{\omega_b}\right) \delta(\mathcal{T} - k_a^+ - k_b^- - k) \\ &\quad = \mathrm{d}k_a^+\, \mathcal{S}_\kappa(k_a^+, \vec{\ell}_a, \mu, \nu)\, \mathrm{d}k_b^-\, \mathcal{S}_\kappa(k_b^-, \vec{\ell}_b, \mu, \nu)\, \delta(\mathcal{T} - k_a^+ - k_b^- - k) , \end{aligned} \tag{2.43}$$

[4] More explicitly, the rapidity regulator breaks the RPI-III invariance of SCET [84, 85], which is equivalent to boost invariance that must hold separately in each collinear sector. To restore it, ν must transform under RPI-III like $\bar{n} \cdot p$ in each n-collinear-soft sector. This is most straightforward to see when strictly expanding the rapidity regulator to leading power in $\mathcal{T}^2/q_T^2$ using the soft-collinear mode scaling in eq. (2.38). The RPI-III transformation of the explicit measurement δ function in the matrix element is canceled by the corresponding integration measure in eqs. (2.39) and (2.42). Therefore, RPI-III invariance implies that each collinear-soft function can only depend on the RPI-III invariant combination $\nu\, n \cdot k$.

JHEP03(2019)124

where in the first step we changed variables from $\ell^{\pm}_{a,b}$ to $k^+_a = \omega_a \ell^+_a / Q_a$ and $k^-_b = \omega_b \ell^-_b / Q_b$. In the second step we performed the rapidity evolution from $\nu_{a,b} \equiv Q_{a,b}\,\nu/\omega_{a,b}$ back to a common ν at fixed μ [see eq. (B.46)], for which the rapidity evolution factors exactly cancel because

$$\ln \frac{\nu_a}{\nu} + \ln \frac{\nu_b}{\nu} = \ln \frac{Q_a Q_b}{\omega_a \omega_b} = 0\,. \tag{2.44}$$

The SCET_+ factorization in eq. (2.39) fully disentangles the physics at the following SCET_+ canonical energy and rapidity scales:

$$\begin{aligned} &\mu_H^+ \sim Q\,, \qquad \mu_B^+ \sim q_T\,, \qquad \mu_S^+ \sim q_T\,, \qquad \mu_S^+ \sim \mathcal{T}\,, \\ &\qquad\qquad \nu_B^+ \sim Q\,, \qquad \nu_S^+ \sim q_T^2/\mathcal{T}\,. \end{aligned} \tag{2.45}$$

As for SCET_{II}, we perform the q_T resummation in b_T space, transforming the vectorial convolutions in eq. (2.39) into simple products. In b_T space, the canonical SCET_+ scales are

$$\begin{aligned} &\mu_H^+ \sim Q\,, \qquad \mu_B^+ \sim b_0/b_T\,, \qquad \mu_S^+ \sim b_0/b_T\,, \qquad \mu_S^+ \sim \mathcal{T}\,, \\ &\qquad\qquad \nu_B^+ \sim Q\,, \qquad \nu_S^+ \sim (b_0/b_T)^2/\mathcal{T}\,. \end{aligned} \tag{2.46}$$

By evaluating all functions at their natural scales and evolving them to common scales, all logarithms of large scale ratios in the problem are resummed, e.g.,

$$\frac{(b_0/b_T)^2}{Q\mathcal{T}} \sim \frac{\nu_S^+}{\nu_B^+}\,, \qquad \frac{\mathcal{T}}{b_0/b_T} \sim \frac{\mu_S^+}{\mu_S^+}\,, \qquad \frac{b_0/b_T}{Q} \sim \frac{\mu_B^+}{\mu_H^+} \sim \frac{\mu_S^+}{\mu_H^+}\,, \qquad \frac{\mathcal{T}}{Q} \sim \frac{\mu_S^+}{\mu_H^+}\,. \tag{2.47}$$

The logarithms of the first ratio appear in the double-differential SCET_{I} beam function in the limit $q_T \ll \sqrt{Q\mathcal{T}}$, and are resummed in SCET_+ by the additional ν evolution in the refactorization in eq. (2.41). Similarly, logarithms of the second ratio appear in the double-differential SCET_{II} soft function in the limit $\mathcal{T} \ll q_T$, and are resummed in SCET_+ by the additional μ evolution in eq. (2.42). Our framework to match between the rich logarithmic structure predicted by eq. (2.39) and the two boundary regimes is the subject of section 3.

2.5 Outer space

We now briefly discuss the outer phase-space regions left blank in figure 2. The region above the SCET_{II} regime is characterized by the hierarchy $q_T \ll \mathcal{T} \ll \sqrt{Q\mathcal{T}}$, while the region to the right of the SCET_{I} regime corresponds to $\mathcal{T} \ll \sqrt{Q\mathcal{T}} \ll q_T$. Both regions are power suppressed.

As we have discussed in section 2.3, only the soft function contributes to $\mathcal{T}$ in SCET_{II}, as the collinear contribution is power suppressed. However, for $q_T \ll \mathcal{T}$, even the soft contribution to $\mathcal{T}$ becomes power suppressed. In particular, for a single real emission at fixed $\mathcal{O}(\alpha_s)$, the region $\mathcal{T} > q_T$ is kinematically forbidden both in SCET_{II} as well as in full QCD. At higher orders only (soft) emissions that are mostly back-to-back such that their transverse momenta largely cancel can fill out this region. The cross section in this region is power suppressed by $\mathcal{O}(q_T^2/\mathcal{T}^2)$. Equivalently, expanding the SCET_{II} factorization of the double-differential cross section in the limit $q_T \ll \mathcal{T}$ reduces it to the single-differential q_T spectrum with an overall $\delta(\mathcal{T})$, which we exploit in our numerical implementation,

JHEP03(2019)124

cf. eq. (B.33). Physically this means that by integrating the double spectrum in SCET_{II} up to some $\mathcal{T}_{\text{cut}} \gg q_T$, we recover the single-differential q_T spectrum, while the effect of the cut is power suppressed in this limit. Note that there is also a contribution from double-parton scattering [86–89] in this region, where the two jets produced in the second interaction alongside the Z boson are naturally back to back and not power suppressed. This contribution is still not expected to much exceed the single-parton scattering contribution because double-parton scattering itself is power suppressed by $\mathcal{O}(\Lambda^2_{\text{QCD}}/\mathcal{T}^2)$, with $\mathcal{T}$ setting the scale of the second hard scatter producing the back-to-back jets.

Similarly, in the limit $\sqrt{Q\mathcal{T}} \ll q_T$, even the contribution from collinear radiation to q_T becomes power suppressed in SCET_{I} [cf. eq. (B.24)], and at leading power we recover the single-differential $\mathcal{T}$ spectrum with an overall $\delta(q_T)$. This is analogous to the relation between the regimes 1 and 2 for a jet veto with a jet rapidity cut in ref. [34], where the effect of a very forward jet rapidity cut (the auxiliary measurement) on collinear radiation becomes power suppressed. An additional subtlety for $\sqrt{Q\mathcal{T}} \ll q_T$ is that very energetic forward radiation with energy $\sim q_T^2/\mathcal{T}$ can theoretically contribute [51], pushing the hard scale up to $q_T^2/\mathcal{T} \gg Q$. However, the cross section in this kinematic configuration is very strongly suppressed by the PDFs, so we choose to describe it at fixed order in this paper.

The above analysis justifies focusing on the shaded regions of phase space in figure 2, corresponding to the main SCET_{I}, SCET_{II}, and SCET_{+} regimes.

3 Matching effective theories

3.1 Structure of power corrections

An important feature of our EFT setup is that the factorized cross section in SCET_{+} differs from the ones in SCET_{I} and SCET_{II} only by a subset of the power corrections it receives relative to the full QCD result,

$$\begin{aligned}\frac{\mathrm{d}\sigma_{\text{I}}}{\mathrm{d}Q\,\mathrm{d}Y\,\mathrm{d}q_T\,\mathrm{d}\mathcal{T}} &= \frac{\mathrm{d}\sigma_{+}}{\mathrm{d}Q\,\mathrm{d}Y\,\mathrm{d}q_T\,\mathrm{d}\mathcal{T}}\left[1+\mathcal{O}\left(\frac{q_T^2}{\mathcal{T}Q}\right)\right],\\ \frac{\mathrm{d}\sigma_{\text{II}}}{\mathrm{d}Q\,\mathrm{d}Y\,\mathrm{d}q_T\,\mathrm{d}\mathcal{T}} &= \frac{\mathrm{d}\sigma_{+}}{\mathrm{d}Q\,\mathrm{d}Y\,\mathrm{d}q_T\,\mathrm{d}\mathcal{T}}\left[1+\mathcal{O}\left(\frac{\mathcal{T}^2}{q_T^2}\right)\right].\end{aligned} \tag{3.1}$$

This is illustrated in figure 6, and follows from comparing eq. (2.40) to eq. (2.7) and eq. (2.21), respectively. Crucially, eq. (3.1) also holds when the cross sections are evaluated at common (but not necessarily fixed-order) scales.

For example, both σ_{I} and σ_{+} share a logarithmic singularity with respect to $\mathcal{T}/Q$, which can be resummed by running between the scales of the hard, soft, and (refactorized) beam functions. In SCET_{+} this amounts to setting the μ^{+} scales to be equal to their μ^{I} counterparts,

$$\mu_B^{+} = \mu_{\mathcal{S}}^{+} = \mu_B^{\text{I}}\,, \qquad \nu_B^{+} = \nu_{\mathcal{S}}^{+} = \mu_{\text{FO}}\,, \qquad \mu_S^{+} = \mu_S^{\text{I}}\,, \tag{3.2}$$

such that any large logarithms inside the refactorized beam function in eq. (2.41) are treated at fixed order. We write $\mathrm{d}\sigma_{+}\big|_{\mu^{\text{I}}}$ to indicate that $\mathrm{d}\sigma_{+}$ is evaluated at scales that satisfy eq. (3.2). A natural way to judge the size of the power corrections in eq. (3.1) then is to

JHEP03(2019)124

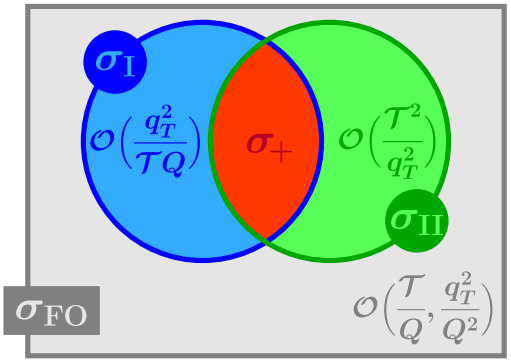

Figure 6. Venn diagram of power corrections to the factorized double-differential spectrum. $\text{SCET}_{\rm I}$ (blue) and $\text{SCET}_{\rm II}$ (green) each capture a set of power corrections that is expanded away in the SCET_+ factorization (red) and the opposite boundary regime. A third class of power corrections to the overall soft-collinear limit is captured by the fixed-order calculation in full QCD (gray).

compare $\mathrm{d}\sigma_+\big|_{\mu^{\rm I}}$ to $\mathrm{d}\sigma_{\rm I}\big|_{\mu^{\rm I}}$, with our choices for $\mu^{\rm I}$ as given in section 2.2, i.e., including the whole set of all-order terms from the $\mathcal{T}$ resummation in both of them. This comparison is shown in figure 7 for representative choices of fixed $\mathcal{T}$ and q_T at NNLL. We can clearly read off a power-like behavior of the difference $\big[\mathrm{d}\sigma_{\rm I} - \mathrm{d}\sigma_+\big]_{\mu^{\rm I}}$ (dotted green) as either $q_T \to 0$ for fixed $\mathcal{T}$ (left panel) or $\mathcal{T} \to \infty$ for fixed q_T (right panel). This also provides a nontrivial check on our implementation of $\sigma_{\rm I}$ and σ_+. This comparison in figure 7 is analogous to the usual procedure of comparing the full-theory result for a cross section with its singular EFT limit at a common scale $\mu_{\rm FO}$. Here, $\text{SCET}_{\rm I}$ takes on the role of the full theory, while SCET_+ provides the singular limit, and the comparison is performed at common scales $\mu^{\rm I}$.

Similarly, both $\sigma_{\rm II}$ and σ_+ have a common singular structure as $q_T/Q \to 0$. In this case, resumming the shared logarithmic terms requires running between the hard, beam, and (refactorized) soft function. In SCET_+ this amounts to setting the μ^+ scales to be equal to their $\mu^{\rm II}$ counterparts,

$$\mu_{\mathcal{S}}^+ = \mu_S^+ = \mu_S^{\rm II}\,, \qquad \nu_{\mathcal{S}}^+ = \nu_S^{\rm II}\,, \tag{3.3}$$

which treats the large logarithms in the refactorized double-differential soft function in eq. (2.42) at fixed order. We denote this choice of scales by $\mathrm{d}\sigma_+\big|_{\mu^{\rm II}}$, with scale setting in b_T space and the inverse Fourier transform understood as in section 2.3. In figure 8 we compare $\mathrm{d}\sigma_+\big|_{\mu^{\rm II}}$ to $\mathrm{d}\sigma^{\rm II}\big|_{\mu^{\rm II}}$ at NNLL as a function of $\mathcal{T}$ at fixed q_T (left) and vice versa (right). It is clear that even when evaluated at its intrinsic scales, $\mathrm{d}\sigma_{\rm II}\big|_{\mu^{\rm II}}$ (solid orange) exhibits an unresummed singularity as $\mathcal{T}/q_T \ll 1$, which, as expected, is captured by $\mathrm{d}\sigma_+\big|_{\mu^{\rm II}}$ (dashed blue) up to power corrections (dotted green). This check is highly nontrivial as it involves an additional Fourier transform on both sides of the comparison. We note that the strong kinematic suppression of the double spectrum for $\mathcal{T} \gtrsim q_T$ is correctly captured by $\text{SCET}_{\rm II}$, where central soft modes resolve the phase-space boundary. In SCET_+, soft modes have too little energy and collinear-soft modes are too forward to resolve it, leading to large power corrections in this region.

JHEP03(2019)124

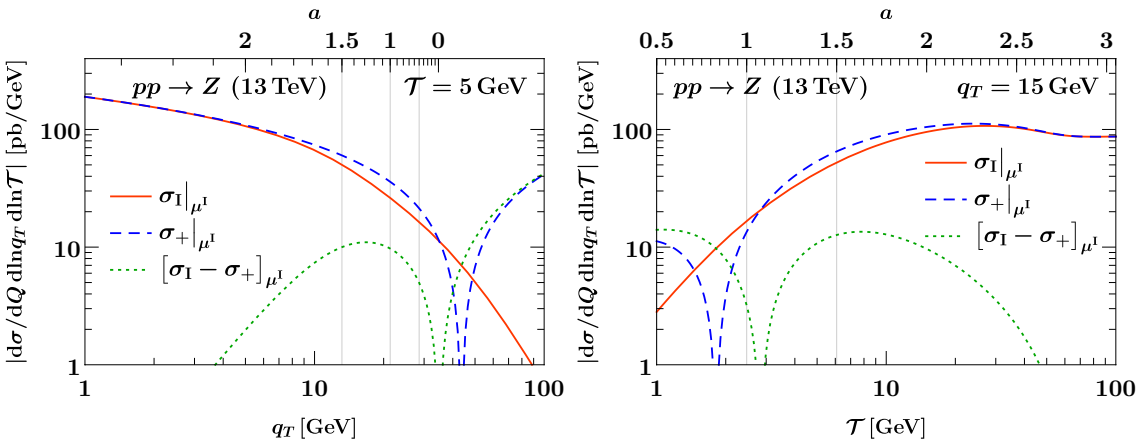

Figure 7. Singular/nonsingular comparison between $\mathrm{SCET_I}$ and $\mathrm{SCET_+}$ at NNLL as a function of q_T for fixed $\mathcal{T} = 5\,\mathrm{GeV}$ (left) and as a function of $\mathcal{T}$ for fixed $q_T = 15\,\mathrm{GeV}$ (right). The orange solid lines show the full $\mathrm{SCET_I}$ result including resummation. The dashed blue lines show the corresponding $\mathrm{SCET_+}$ singular limit with *only* $\mathrm{SCET_I}$ resummation. The dotted green lines show their difference, corresponding to the power corrections indicated in eq. (3.1). The thin vertical lines indicate our choice of transition points (a_1, a_2, a_3) with respect to the regime parameter a (upper horizontal axis), as discussed in section 3.3.

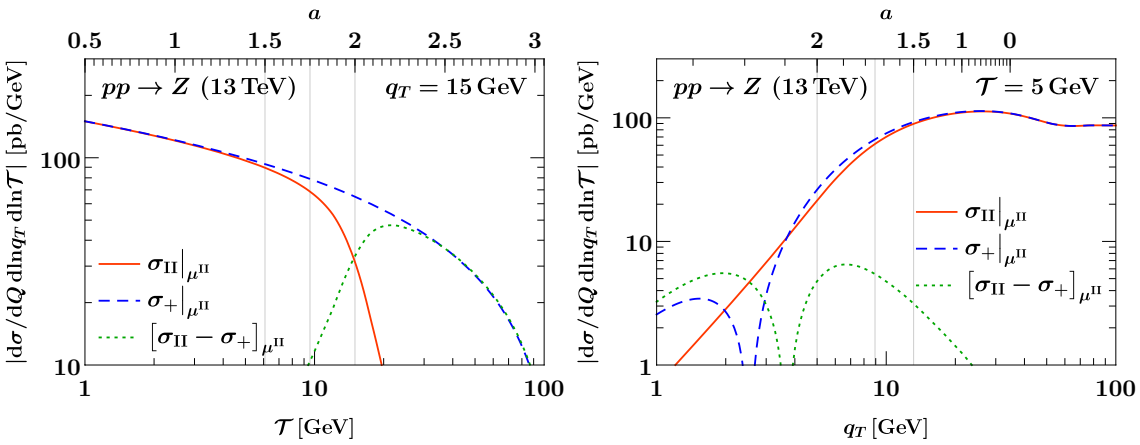

Figure 8. Singular/nonsingular comparison between $\mathrm{SCET_{II}}$ and $\mathrm{SCET_+}$ at NNLL as a function of $\mathcal{T}$ for fixed $q_T = 15\,\mathrm{GeV}$ (left) and as a function of q_T for fixed $\mathcal{T} = 5\,\mathrm{GeV}$ (right). The orange solid lines show the full $\mathrm{SCET_{II}}$ result including resummation. The dashed blue lines show the corresponding $\mathrm{SCET_+}$ singular limit with *only* $\mathrm{SCET_{II}}$ resummation. The dotted green lines show their difference, corresponding to the power corrections indicated in eq. (3.1). The thin vertical lines indicate our choice of transition points (a_4, a_5, a_6) with respect to the regime parameter a (upper horizontal axis), as discussed in section 3.3.

JHEP03(2019)124

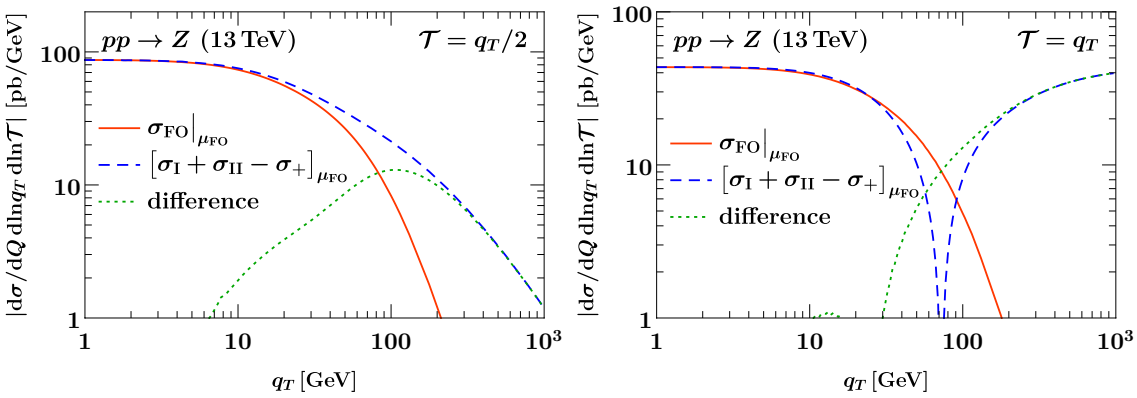

Figure 9. Singular/nonsingular comparison between the matched SCET descriptions and QCD at fixed $\mathcal{O}(\alpha_s)$ as a function of q_T for $\mathcal{T} = q_T/2$ (left) and $\mathcal{T} = q_T$ (right). The orange solid line shows the fixed-order QCD double spectrum, the dashed blue the matched SCET result in eq. (3.4), and the dotted green the difference.

As a final important consequence of figure 6, the complete infrared structure of the double-differential spectrum for $q_T \ll Q$ and $\mathcal{T} \ll Q$, i.e., for any hierarchy between q_T and $\mathcal{T}$, is described by adding the $\mathrm{SCET_I}$ and $\mathrm{SCET_{II}}$ cross sections and removing the overlap between the two by subtracting the $\mathrm{SCET_+}$ cross section,

$$\frac{\mathrm{d}\sigma}{\mathrm{d}Q\,\mathrm{d}Y\,\mathrm{d}q_T\,\mathrm{d}\mathcal{T}} = \left[\frac{\mathrm{d}\sigma_{\rm I}}{\mathrm{d}Q\,\mathrm{d}Y\,\mathrm{d}q_T\,\mathrm{d}\mathcal{T}} + \frac{\mathrm{d}\sigma_{\rm II}}{\mathrm{d}Q\,\mathrm{d}Y\,\mathrm{d}q_T\,\mathrm{d}\mathcal{T}} - \frac{\mathrm{d}\sigma_{+}}{\mathrm{d}Q\,\mathrm{d}Y\,\mathrm{d}q_T\,\mathrm{d}\mathcal{T}}\right] \times \left[1 + \mathcal{O}\left(\frac{q_T^2}{Q^2}, \frac{\mathcal{T}}{Q}\right)\right] . \tag{3.4}$$

In figure 9 we numerically check this relation at fixed $\mathcal{O}(\alpha_s)$, which requires setting all scales equal to a common $\mu_{\rm FO}$. We plot the comparison as a function of q_T along lines of fixed $\mathcal{T}/q_T = 1/2$ (left) and $\mathcal{T}/q_T = 1$ (right), finding excellent agreement between the full result (solid orange) and the first line on the right-hand side of eq. (3.4) (dashed blue), as evident from the power-like behavior of their difference (dotted green) as $q_T, \mathcal{T} \to 0$.

This singular/nonsingular comparison is qualitatively different from the structure of power corrections in either $\mathrm{SCET_I}$ or $\mathrm{SCET_{II}}$ alone, which we already verified in figure 3 and figure 4. Because $\mathrm{SCET_I}$ and $\mathrm{SCET_{II}}$ both involve an additional expansion about a specific hierarchy between q_T and $\mathcal{T}$, they incur power corrections $\mathcal{O}(\mathcal{T}^2/q_T^2)$ or $\mathcal{O}(q_T^2/(Q\mathcal{T}))$, respectively. Accordingly, they only recover the singular limit of full QCD when approaching it along specific lines in the $(q_T, \mathcal{T})$ plane. This is different from figure 9, where the combined expression in eq. (3.4) (dashed blue) describes the singular limit $q_T, \mathcal{T} \to 0$ along an arbitrary line of approach, with the ratio $q_T/\mathcal{T}$ effectively controlling the "admixture" of power corrections $\mathcal{O}(q_T^2/Q^2)$ and $\mathcal{O}(\mathcal{T}/Q)$, respectively. We have verified that also for other fixed ratios of q_T and $\mathcal{T}$, the singular behavior of full QCD is correctly described.

As a final remark, as noted in ref. [90], this property actually qualifies the expression $\mathrm{d}\sigma_{\rm I} + \mathrm{d}\sigma_{\rm II} - \mathrm{d}\sigma_+$ for use as a double-differential subtraction term to treat infrared divergences in fixed-order calculations.

JHEP03(2019)124

3.2 Matching formula

The structure of power corrections discussed in the previous section, together with the all-order resummation shared between SCET_+ and SCET_I or SCET_II, suggests the following matching formula to describe all regions of the double-differential spectrum:

$$\begin{aligned} \mathrm{d}\sigma^{\text{match}} = \mathrm{d}\sigma_+\big|_{\mu^+} &+ \big[\mathrm{d}\sigma_\text{I} - \mathrm{d}\sigma_+\big]_{\mu^\text{I}} + \big[\mathrm{d}\sigma_\text{II} - \mathrm{d}\sigma_+\big]_{\mu^\text{II}} \\ &+ \big[\mathrm{d}\sigma_\text{FO} - \mathrm{d}\sigma_\text{I} - \mathrm{d}\sigma_\text{II} + \mathrm{d}\sigma_+\big]_{\mu_\text{FO}} . \end{aligned} \tag{3.5}$$

The only ingredient in this matching formula we have not yet discussed is $\mathrm{d}\sigma_+\big|_{\mu^+}$, for which all ingredients in the SCET_+ factorization are evaluated at the SCET_+ scales μ^+, such that the full RGE of SCET_+ is in effect. In the following we describe the requirements on μ^+ to ensure the best possible prediction across phase space. Our precise construction of μ^+ to satisfy all requirements is the subject of section 3.3.

In the simplest case, i.e., when the power corrections in eq. (2.40) are small, and thus the SCET_+ parametric assumptions are satisfied, μ^+ is given by the canonical SCET_+ scales in eq. (2.46). As for μ^II, these scales are set in b_T space, followed by an inverse Fourier transform.

As we approach the SCET_I region, the resummation inside the refactorization of the beam function in eq. (2.41) must be turned off,

$$\left.\begin{aligned} \mu_B^+(q_T, \mathcal{T}, b_T) &\to \mu_B^\text{I}(\mathcal{T}) \\ \mu_\mathcal{S}^+(q_T, \mathcal{T}, b_T) &\to \mu_B^\text{I}(\mathcal{T}) \\ \nu_\mathcal{S}^+(q_T, \mathcal{T}, b_T) &\to \nu_B^+(q_T, \mathcal{T}, b_T) \end{aligned}\right\} \quad \text{for} \quad q_T \to \sqrt{Q\mathcal{T}} . \tag{3.6}$$

In addition we can identify the soft scales in SCET_I and SCET_+ because the soft functions are identical,

$$\mu_S^+(q_T, \mathcal{T}, b_T) \to \mu_S^\text{I}(\mathcal{T}) \quad \text{for} \quad q_T \to \sqrt{Q\mathcal{T}} . \tag{3.7}$$

These relations must hold for every value of the b_T argument of the scale.

Similarly, as we approach the SCET_II region, the scales inside the refactorized soft function eq. (2.42) must become equal

$$\left.\begin{aligned} \mu_S^+(q_T, \mathcal{T}, b_T) &\to \mu_S^\text{II}(q_T, b_T) \\ \mu_\mathcal{S}^+(q_T, \mathcal{T}, b_T) &\to \mu_S^\text{II}(q_T, b_T) \\ \nu_\mathcal{S}^+(q_T, \mathcal{T}, b_T) &\to \nu_S^\text{II}(q_T, b_T) \end{aligned}\right\} \quad \text{for} \quad q_T \to \mathcal{T} , \tag{3.8}$$

and we can identify the scales of the common beam function in SCET_II and SCET_+,

$$\left.\begin{aligned} \mu_B^+(q_T, \mathcal{T}, b_T) &\to \mu_B^\text{II}(q_T, b_T) \\ \nu_B^+(q_T, \mathcal{T}, b_T) &\to \nu_B^\text{II}(q_T, b_T) \end{aligned}\right\} \quad \text{for} \quad q_T \to \mathcal{T} . \tag{3.9}$$

Some of the above requirements for the behavior at the boundary are already satisfied by the canonical SCET_+ scales, e.g., the canonical soft scales in SCET_+ and SCET_I are

JHEP03(2019)124

simply equal. The challenge in these cases is to extend the scale choice onto the opposite boundary, where they are constrained in a nontrivial way. The nontrivial all-order information in SCET$_+$ is mostly encoded in the canonical choice of

$$\nu_{\mathcal{S}}^{+}(q_T, \mathcal{T}, b_T) = \frac{(b_0/b_T)^2}{\mathcal{T}} \quad \text{for} \quad \mathcal{T} \ll q_T \ll \sqrt{Q\mathcal{T}}\,, \tag{3.10}$$

which does not coincide with any scale on either boundary.

It is instructive to explicitly consider the behavior of eq. (3.5) on the SCET$_{\rm I}$ and SCET$_{\rm II}$ phase-space boundaries, as well as in the fixed-order region. By construction, for any choice of μ^+ scales satisfying eqs. (3.6) and (3.7) we have

$$\mathrm{d}\sigma_+\big|_{\mu^+} \to \mathrm{d}\sigma_+\big|_{\mu^{\rm I}} \quad \text{for} \quad q_T \to \sqrt{Q\mathcal{T}}\,. \tag{3.11}$$

It follows that

$$\begin{aligned}\mathrm{d}\sigma^{\rm match} \to{}& \mathrm{d}\sigma_{\rm I}\big|_{\mu^{\rm I}} + \big[\mathrm{d}\sigma_{\rm FO} - \mathrm{d}\sigma_{\rm I}\big]_{\mu_{\rm FO}} \\ &+ \big[\mathrm{d}\sigma_{\rm II} - \mathrm{d}\sigma_+\big]_{\mu^{\rm II}} - \big[\mathrm{d}\sigma_{\rm II} - \mathrm{d}\sigma_+\big]_{\mu_{\rm FO}} \quad \text{for} \quad q_T \to \sqrt{Q\mathcal{T}}\,.\end{aligned} \tag{3.12}$$

This mostly coincides with the result in eq. (2.11) of matching $\mathrm{d}\sigma_{\rm I}$ to the fixed-order result $\mathrm{d}\sigma_{\rm FO}$, and is guaranteed to capture all large logarithms of $\mathcal{T}/Q$ captured by the SCET$_{\rm I}$ RGE. It improves over eq. (2.11) by also resumming logarithms of q_T/Q in the power corrections $\mathcal{O}(\mathcal{T}^2/q_T^2)$, encoded in $\big[\sigma_{\rm II} - \sigma_+\big]_{\mu^{\rm II}}$. This is not a numerically large effect and cannot be exploited to achieve the resummation of $\mathcal{T}$ at next-to-leading power, as it is only a subset of all power corrections.

Similarly, eqs. (3.8) and (3.9) imply that

$$\mathrm{d}\sigma_+\big|_{\mu^+} \to \mathrm{d}\sigma_+\big|_{\mu^{\rm II}} \quad \text{for} \quad q_T \to \mathcal{T}\,, \tag{3.13}$$

and consequently

$$\begin{aligned}\mathrm{d}\sigma^{\rm match} \to{}& \mathrm{d}\sigma_{\rm II}\big|_{\mu^{\rm II}} + \big[\mathrm{d}\sigma_{\rm FO} - \mathrm{d}\sigma_{\rm II}\big]_{\mu_{\rm FO}} \\ &+ \big[\mathrm{d}\sigma_{\rm I} - \mathrm{d}\sigma_+\big]_{\mu^{\rm I}} - \big[\mathrm{d}\sigma_{\rm I} - \mathrm{d}\sigma_+\big]_{\mu_{\rm FO}} \quad \text{for} \quad q_T \to \mathcal{T}\,.\end{aligned} \tag{3.14}$$

This mostly coincides with the result in eq. (2.29) of matching $\mathrm{d}\sigma_{\rm II}$ to the fixed-order result $\mathrm{d}\sigma_{\rm FO}$, and thus captures all large logarithms of q_T/Q captured by the SCET$_{\rm II}$ RGE. In addition, it resums logarithms of $\mathcal{T}/Q$ in the $\mathcal{O}(q_T^2/(\mathcal{T}Q))$ power corrections encoded in $[\mathrm{d}\sigma_{\rm I} - \mathrm{d}\sigma_+]_{\mu^{\rm I}}$.

Finally, in the fixed-order region, all μ^+, $\mu^{\rm I}$, and $\mu^{\rm II}$ scales become equal to $\mu_{\rm FO}$. Thus as desired, the matched prediction reduces to the fixed-order result,

$$\mathrm{d}\sigma^{\rm match} \to \mathrm{d}\sigma_{\rm FO}\big|_{\mu_{\rm FO}} \quad \text{for} \quad q_T, \mathcal{T} \to Q\,. \tag{3.15}$$

3.3 Profile scales

In this section, we describe our choice of the central μ^+ scales for the various ingredients in the SCET$_+$ factorized cross section, taking into account the transition to the SCET$_{\rm I}$ and

JHEP03(2019)124

Scale	SCET_I	SCET_+	SCET_II
μ_H	Q	Q	Q
μ_B	$\sqrt{\mathcal{T}Q}$	b_0/b_T	b_0/b_T
ν_B		Q	Q
$\mu_\mathcal{S}$		b_0/b_T	
$\nu_\mathcal{S}$		$(b_0/b_T)^2/\mathcal{T}$	
μ_S	$\mathcal{T}$	$\mathcal{T}$	b_0/b_T
ν_S			b_0/b_T

Table 1. Summary of canonical scales in SCET_I, SCET_+, and SCET_II [see eq. (2.10), (2.25) and (2.46)]. For SCET_+ and SCET_II we give the canonical scales in b_T space.

SCET_II boundary theories as well as the transition to the fixed-order region. The SCET_+ scales are obtained using a regime parameter that selects the appropriate combination of scales from the boundary theories in each region of phase space, and selects a third, independent choice in the SCET_+ "bulk" when necessary. The profile functions that handle the transition to fixed order can conveniently be reused from SCET_I and SCET_II.

We start by summarizing the canonical scales for SCET_I, SCET_II, SCET_+ in table 1. At these scales, the arguments of logarithms in the ingredients of the factorized cross section are order one, i.e., all large logarithms are resummed by RG evolution. To interpolate between the canonical scales in different regimes, we find it convenient to introduce the regime parameter

$$a = 3 - \frac{|\ln(\mathcal{T}/Q)|}{|\ln(q_T/Q)|}\,. \tag{3.16}$$

Its definition is carefully chosen such that $a = 1$ when the SCET_I parametric relation is exactly satisfied, $q_T = \sqrt{\mathcal{T}Q}$, and $a = 2$ on the SCET_II boundary of phase space, $q_T = \mathcal{T}$. As illustrated in the left panel of figure 10, the canonical SCET_+ region lies at intermediate $a \sim 1.5$. The requirements on the SCET_+ scales were given in eqs. (3.6) and (3.7) for the transition to SCET_I, and in eqs. (3.8) and (3.9) for SCET_II. To satisfy these requirements, we take weighted products of scales on the boundary and in the bulk, schematically,

$$\mu^+ = \left[\mu^\text{I}\right]^{h_\text{I}(a)} \left[\mu^+_\text{bulk}\right]^{h_+(a)} \left[\mu^\text{II}\right]^{h_\text{II}(a)}\,. \tag{3.17}$$

The weights in the exponent are given by helper functions that depend on a, as illustrated in the right panel of figure 10. They satisfy

$$h_\text{I}(a) + h_+(a) + h_\text{II}(a) = 1\,, \tag{3.18}$$

for any a and are given explicitly in eq. (3.22) below. The helper functions ensure that the appropriate scales are used in each region, e.g., $h_\text{II}(a)$ is one in the vicinity of $a = 2$ and vanishes for $a < 1.5$, with a smooth transition between regions.

JHEP03(2019)124

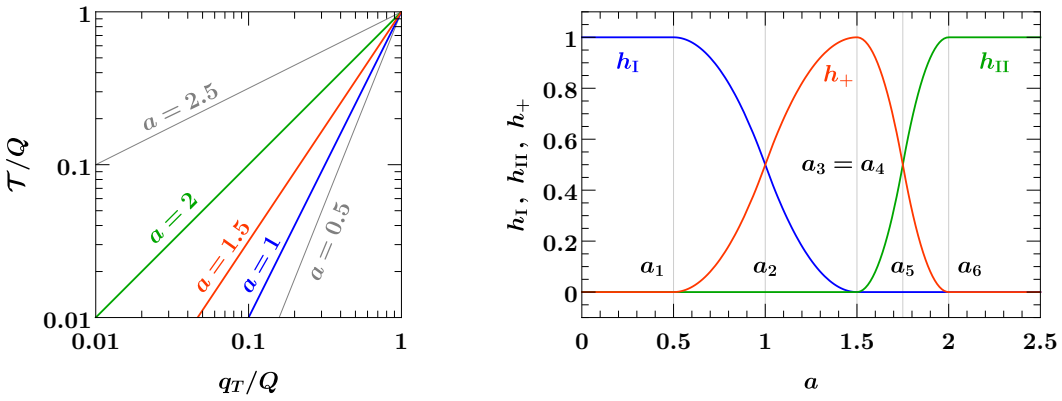

Figure 10. Left: illustration of the regime parameter a that governs the matching between EFTs. We show lines of constant a in the $(q_T, \mathcal{T})$ plane. For $a = 1$ the $\mathrm{SCET_I}$ parametric relation is exactly satisfied, $q_T = \sqrt{Q\mathcal{T}}$, whereas for $a = 2$, the $\mathrm{SCET_{II}}$ parametric relation is exactly satisfied, $q_T = \mathcal{T}$. Right: helper functions used to interpolate between scales on the boundaries ($\mathrm{SCET_I}$, $\mathrm{SCET_{II}}$) and in the bulk ($\mathrm{SCET_+}$). The helper functions have continuous derivatives and always sum to one. The individual helper functions are exactly one in their respective canonical regions. See the text for a detailed discussion.

For the soft and collinear-soft scales, eq. (3.17) takes the following concrete form:

$$\begin{aligned}
\mu_{\mathcal{S}}^{+} &= \left[\mu_B^{\rm I}\right]^{h_{\rm I}(a)} \left[\mu_{\mathcal{S},\rm bulk}^{+}\right]^{h_+(a)} \left[\mu_S^{\rm II}\right]^{h_{\rm II}(a)} , \\
\nu_{\mathcal{S}}^{+} &= \left[\nu\right]^{h_{\rm I}(a)} \left[\nu_{\mathcal{S},\rm bulk}^{+}\right]^{h_+(a)} \left[\nu_S^{\rm II}\right]^{h_{\rm II}(a)} , \\
\mu_S^{+} &= \left[\mu_S^{\rm I}\right]^{h_{\rm I}(a)} \left[\mu_{S,\rm bulk}^{+}\right]^{h_+(a)} \left[\mu_S^{\rm II}\right]^{h_{\rm II}(a)} .
\end{aligned} \tag{3.19}$$

The most nontrivial of these cases is $\nu_{\mathcal{S}}$, which must be equal to the overall ν in the $\mathrm{SCET_I}$ region to turn off the rapidity resummation there, has a distinct canonical value in the $\mathrm{SCET_+}$ bulk, and must asymptote to yet another value on the $\mathrm{SCET_{II}}$ boundary. We note that μ_S^+ also requires a distinct treatment in the bulk to ensure that the hierarchy $\mu_S^+ < \mu_{\mathcal{S}}^+$ inside the refactorized soft function, as implied by the $\mathrm{SCET_+}$ power counting, is not upset by variations (see next subsection). Our central choices for the above scales in the bulk are

$$\begin{aligned}
\mu_{\mathcal{S},\rm bulk}^{+} &= \mu_{\rm FO}\, f_{\rm run}^{\rm II}\left(\frac{q_T}{Q}, \frac{b_0}{b^*(b_T)\,Q}\right) , \quad \nu_{\mathcal{S},\rm bulk}^{+} = \mu_{\rm FO} \frac{\left[f_{\rm run}^{\rm II}\left(\frac{q_T}{Q}, \frac{b_0}{b^*(b_T)Q}\right)\right]^2}{f_{\rm run}^{\rm I}\left(\frac{\mathcal{T}}{Q}\right)} , \\
\mu_{S,\rm bulk}^{+} &= \mu_{\rm FO}\, f_{\rm run}^{\rm I}\left(\frac{\mathcal{T}}{Q}\right) .
\end{aligned} \tag{3.20}$$

The profile function $f_{\rm run}^{\rm I}$ was introduced for the transition between $\mathrm{SCET_I}$ and fixed-order QCD in eq. (2.14), and similarly for the hybrid profile $f_{\rm run}^{\rm II}$ in eq. (2.32) and the nonperturbative $b^*(b_T)$ prescription in eq. (2.34). These functions turn off the resummation of logarithms involving q_T (b_T) and $\mathcal{T}$, respectively, as the fixed-order regime is approached, and also ensure that scales are frozen in the nonperturbative regime to avoid the Landau pole. It is straightforward to check that away from the nonperturbative region, the above

JHEP03(2019)124

bulk scales all assume their canonical values for $q_T, \mathcal{T} \ll Q$ as given in table 1, and asymptote to $\mu_{\rm FO}$ when simultaneously taking $q_T, \mathcal{T} \to Q$. The beam function scales in the bulk can simply be associated with their $\text{SCET}_{\rm II}$ counterparts and only require a transition towards the $\text{SCET}_{\rm I}$ boundary,

$$\begin{aligned}\mu_B^+ &= \left[\mu_B^{\rm I}\right]^{h_{\rm I}(a)} \left[\mu_B^{\rm II}\right]^{h_+(a)+h_{\rm II}(a)}, \\ \nu_B^+ &= \left[\nu\right]^{h_{\rm I}(a)} \left[\nu_B^{\rm II}\right]^{h_+(a)+h_{\rm II}(a)}.\end{aligned} \tag{3.21}$$

In our numerical implementation, we choose the helper functions $h_{\rm I,II,+}$ as

$$h_{\rm I}(a) \equiv \begin{cases} 1 & a < a_1\,, \\ 1 - c_{123}(a) & a_1 \le a < a_2\,, \\ c_{312}(a) & a_2 \le a < a_3\,, \\ 0 & a_3 \le a\,, \end{cases} \qquad h_{\rm II}(a) \equiv \begin{cases} 0 & a < a_4\,, \\ c_{456}(a) & a_4 \le a < a_5\,, \\ 1 - c_{645}(a) & a_5 \le a < a_6\,, \\ 1 & a_6 \le a\,, \end{cases}$$

$$h_+(a) \equiv 1 - h_{\rm I}(a) - h_{\rm II}(a)\,, \tag{3.22}$$

where the polynomials governing the interpolation between zero and one are

$$c_{ijk}(a) = \frac{(a - a_i)^2}{(a_i - a_j)(a_i - a_k)}\,. \tag{3.23}$$

The transition points $a_{1,\ldots,6}$ determine the transition between the different regions, as can be seen from the helper functions in figure 10: for values $a_3 \le a < a_4$, the exact canonical SCET_+ scales are selected, implying that the resummation of logarithms of both q_T and $\mathcal{T}$ is fully turned on. For lower values $a_1 \le a < a_3$, the additional q_T resummation is smoothly turned off and for $a < a_1$, $\text{SCET}_{\rm I}$ scales are used so that only logarithms of $\mathcal{T}$ are resummed. Conversely, for higher values of the regime parameter $a_4 \le a < a_6$, the resummation of $\mathcal{T}$ logarithms is smoothly turned off. At values $a_6 \le a$, $\text{SCET}_{\rm II}$ scales are selected by the helper functions, and the additional resummation of logarithms of $\mathcal{T}$ is completely turned off.

In practice we use $(a_1, a_2, a_3, a_4, a_5, a_6) = (0.5, 1.0, 1.5, 1.5, 1.75, 2.0)$. This choice ensures that for $a \ge a_6 = 2$, we fully recover $\text{SCET}_{\rm II}$ resummation and faithfully describe the kinematic edge at $q_T \sim \mathcal{T}$ by preserving the $\mathcal{O}(1)$ cancellation between $\sigma_+\big|_{\mu^{\rm II}}$ and the $\text{SCET}_{\rm II}$ nonsingular contribution visible at $a \sim 2$ in the left panel of figure 8. (In both figures 7 and 8, corresponding values of a are indicated on the horizontal axis at the top of the panels.) On the other hand, from figure 7 we observe that power corrections from $\text{SCET}_{\rm I}$ are smaller and tend to set in at values of a lower than the naively expected $a = 1$. E.g., an $\mathcal{O}(1)$ cancellation between $\sigma_+\big|_{\mu^{\rm I}}$ and the $\text{SCET}_{\rm I}$ nonsingular only is in effect around $a \sim 0.5$ in the right panel of figure 7, leaving more room for slowly turning off the SCET_+ resummation down towards $a_1 = 0.5$. This is expected because the $\text{SCET}_{\rm I}$ nonsingular encodes the suppression of collinear recoil beyond the naive phase-space boundary at $a \sim 1$ ($q_T \sim \sqrt{Q\mathcal{T}}$) that is washed out by the PDFs, unlike the sharp kinematic edge at $q_T \sim \mathcal{T}$ encoded in the $\text{SCET}_{\rm II}$ nonsingular. For simplicity we set $a_3 = a_4$ for our central prediction,

JHEP03(2019)124

i.e., we shrink the canonical SCET$_+$ region to a point at $a = 1.5$, and fix a_2 (a_5) to be the midpoint between a_1 and a_3 (a_4 and a_6). Variations of the transition points, including independent variations of a_3 and a_4, are considered as part of our uncertainty estimate described in the next section.

3.4 Perturbative uncertainties

In this section we describe how we assess perturbative uncertainties by varying the scales entering the matched prediction in eq. (3.5). Following the same approach as for SCET$_{\rm I}$ and SCET$_{\rm II}$ on their own (see sections 2.2 and 2.3), we distinguish between resummation uncertainties and a fixed-order uncertainty. The fixed-order uncertainty $\Delta_{\rm FO}$ is estimated by varying $\mu_{\rm FO}$ up and down by a factor of two, i.e., by setting $\mu_{\rm FO} = \{Q/2, 2Q\}$. Since all scales (in any piece of the matching formula) include an overall factor of $\mu_{\rm FO}$, the ratios between the various scales remain unchanged and the same logarithms are resummed. The fixed-order uncertainty $\Delta_{\rm FO}$ is then taken to be the maximum deviation from the central cross section.

We consider several sources of resummation uncertainty entering the matched prediction in eq. (3.5). To probe the tower of logarithms of $\mathcal{T}/Q$ predicted by the SCET$_{\rm I}$ RGE, we perform variations of $\mu_B^{\rm I}$ and $\mu_S^{\rm I}$ parametrized by α and β as in eq. (2.15). This directly affects the resummed power corrections $\left[{\rm d}\sigma_{\rm I} - {\rm d}\sigma_+\right]_{\mu_{\rm I}}$ captured by SCET$_{\rm I}$. In addition, however, ${\rm d}\sigma_+\big|_{\mu_+}$ near the SCET$_{\rm I}$ boundary also undergoes variations because for large $h_{\rm I}$, the SCET$_+$ scales in eqs. (3.19) and (3.21) strongly depend on their SCET$_{\rm I}$ counterparts and inherit their variations. Our setup thus ensures that in (or near) the SCET$_{\rm I}$ region, variations probing resummed logarithms of $\mathcal{T}/Q$ are properly treated as correlated between the SCET$_+$ cross section and the SCET$_{\rm I}$ matching correction. When referring to the matched prediction in eq. (3.5), we take $\Delta_{\rm I}$ to be the maximum deviation of ${\rm d}\sigma_{\rm match}$ from its central value under these correlated variations of α, β.

In complete analogy, we define $\Delta_{\rm II}$ as the maximum deviation under correlated variations of $\mu_{\rm II}$ as described in section 2.3. These variations act on both $\left[{\rm d}\sigma_{\rm II} - {\rm d}\sigma_+\right]_{\mu_{\rm II}}$ and ${\rm d}\sigma_+\big|_{\mu_+}$, where now the SCET$_+$ scales inherit variations from $\mu_{\rm II}$ near the SCET$_{\rm II}$ boundary (where $h_{\rm II}$ is large). As a result, $\Delta_{\rm II}$ probes an all-order set of logarithms of $(b_0/b_T)/Q$ predicted and resummed by the SCET$_{\rm II}$ RGE, and properly captures the correlated tower of logarithms in SCET$_+$. We like to stress that our setup is fully general with respect to the method chosen to perform scale variations for the boundary theories, as any variation will automatically be inherited by SCET$_+$.

As a final source of uncertainty, we consider the uncertainty inherent in our matching procedure and in our choice of SCET$_+$ scales in the bulk. To estimate this we perform the following 8 variations of the (in principle arbitrary) transition points (a_1, a_3, a_4, a_6),

$$\begin{aligned} &(\uparrow,-,-,-)\,, \quad (-,\downarrow,-,-)\,, \quad (-,-,-,\downarrow)\,, \quad (-,\uparrow,\uparrow,-)\,, \\ &(\downarrow,-,-,-)\,, \quad (-,-,\uparrow,-)\,, \quad (-,-,-,\uparrow)\,, \quad (-,\downarrow,\downarrow,-)\,, \end{aligned} \tag{3.24}$$

where $\uparrow$ ($\downarrow$) indicates a variation by $+0.2$ (-0.2), a dash indicates keeping the transition point fixed, and we always maintain $a_2 = (a_1 + a_3)/2$ and $a_5 = (a_4 + a_6)/2$. In addition,

JHEP03(2019)124

we perform the following two variations of the SCET_+ bulk scales,

$$\mu^+_{\mathcal{S},\mathrm{bulk}} = \mu_{\mathrm{FO}} \left(\frac{q_T}{\mathcal{T}}\right)^{+\gamma/2} f^{\mathrm{II}}_{\mathrm{run}}\Big(\frac{q_T}{Q}, \frac{b_0}{b^* Q}\Big)\,,$$
$$\mu^+_{S,\mathrm{bulk}} = \mu_{\mathrm{FO}} \left(\frac{q_T}{\mathcal{T}}\right)^{-\gamma/2} f^{\mathrm{I}}_{\mathrm{run}}\Big(\frac{\mathcal{T}}{Q}\Big)\,, \qquad \gamma = \{+1/6, -1/6\}\,, \tag{3.25}$$

where $\gamma = 0$ corresponds to the central scales in eq. (3.20). Similarly to the role of β in the $\mathrm{SCET}_{\mathrm{I}}$ variations [see eq. (2.15)], making the strength of the γ variations depend on the ratio $q_T/\mathcal{T}$ ensures that the hierarchy $\mu_S < \mu_{\mathcal{S}}$ implied by the SCET_+ power counting is not upset by variations, counting $b_0/b_T \sim q_T$. We note that the third independent bulk scale $\nu^+_{\mathcal{S},\mathrm{bulk}}$ does not require independent variation because it only enters through rapidity logarithms of $\nu_B^+/\nu_{\mathcal{S}}^+$, which are already being probed by variations of ν_B^+ inherited from $\mathrm{SCET}_{\mathrm{II}}$. Taking the envelope of the eight transition point variations and the two bulk scale variations, we obtain a third contribution to the resummation uncertainty denoted by Δ_+. The total uncertainty assigned to the matched prediction is then given by adding all contributions in quadrature,

$$\Delta_{\mathrm{total}} = \Delta_+ \oplus \Delta_{\mathrm{I}} \oplus \Delta_{\mathrm{II}} \oplus \Delta_{\mathrm{FO}}\,. \tag{3.26}$$

3.5 Differential and cumulant scale setting

We will now discuss the issue of differential versus cumulant scale setting, starting with the simpler case of a cross section differential in a single observable and using 0-jettiness $\mathcal{T}$ as an example. There are two equivalent quantities of interest in this case, namely the spectrum $\mathrm{d}\sigma/\mathrm{d}\mathcal{T}$ with respect to $\mathcal{T}$ and the cumulant cross section $\sigma(\mathcal{T}_{\mathrm{cut}})$ with a cut on $\mathcal{T}$. The two quantities are related by

$$\sigma(\mathcal{T}_{\mathrm{cut}}) = \int_0^{\mathcal{T}_{\mathrm{cut}}} \mathrm{d}\mathcal{T}\, \frac{\mathrm{d}\sigma}{\mathrm{d}\mathcal{T}}\,, \tag{3.27}$$

where we suppress the dependence on Q^2 and Y for the purposes of this subsection. Accordingly, in a resummation analysis one can implement the resummation scales either in terms of the differential variable $\mathcal{T}$ to directly predict the spectrum, or in terms of the cumulant variable $\mathcal{T}_{\mathrm{cut}}$ to predict the cross section integrated up to $\mathcal{T}_{\mathrm{cut}}$. The other observable then follows from eq. (3.27).

Explicitly, with differential scale setting (indicated by the subscript), the differential and cumulant cross section are given by

$$\frac{\mathrm{d}\sigma_{\mathrm{diff}}}{\mathrm{d}\mathcal{T}} = \frac{\mathrm{d}\sigma}{\mathrm{d}\mathcal{T}}\Big|_{\mu(\mathcal{T})}\,,$$
$$\sigma_{\mathrm{diff}}(\mathcal{T}_{\mathrm{cut}}) = \int^{\mathcal{T}_{\mathrm{cut}}} \mathrm{d}\mathcal{T} \left[\theta(\mathcal{T} > \mathcal{T}_{\mathrm{np}}) \frac{\mathrm{d}\sigma}{\mathrm{d}\mathcal{T}}\Big|_{\mu(\mathcal{T})} + \theta(\mathcal{T} \le \mathcal{T}_{\mathrm{np}}) \frac{\mathrm{d}\sigma}{\mathrm{d}\mathcal{T}}\Big|_{\mu(\mathcal{T}_{\mathrm{np}})}\right]. \tag{3.28}$$

In the first term under the integral in the cumulant cross section, all scales μ entering the resummed and matched prediction depend on the integration variable $\mathcal{T}$. Because our setup only reliably predicts the spectrum away from the nonperturbative region, we choose

JHEP03(2019)124

to integrate the resummed spectrum with differential scale setting up from some small cutoff $\mathcal{T}_{\text{np}}$, and include an "underflow" contribution given by the second term under the integral. For the underflow contribution for $\mathcal{T} \leq \mathcal{T}_{\text{np}}$, the spectrum is evaluated at fixed scales corresponding to $\mathcal{T}_{\text{np}}$, such that the integral can be done analytically. The underflow contribution is Sudakov suppressed and thus typically small.

Using cumulant scale setting, we instead use

$$\begin{aligned}\sigma_{\text{cumul}}(\mathcal{T}_{\text{cut}}) &= \int^{\mathcal{T}_{\text{cut}}} \mathrm{d}\mathcal{T}\, \frac{\mathrm{d}\sigma}{\mathrm{d}\mathcal{T}}\Big|_{\mu(\mathcal{T}_{\text{cut}})}\,, \\ \frac{\mathrm{d}\sigma_{\text{cumul}}}{\mathrm{d}\mathcal{T}} &= \frac{\mathrm{d}\sigma}{\mathrm{d}\mathcal{T}}\Big|_{\mu(\mathcal{T})} + \sum_i \left[\frac{\mathrm{d}}{\mathrm{d}\mu_i}\int^{\mathcal{T}} \mathrm{d}\mathcal{T}'\, \frac{\mathrm{d}\sigma}{\mathrm{d}\mathcal{T}'}\right]_{\mu(\mathcal{T})} \frac{\mathrm{d}\mu_i(\mathcal{T})}{\mathrm{d}\mathcal{T}}\,. \end{aligned} \tag{3.29}$$

In this case, the scales in the cumulant cross section depend on $\mathcal{T}_{\text{cut}}$, and not the integration variable $\mathcal{T}$, so the integral up to $\mathcal{T}_{\text{cut}}$ can easily be performed analytically. The expression for the differential cross section arises from taking the derivative of the cumulant cross section, where the chain rule leads to the sum of derivatives of each of the scales μ_i in μ with respect to $\mathcal{T}$.

Cumulant scale setting ensures that for $\mathcal{T}_{\text{cut}} \to Q$, the resummed and matched cumulant cross section exactly reproduces the inclusive fixed-order cross section. This follows from the generic requirement on profile scales in the fixed-order region,

$$\mu_i(\mathcal{T}_{\text{cut}}) \to \mu_{\text{FO}} \quad \text{for} \quad \mathcal{T}_{\text{cut}} \to Q\,. \tag{3.30}$$

Thus for cumulant scale setting, the spectrum has the correct (fixed-order) normalization. However, the additional derivatives of the scales in eq. (3.29) tend to produce artifacts in the spectrum if the profile functions $\mu_i(\mathcal{T})$ used to interpolate between the resummation region $\mathcal{T} \ll Q$ to the fixed-order region $\mathcal{T} \sim Q$ undergo a rapid transition. In particular, a smooth matching to the fixed-order prediction at the level of the differential spectrum typically requires differential scale setting. Moreover, the scale variations using cumulant scale setting tend to produce unreliable uncertainties for the spectrum.

If instead differential scale setting is used, the spectrum is free from such artifacts. However, the integral of the spectrum will not exactly recover the inclusive fixed-order cross section, and the uncertainties obtained for the cumulant by integrating the spectrum scale variations tend to accumulate and end up being much larger than they should be for the total cross section. As in the case of the spectrum with cumulant scale setting, this mismatch purely arises from residual scale dependence, and therefore is formally beyond the working order. It can however still be numerically significant.

Therefore, in general one should use the scale setting that is appropriate for the quantity of interest, i.e., one should use cumulant scale setting when making predictions for the cumulant, and differential scale setting when one is interested in the spectrum. This issue of differential versus cumulant scale setting is well appreciated in the literature for the single-differential case, see e.g. refs. [50, 65, 91, 92]. It fundamentally results from the fact that long-range correlations across the spectrum are not accounted for by the profile scales used for the differential predictions. Conversely, profile scales for the cumulant do

JHEP03(2019)124

not correctly capture the slope of the cumulant and its uncertainty. An elaborate procedure for obtaining a spectrum with differential scales that still produce the exact cross section and uncertainties was developed in ref. [92]. In the GENEVA Monte Carlo generator, the mismatch between differential and cumulant scales is accounted for by adding explicit higher-order terms [50].

For a simultaneous measurement of q_T and $\mathcal{T}$, there are in principle four quantities of interest, namely the double-differential spectrum $\mathrm{d}\sigma/\mathrm{d}q_T\,\mathrm{d}\mathcal{T}$, the single-differential spectra $\mathrm{d}\sigma(q_T^{\mathrm{cut}})/\mathrm{d}\mathcal{T}$ and $\mathrm{d}\sigma(\mathcal{T}_{\mathrm{cut}})/\mathrm{d}q_T$ with a cut on the other variable, and the double cumulant $\sigma(q_T^{\mathrm{cut}},\mathcal{T}_{\mathrm{cut}})$. They are all related by integration or differentiation, allowing for four different ways of setting scales in each case. For our explicit numerical results in section 4, we take a pragmatic approach and use the appropriate combination of differential or cumulant scale setting with respect to either q_T or $\mathcal{T}$ for each of these quantities. This is achieved by evaluating the resummed prediction at profile scales given by the setup described in sections 2.2 and 2.3 as well as section 3.3, but with q_T ($\mathcal{T}$) replaced by q_T^{cut} ($\mathcal{T}_{\mathrm{cut}}$) as appropriate. In this way we are guaranteed to avoid artifacts from profile functions in spectrum observables, and on the other hand ensure that cumulant observables have the correct limiting behavior; e.g., $\sigma(q_T^{\mathrm{cut}},\mathcal{T}_{\mathrm{cut}})$ will by construction recover the inclusive fixed-order cross section when lifting both cuts, while $\mathrm{d}\sigma(q_T^{\mathrm{cut}})/\mathrm{d}\mathcal{T}$ and $\mathrm{d}\sigma(\mathcal{T}_{\mathrm{cut}})/\mathrm{d}q_T$ exactly recover the resummed and matched prediction for the respective inclusive spectrum at large values of the cut.

Nevertheless, it is interesting to ask how well the different combinations of differential and cumulant scale setting fare for observables other than the one they are designed to describe. In particular we should ask how well the $(q_T,\mathcal{T})$ scale setting we described in earlier sections performs at the level of cumulant observables and their inclusive limit. To do so, we can always promote a spectrum using differential scale setting in q_T ($\mathcal{T}$) to a prediction for the cumulant up to q_T^{cut} ($\mathcal{T}_{\mathrm{cut}}$) using the analogue of eq. (3.28). The only nontrivial new procedure is computing the double cumulant directly from $(q_T,\mathcal{T})$ scales, where we need to account for an overlap in underflow contributions as

$$\begin{aligned}\sigma_{\mathrm{diff,diff}}(q_T^{\mathrm{cut}},\mathcal{T}_{\mathrm{cut}}) = \int^{q_T^{\mathrm{cut}}}\mathrm{d}q_T \int^{\mathcal{T}_{\mathrm{cut}}}\mathrm{d}\mathcal{T}\,\Bigg[&\theta(q_T>q_T^{\mathrm{np}})\,\theta(\mathcal{T}>\mathcal{T}_{\mathrm{np}})\frac{\mathrm{d}\sigma}{\mathrm{d}q_T\,\mathrm{d}\mathcal{T}}\bigg|_{\mu(q_T,\mathcal{T})}\\ &+\theta(q_T\le q_T^{\mathrm{np}})\,\theta(\mathcal{T}>\mathcal{T}_{\mathrm{np}})\frac{\mathrm{d}\sigma}{\mathrm{d}q_T\,\mathrm{d}\mathcal{T}}\bigg|_{\mu(q_T^{\mathrm{np}},\mathcal{T})}\\ &+\theta(q_T>q_T^{\mathrm{np}})\,\theta(\mathcal{T}\le\mathcal{T}_{\mathrm{np}})\frac{\mathrm{d}\sigma}{\mathrm{d}q_T\,\mathrm{d}\mathcal{T}}\bigg|_{\mu(q_T,\mathcal{T}_{\mathrm{np}})}\\ &-\theta(q_T\le q_T^{\mathrm{np}})\,\theta(\mathcal{T}\le\mathcal{T}_{\mathrm{np}})\frac{\mathrm{d}\sigma}{\mathrm{d}q_T\,\mathrm{d}\mathcal{T}}\bigg|_{\mu(q_T^{\mathrm{np}},\mathcal{T}_{\mathrm{np}})}\Bigg].\end{aligned} \tag{3.31}$$

The distinction between differential or cumulant scale setting is only relevant for q_T versus q_T^{cut} but not for the underlying resummation in b_T space, so we suppress the dependence of the hybrid scales on b_T. In practice we use $q_T^{\mathrm{np}} = \mathcal{T}_{\mathrm{np}} = 1\,\mathrm{GeV}$, and implement the integrals in eqs. (3.28) and (3.31) as sums over logarithmically spaced bins with bin size $\Delta(\log_{10} q_T) = \Delta(\log_{10}\mathcal{T}) = 0.08$, where the spectrum is evaluated at the logarithmic

JHEP03(2019)124

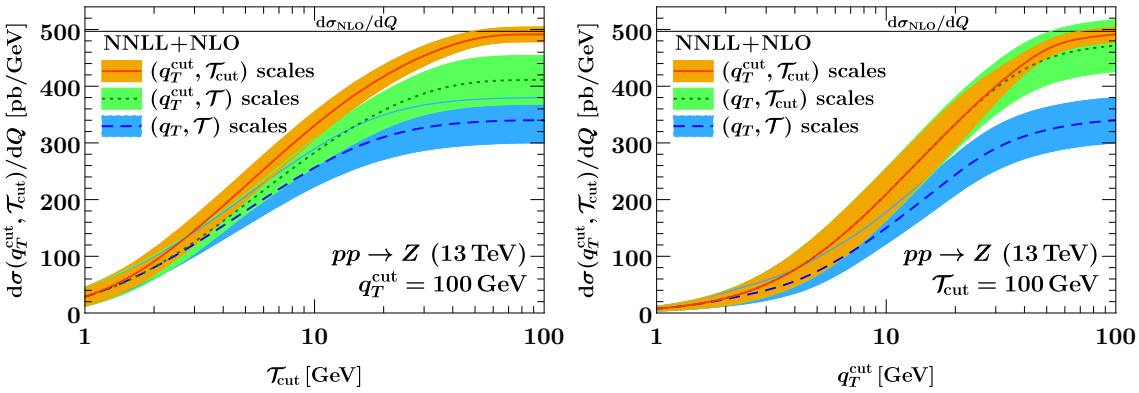

Figure 11. The double cumulant cross section as a function of $\mathcal{T}_{\rm cut}$ for $q_T^{\rm cut} = 100\,\text{GeV}$ (left) and as a function of $q_T^{\rm cut}$ for $\mathcal{T}_{\rm cut} = 100\,\text{GeV}$ (right). The bands indicate the total perturbative uncertainty $\Delta_{\rm total}$, see section 3.4. The colors correspond to different scale setting prescriptions (default: solid orange); see the text for details.

midpoint of the bin. Scale variations in the integrated results are performed by integrating each instance of the spectrum separately and computing maximum deviations from central in the end. The final results are interpolated for clarity.

In figures 11 to 13, we compare our default scale setting for various cumulant observables (solid orange) to more differential scale setting (dashed blue and dotted green), i.e., choosing μ in terms of q_T rather than $q_T^{\rm cut}$ and/or $\mathcal{T}$ rather than $\mathcal{T}_{\rm cut}$. In figure 11, we show the double cumulant cross section, for which our default is to use scales in terms of $q_T^{\rm cut}$ and $\mathcal{T}_{\rm cut}$. The horizontal reference line indicates the inclusive fixed-order cross section. In figure 12 we show the $\mathcal{T}$ spectrum with a cut on q_T, for which our default scales are in terms of $q_T^{\rm cut}$ and $\mathcal{T}$, and the converse for figure 13. In figures 12 and 13 the left panel shows the dependence on the cut at a representative point along the spectrum, with the reference line indicating the resummed prediction for the inclusive (strictly single-differential) spectrum. The right panel shows the spectrum at a representative choice of the cut.

We start by observing that in all cases, the predictions obtained using the default scale setting (solid orange) cleanly asymptote to the respective target observable (the reference line) for large values of the cut. The central double-differential prediction in the left panel of figure 13 slightly overshoots the inclusive result beyond the phase-space boundary $\mathcal{T}_{\rm cut} \gtrsim q_T$ (where our calculation is effectively a leading-order calculation), but is monotonic within uncertainties. Furthermore, the uncertainty obtained using our default is smaller than any of the ones obtained from more differential scale setting. This is expected because differential scale setting cannot account for correlations between different bins of the spectrum, giving rise to a larger band in the cumulant cross sections.

We further note that predictions obtained using q_T or $q_T^{\rm cut}$ scale setting are mutually compatible, i.e., their uncertainty bands (very nearly) overlap, as long as the scale setting with respect to $\mathcal{T}$ is done the same way in both cases. This can be seen from the right panel of figure 11 by contrasting the default $(q_T^{\rm cut}, \mathcal{T}_{\rm cut})$ scales (solid orange) and $(q_T, \mathcal{T}_{\rm cut})$ scales (dotted green). Similarly, in figure 12 we find that the default $(q_T^{\rm cut}, \mathcal{T})$ scales (solid orange)

JHEP03(2019)124

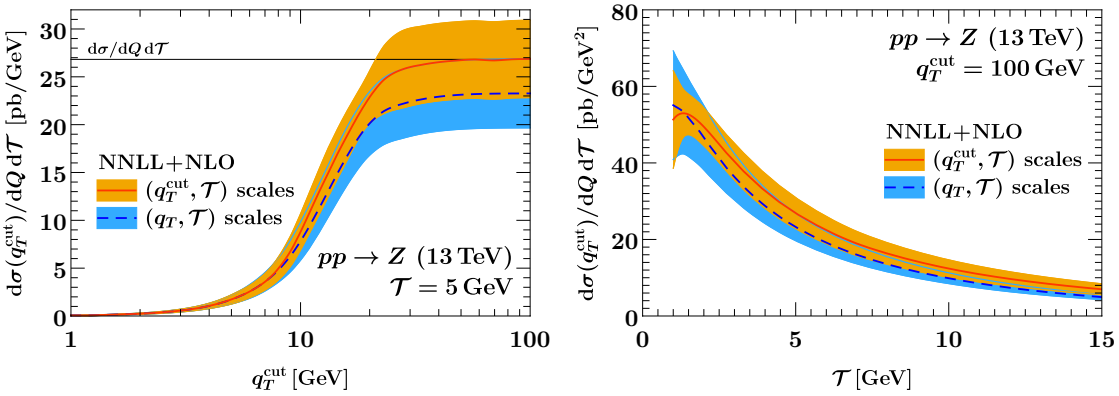

Figure 12. The $\mathcal{T}$ spectrum with a cut on q_T as a function of q_T^{cut} at fixed $\mathcal{T} = 5\,\text{GeV}$ (left) and as a function of $\mathcal{T}$ at fixed $q_T^{\text{cut}} = 100\,\text{GeV}$ (right). The bands indicate the total perturbative uncertainty Δ_{total}, see section 3.4. The colors correspond to different scale setting prescriptions (default: solid orange); see the text for details.

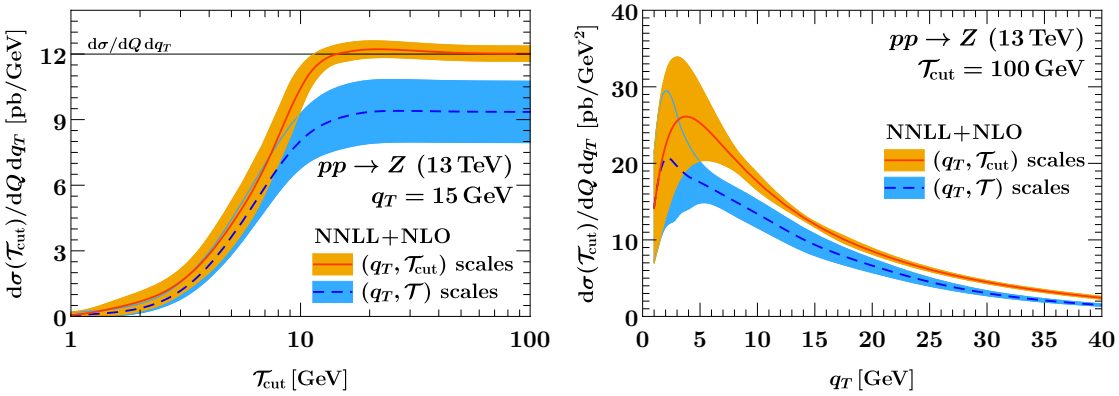

Figure 13. The q_T spectrum with a cut on $\mathcal{T}$ as a function of $\mathcal{T}_{\text{cut}}$ for $q_T = 15\,\text{GeV}$ (left) and as a function of q_T for $\mathcal{T}_{\text{cut}} = 100\,\text{GeV}$ (right). The bands indicate the total perturbative uncertainty Δ_{total}, see section 3.4. The colors correspond to different scale setting prescriptions (default: solid orange); see the text for detail.

and $(q_T, \mathcal{T})$ scale setting (dashed blue) roughly differ by their respective uncertainties. In principle these relations are expected since the unphysical scale dependence is canceled by higher-order corrections, which our scale variations are designed to probe. For the case of q_T versus q_T^{cut} scales in particular, we note that due to our specific choice of hybrid profile scales in eq. (2.32), differences between the two prescriptions only start to appear when turning off the resummation, such that g_{run} is nonzero. E.g. for a high $\mathcal{T}_{\text{cut}} = 100\,\text{GeV}$, which is also a good proxy for the inclusive q_T spectrum, the two prescriptions fully agree in the canonical region $q_T^{\text{cut}} \leq 20\,\text{GeV}$ (see the right panel of figure 11). This is responsible for the good overall agreement because most of the cross section is concentrated in the canonical region.

JHEP03(2019)124

The comparison of $\mathcal{T}$ versus $\mathcal{T}_{\text{cut}}$ scales is much less favorable, with the former failing to reproduce the latter's inclusive limit within uncertainties in all cases. This is in line with the discrepancy reported in ref. [92] for a single-differential measurement of thrust in e^+e^- collisions and at a comparable working order (NLL′+NLO). The mismatch is most striking between the default scales (solid orange) and $(q_T, \mathcal{T})$ scales (dashed blue) in figures 11 and 13, implying that more effort is required to ensure both a correct integral and the best possible prediction for the shape of the double-differential spectrum.

From our previous discussion we conclude that the mismatch mostly reduces to the question of differential versus cumulant scale setting in $\mathcal{T}$ alone, so that the methods developed for the single-differential case in refs. [50, 92] can be brought to bear here as well if desired. However, since this is a well-known issue that is merely inherited from the single-differential case, we do not pursue this further here.

Instead, we consider a modification of our profile scales to illustrate that the issue is indeed a correlated higher-order effect related to scale choices. Specifically, we can consider lowering the canonical low scale $\mu_S^{\text{I}} \sim (\mu_B^{\text{I}})^2/\mu_H^{\text{I}} \sim \mathcal{T}$ in SCET_{I} by a factor of $c = 0.5$, which does not parametrically violate the canonical scaling. Including a smooth interpolation to the fixed-order and nonperturbative region, this can be achieved by replacing eq. (2.14) with

$$f_{\text{run}}^{\text{I}}(c; x) = \begin{cases} x_0\left(1 + \frac{c^2x^2}{4x_0^2}\right) & x \le 2x_0/c\,, \\ cx & 2x_0/c < x \le x_1\,, \\ cx + \frac{(2-cx_2-cx_3)(x-x_1)^2}{2(x_2-x_1)(x_3-x_1)} & x_1 < x \le x_2\,, \\ 1 - \frac{(2-cx_1-cx_2)(x-x_3)^2}{2(x_3-x_1)(x_3-x_2)} & x_2 < x \le x_3\,, \\ 1 & x_3 < x\,, \end{cases} \tag{3.32}$$

and keeping the entire remaining profile setup unchanged; setting $c = 1$ recovers eq. (2.14).

Our results using eq. (3.32) are shown in figure 14, where we repeat the left panels of figures 11 and 13 using the modified setup. Note that for simplicity, we use eq. (3.32) for all results in this figure, i.e., for both differential and cumulant scale setting. We find that the simple modification eq. (3.32) already substantially improves the agreement between differential and cumulant scale setting, with the result from $(q_T^{\text{cut}}, \mathcal{T})$ scales (dotted green, left panel) covering the inclusive fixed-order cross section and the result from $(q_T, \mathcal{T})$ scales (dashed blue, right panel) covering the result from single-differential q_T resummation, at the price of much larger uncertainties.

We conclude that with additional effort, e.g. applying the methods used in refs. [50, 92], it would be possible to fully reconcile the best possible predictions for both the differential shape and the cumulant of the double-differential spectrum. However, for our purposes we can simply use the appropriate scale setting for the observable of interest. In particular, if the experimental observable of interest has cumulant-like character in either q_T or $\mathcal{T}$, e.g. if large bins in either observable are considered, the double-differential profile setup given in this paper, using $(q_T^{\text{cut}}, \mathcal{T})$ or $(q_T, \mathcal{T}_{\text{cut}})$ scales as appropriate, will be completely sufficient.

JHEP03(2019)124

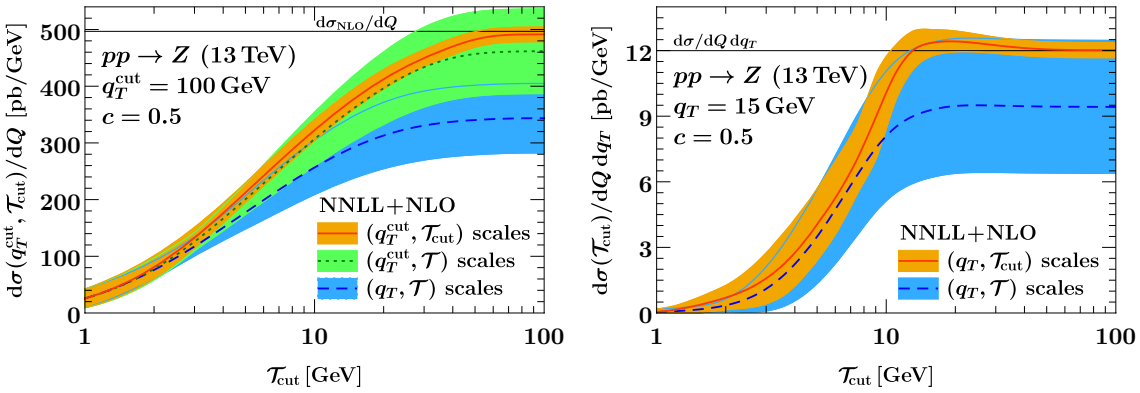

Figure 14. Left: the double cumulant cross section as a function of $\mathcal{T}_{\rm cut}$ for $q_T^{\rm cut} = 100\,\text{GeV}$ for different scale setting prescriptions, with a modified slope $c = 0.5$ of the SCET_I profile scales, see eq. (3.32). Right: the q_T spectrum with a cut on $\mathcal{T}$ as a function of $\mathcal{T}_{\rm cut}$ for different scale setting prescriptions, also using modified SCET_I profile scales with $c = 0.5$. The bands indicate the total perturbative uncertainty $\Delta_{\rm total}$, see section 3.4.

4 Results

In this section we present our results for Drell-Yan production $pp \to Z/\gamma^* \to \ell^+\ell^-$ at the LHC, with a simultaneous measurement of the transverse momentum q_T of the lepton pair and the 0-jettiness event shape $\mathcal{T}$. The center-of-mass energy is taken to be $E_{\rm cm} = 13\,\text{TeV}$. We assume that in addition, the invariant mass Q of the lepton pair is measured, and write $pp \to Z$ for short if $Q = m_Z$, and $pp \to Z^*$ otherwise. The subsequent decay and the contribution from the virtual photon are included in either case.

To obtain numerical results for the SCET_I, SCET_II, and SCET_+ contributions, we have implemented all pieces of the relevant double-differential factorized cross sections to $\mathcal{O}(\alpha_s)$ and their RGEs to NNLL in `SCETlib` [54]. The fixed NLO contributions in full QCD are obtained from `MCFM 8.0` [55–57]. We make use of the `MMHT2014nnlo68cl` [58] NNLO PDFs with five-flavor running and $\alpha_s(m_Z) = 0.118$. Since we focus on the perturbative calculation and do not include any nonperturbative effects, we provide the results down to 1 GeV in q_T and $\mathcal{T}$.

The outline of this section is as follows: in section 4.1 we present our fully resummed prediction for the double-differential spectrum, both as surface plots over the $(q_T, \mathcal{T})$ plane and for selected slices along lines of constant q_T or $\mathcal{T}$. We demonstrate that our prediction smoothly interpolates between the SCET_I and SCET_II boundary theories, i.e., we show that our matching formula in eq. (3.5) recovers the matched predictions on either boundary and improves over them by an additional resummation of power-suppressed terms. Finally, in section 4.2 we present our predictions for the single-differential spectra $d\sigma(q_T^{\rm cut})/d\mathcal{T}$ and $d\sigma(\mathcal{T}_{\rm cut})/dq_T$ with a cut on the other variable, and show how they recover the inclusive single-differential $\mathcal{T}$ and q_T spectra for large values of $q_T^{\rm cut}$ and $\mathcal{T}_{\rm cut}$, respectively.

JHEP03(2019)124

4.1 Double spectrum and comparison with boundary theories

To highlight the necessity of the simultaneous resummation of large logarithms of both q_T and $\mathcal{T}$, we start by showing results for the double spectrum (the cross section double-differential in q_T and $\mathcal{T}$) where only some of the logarithms are resummed. These results are shown as surface plots in figure 15, where we plot the double-differential spectrum with respect to $\log_{10} q_T$ and $\log_{10} \mathcal{T}$ for better visibility. In each case the left rear wall of the surface plot shows the result of integrating the double-differential spectrum up to $\mathcal{T}_{\text{cut}} = 100\,\text{GeV}$, but staying differential in $\log_{10} q_T$. Similarly, the right rear wall shows the projection onto the single-differential spectrum in $\log_{10} \mathcal{T}$, with a cut at $q_T^{\text{cut}} = 100\,\text{GeV}$.[5]

The top left panel of figure 15 shows the spectrum evaluated at fixed $\mathcal{O}(\alpha_s)$, without any resummation. The double-differential fixed-order spectrum diverges logarithmically for small $\mathcal{T}$ at any value of q_T, while its projections onto the single-differential spectra in q_T and $\mathcal{T}$ feature double-logarithmic singularities. Notably, the double-differential spectrum has a sharp kinematic edge along $q_T = \mathcal{T}$. This sharp edge is unphysical because it only reflects the kinematics of a single on-shell emission with transverse momentum k_T at rapidity η, which contributes at most $\mathcal{T} = k_T\, e^{-|\eta|} \leq k_T = q_T$. Due to the vectorial nature of q_T, however, back-to-back emissions can populate the region $\mathcal{T} > q_T$ at higher orders, and the kinematic edge must be smeared out.

Next, we consider the cases in which only logarithms of one variable are resummed, while logarithms involving the auxiliary variable are treated at fixed order. In the middle panel of figure 15, we show the result of resumming logarithms of $\mathcal{T}$ using the SCET_I matched result in eq. (2.11). The resummation is performed at NNLL and is matched to full NLO, which we refer to as $\text{NNLL}_{\mathcal{T}}$+NLO. As discussed in section 2.2, this prediction is valid as long as the parametric relation $\mathcal{T} \ll q_T \sim \sqrt{Q\mathcal{T}}$ is satisfied. This corresponds to the SCET_I phase-space boundary (blue) in figure 2, running from the region of small $\mathcal{T}$ and intermediate q_T towards the fixed-order region where $q_T \sim \mathcal{T} \sim Q$. It is clear that away from its region of validity, the $\text{NNLL}_{\mathcal{T}}$+NLO result contains unresummed logarithms of q_T because at any point in $\mathcal{T}$, the prediction diverges for very small q_T. In particular, power corrections of $\mathcal{O}(\mathcal{T}^2/q_T^2)$ are only captured by the fixed-order matching. They become $\mathcal{O}(1)$ as one approaches the diagonal $\mathcal{T} = q_T$ (the green line in figure 2), and encode the phase-space boundary at $q_T \sim \mathcal{T}$. As in the NLO case, treating this phase-space boundary at fixed order leads to the sharp kinematic edge along the diagonal; physically, the all-order tower of collinear emissions that contribute to q_T in SCET_I cannot resolve the boundary because it arises from the dynamics at central rapidities. The projections onto the rear walls highlight that only $\mathcal{T}$ is resummed. The single-differential q_T spectrum still diverges as $q_T \to 0$, while the $\mathcal{T}$ spectrum features a physical Sudakov peak.

In the bottom panel of figure 15, we show the result of resumming logarithms of (the b_T variable conjugate to) q_T to NNLL and matching to fixed NLO, using the SCET_II matched result in eq. (2.29). We denote this order by NNLL_{q_T}+NLO. This result is valid for $\mathcal{T} \sim q_T \ll \sqrt{Q\mathcal{T}}$, i.e., around the SCET_II phase-space boundary (green) in figure 2, where we find the onset of a Sudakov peak from the q_T resummation and a smooth kinematic

[5] We refer the reader to section 3.5 for the precise way we perform these integrals.

JHEP03(2019)124

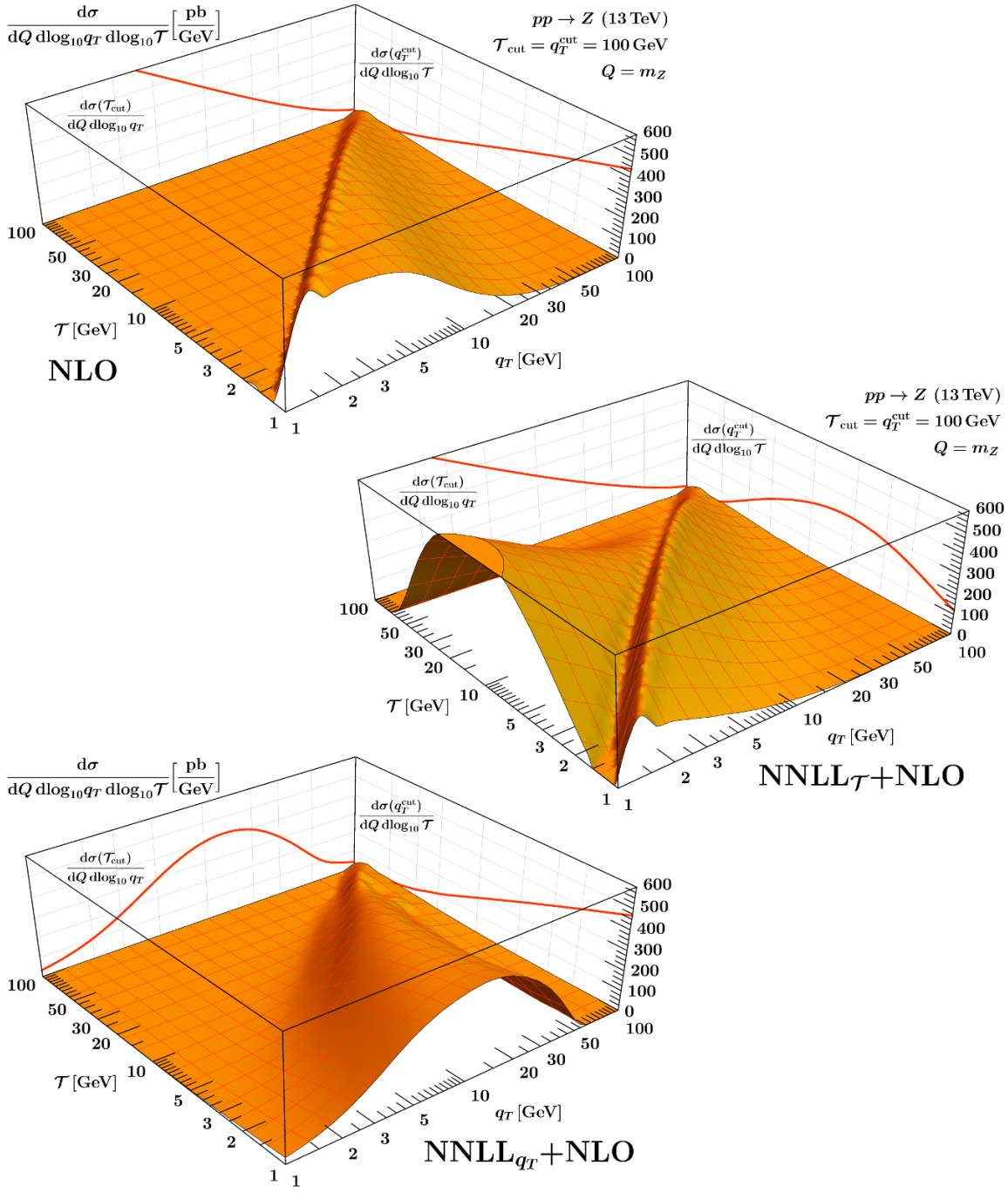

Figure 15. The double-differential Drell-Yan cross section at fixed NLO (top), resummed NNLL$_{\mathcal{T}}$+NLO (center), and NNLL$_{q_T}$+NLO (bottom). The resummed predictions are obtained by using only SCET$_{\rm I}$ (SCET$_{\rm II}$) renormalization group evolution to resum logarithms of $\mathcal{T}$ (q_T), as outlined in section 2.2 (section 2.3), and matching the result to the fixed-order cross section. For better visibility we show the spectrum with respect to $\log_{10} q_T$ and $\log_{10} \mathcal{T}$. On the rear walls we show the result of integrating the double spectrum over either variable up to a cut at 100 GeV.

JHEP03(2019)124

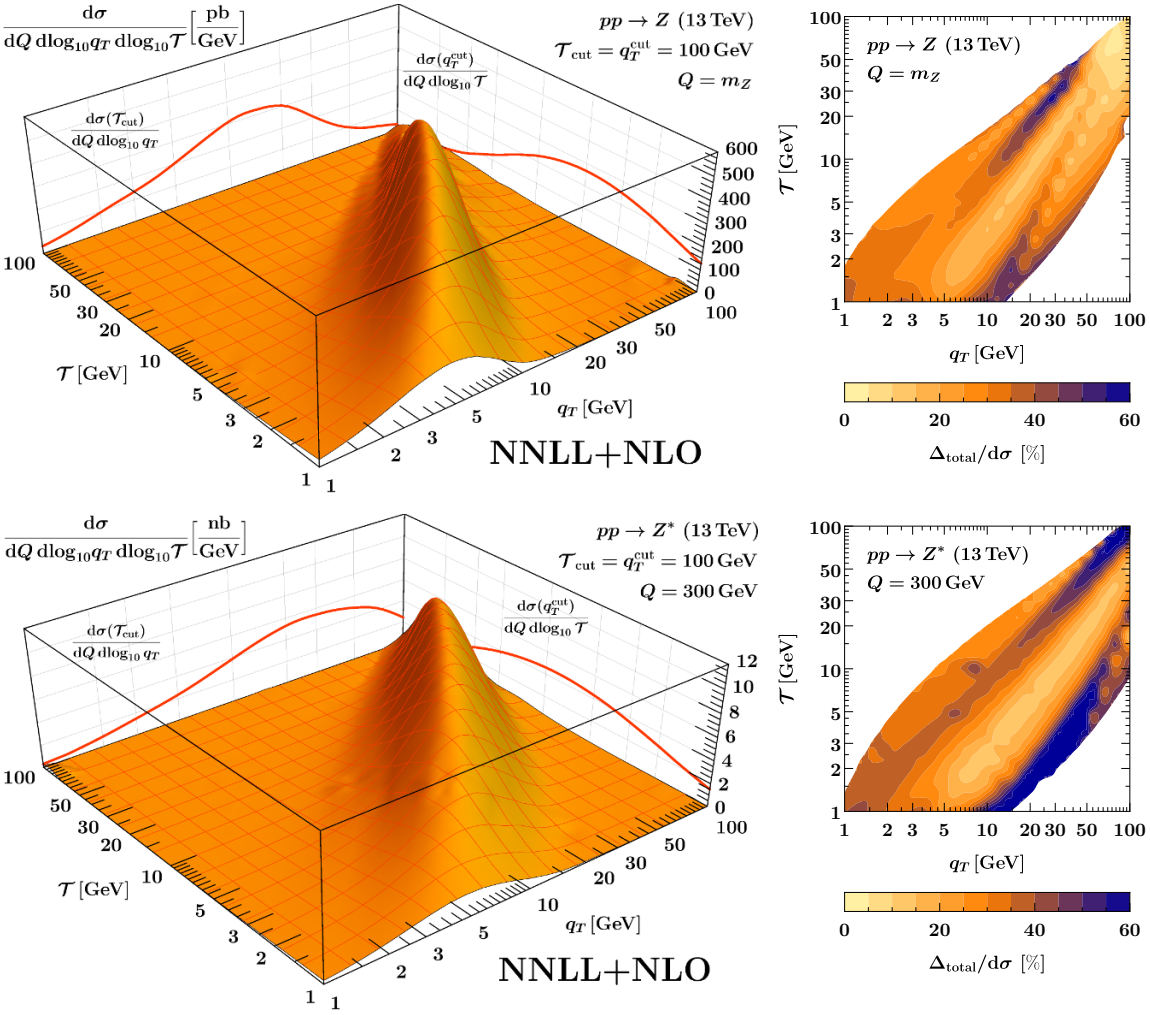

Figure 16. The double-differential Drell-Yan cross section at NNLL+NLO, at $Q = m_Z$ (top) and $Q = 300\,\text{GeV}$ (bottom), with respect to $\log_{10} q_T$ and $\log_{10} \mathcal{T}$. On the rear walls we show the result of integrating the double spectrum over either variable up to a cut at 100 GeV. The contour plots indicate total perturbative uncertainties relative to the cross section, $\Delta_{\text{total}} = \Delta_+ \oplus \Delta_{\text{I}} \oplus \Delta_{\text{II}} \oplus \Delta_{\text{FO}}$. The contour plots are left blank in the region where $d\sigma/(dQ\, d\log_{10} q_T\, d\log_{10} \mathcal{T})$ is less than 3% of its peak height.

suppression towards $\mathcal{T} \gg q_T$. However, the NNLL$_{q_T}$+NLO result diverges for smaller values of $\mathcal{T}$. This is due to unresummed logarithms of $\mathcal{T}$ in both the factorized cross section in SCET$_{\text{II}}$ and terms of $\mathcal{O}(q_T^2/(Q\mathcal{T}))$ that are treated at fixed order as part of the matching correction. In this case the single-differential projections show a Sudakov peak in q_T, but a logarithmic divergence at small $\mathcal{T}$.

Our final results for the Drell-Yan double spectrum are shown in figure 16, as given by the fully matched prediction in eq. (3.5). Here all resummed contributions are evaluated at NNLL, and we match to fixed NLO. This achieves, for the first time, the complete resummation of all large logarithms in the double spectrum, so we simply refer to this order as NNLL+NLO. The top row of plots is for $Q = m_Z$, i.e., for Drell-Yan production at the

JHEP03(2019)124

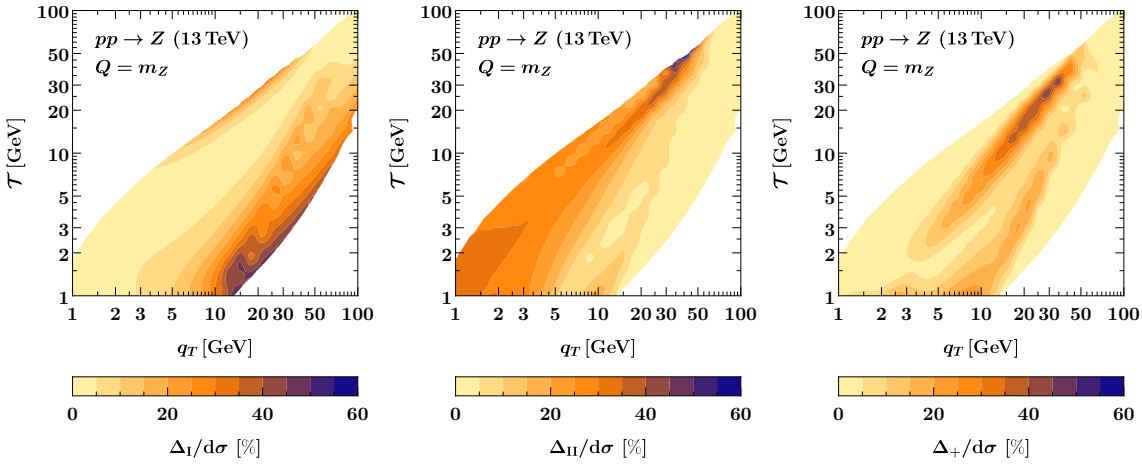

Figure 17. Breakdown of resummation uncertainties contributing to the relative uncertainty in the top right panel of figure 16, showing (from left to right) $\Delta_{\rm I}$, $\Delta_{\rm II}$, and Δ_{+}. As in figure 16 we leave regions blank where the cross section is small.

Z pole. In the bottom row we consider $Q = 300\,\text{GeV}$ as a representative phase-space point at higher production energies. Our matched and fully resummed double spectrum features a two-dimensional Sudakov peak that is situated between the two parametric phase-space boundaries (cf. figure 2), is smoothly suppressed beyond, and shifts towards higher values of q_T and $\mathcal{T}$ for $Q = 300\,\text{GeV}$, as expected. Integrating the double spectrum over either variable also results in a physical Sudakov peak, as can be seen from the projections onto the rear walls. Up to small differences in scale setting discussed in section 3.5, the left and right rear walls agree with the result of integrating the NNLL$_{q_T}$+NLO and NNLL$_{\mathcal{T}}$+NLO results in figure 15 over $\mathcal{T}$ and q_T, respectively. The contour plots in figure 16 show the total perturbative uncertainties $\Delta_{\rm total}$ as percent deviations from the central result for the double spectrum. As described in section 3.4, $\Delta_{\rm total}$ combines estimates of all sources of resummation uncertainty in the prediction.

In figure 17, we break down the uncertainty for the Drell-Yan double-differential spectrum at $Q = m_Z$ into its contributions from SCET$_{\rm I}$, SCET$_{\rm II}$ and SCET$_{+}$ resummation uncertainties, respectively. As expected, the SCET$_{\rm I}$ resummation uncertainty dominates in the SCET$_{\rm I}$ region of phase space, and similarly for SCET$_{\rm II}$. The SCET$_{+}$ resummation uncertainty is largest along the phase-space boundaries, indicating that it is mostly sensitive to variations of the transition points, i.e., the points where the intrinsic SCET$_{+}$ resummation is turned off in our matched prediction.

To further highlight the differences between our fully double-differential resummation and the single-differential resummation at either NNLL$_{q_T}$ or NNLL$_{\mathcal{T}}$, we take slices of the surface plots and overlay them in figure 18, keeping q_T (left) or $\mathcal{T}$ (right) fixed. The solid red curve corresponds to the matched and fully resummed cross section in eq. (3.5), with the uncertainty band given by the total perturbative uncertainty $\Delta_{\rm total}$, see eq. (3.26). The matched SCET$_{\rm I}$ (dashed blue) and SCET$_{\rm II}$ (dotted green) predictions correspond to the middle and bottom panel of figure 15, respectively. Their uncertainty bands are given

JHEP03(2019)124

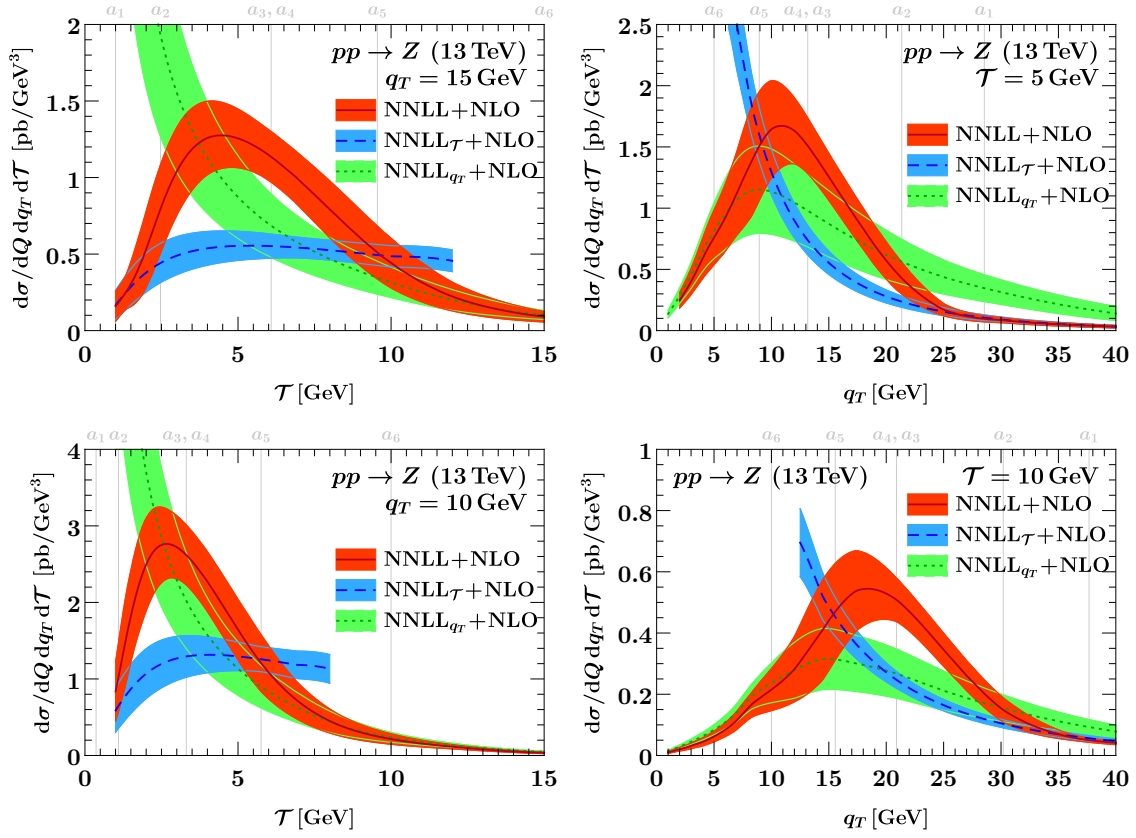

Figure 18. The double-differential Drell-Yan cross section for fixed q_T, as a function of $\mathcal{T}$ (left) and for fixed $\mathcal{T}$, as a function of q_T (right). The solid red curves are slices of the surface plots shown in the top left panel in figure 16, up to Jacobians. The blue dashed (green dotted) curve corresponds to the middle (bottom) panel of figure 15. The thin vertical lines indicate the transition points a_i described in section 3.3. The SCET$_{\rm I}$ prediction (dashed blue) has an unphysical edge at $\mathcal{T} = q_T$, see figure 15, and is not shown beyond $\mathcal{T} = 0.8\, q_T$ to avoid distraction. See the text for details on the uncertainty bands.

by $\Delta^{\rm I}_{\rm total}$ and $\Delta^{\rm II}_{\rm total}$, which only probe a subset of higher-order terms as predicted by the respective RGE, see eqs. (2.18) and (2.37). The SCET$_{\rm I}$ prediction features an unphysical sharp edge at $\mathcal{T} = q_T$, cf. the middle panel of figure 15, and for this reason is cut off at $\mathcal{T} = 0.8\, q_T$.

All panels in figure 18 show that our final prediction smoothly interpolates between the SCET$_{\rm I}$ and SCET$_{\rm II}$ boundary theories, both for the central values and for the uncertainties. Specifically, the matched prediction tends towards SCET$_{\rm I}$ (SCET$_{\rm II}$) for small (large) values of $\mathcal{T}$ and large (small) values of q_T. In the left column one clearly sees that SCET$_{\rm II}$ only captures logarithms of $\mathcal{T}$ at fixed order, leading to a diverging spectrum as $\mathcal{T} \to 0$, while the complete NNLL result features a physical Sudakov peak. Conversely, the SCET$_{\rm I}$ result diverges as $q_T \to 0$, but is rendered physical by the additional q_T resummation at NNLL.

We would like to stress that our fully resummed prediction does not exactly agree with either boundary theory, even beyond the final transition points a_1 and a_6 where the

JHEP03(2019)124

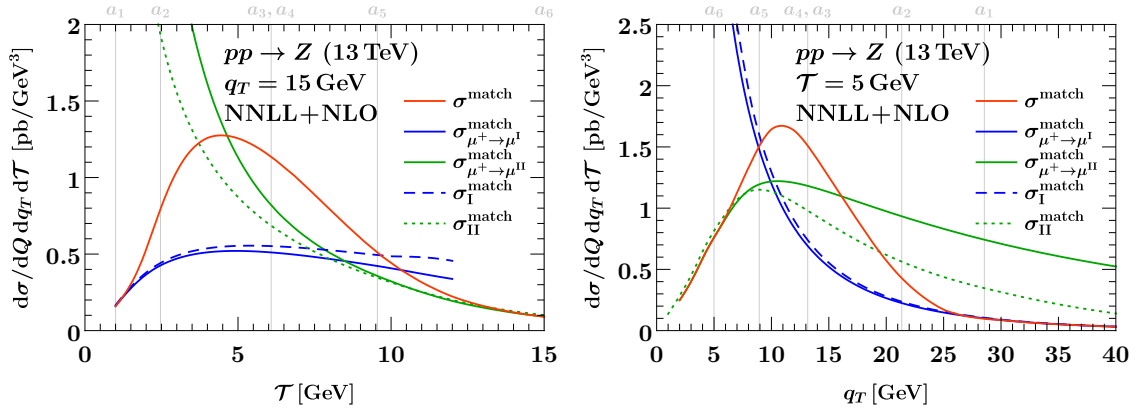

Figure 19. Slices of the double-differential Drell-Yan cross section at $q_T = 15\,\text{GeV}$ (left) and $\mathcal{T} = 5\,\text{GeV}$ (right). The solid red, dashed blue, and dotted green curves are identical to the central results in figure 18. The solid blue and green curves depict the SCET_I and SCET_II limits of our fully resummed result, given in eqs. (3.12) and (3.14). The thin vertical lines indicate the transition points a_i described in section 3.3.

intrinsic SCET_+ resummation is turned off. The reason for this is that even in these limits, the matched cross section in eq. (3.5) improves over the matched SCET_I and SCET_II cross sections in eq. (2.11) and eq. (2.29) by an additional resummation of power-suppressed terms, cf. eqs. (3.12) and (3.14). To assess the size of this effect, we again compare both single-differential resummations (dashed blue and dotted green) to our matched prediction (solid red) in figure 19, but for reference include the case where σ_+ in the matched prediction is evaluated at μ^I (solid blue) or μ^II (solid green) directly. One can easily verify from e.g. the right panel that for q_T above the right-most vertical line (where $a < a_1$), the difference between the solid blue and the dashed blue curves indeed amounts to a small power-suppressed set of higher-order terms, while our best prediction (solid red) recovers the solid blue curve as it must. Similarly, for q_T below the left-most vertical line (where $a > a_6$), the difference between the solid green (and solid red) and dashed green curves can be seen to be a small correction, reflecting the size of power-suppressed higher-order terms predicted by the SCET_I RGE in this region. The asymptotic limits are interchanged in the left panel, where $a < a_1$ towards the left and $a > a_6$ towards the very right of the plot.

4.2 Single-differential spectra with a cut on the other variable

So far we have turned our attention to the cross section differential in both q_T and $\mathcal{T}$. In addition to this double spectrum, our setup also predicts the fully matched and resummed double cumulant cross section, and the single-differential q_T (or $\mathcal{T}$) spectrum with a cut on the other variable; selected results for these observables where already discussed in section 3.5 from a more technical point of view. In figure 20, we show some more detailed results for the single-differential spectra with an additional cut, where the left panel shows $\mathrm{d}\sigma(q_T^{\text{cut}})/\mathrm{d}\mathcal{T}$ as a function of $\mathcal{T}$ for various values of q_T^{cut}, and the right panel shows $\mathrm{d}\sigma(\mathcal{T}_{\text{cut}})/\mathrm{d}q_T$ as a function of q_T for various values of $\mathcal{T}_{\text{cut}}$. By increasing the value of the cut, they can be seen to approach the inclusive single-differential spectra (orange solid),

JHEP03(2019)124

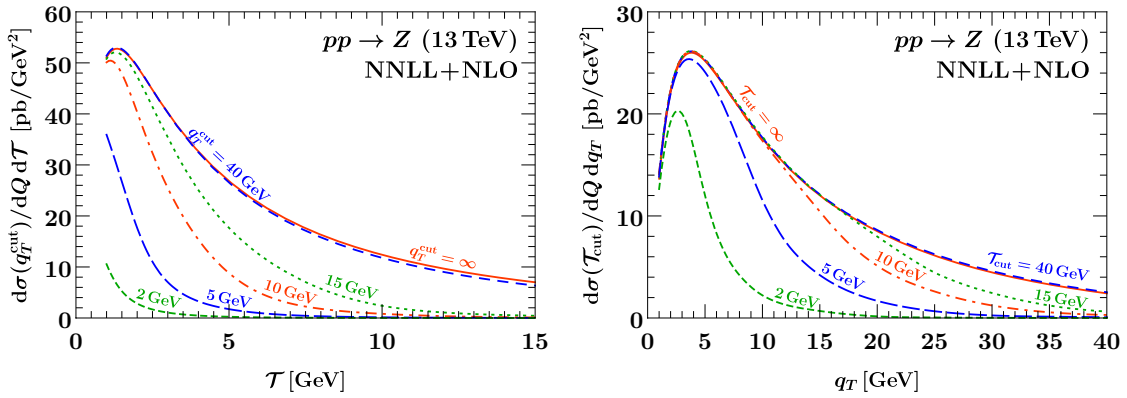

Figure 20. The single-differential $\mathcal{T}$ (left) and q_T (right) spectrum with a cut on the other variable at NNLL+NLO. The different curves represent different values of the cut. The solid orange lines correspond to the inclusive single-differential spectrum obtained by lifting the cut.

with which they must agree when sending $q_T^{\rm cut} \to \infty$ or $\mathcal{T}_{\rm cut} \to \infty$, respectively. This is by construction because we employ cumulant scale setting as appropriate for this prediction, cf. section 3.5. We observe that cuts on the other variable shape either spectrum in a very nontrivial way. Tight cuts $\lesssim 10\,\mathrm{GeV}$ push the peak to lower values and suppress the tail, where the q_T spectrum is somewhat more resilient to cuts on $\mathcal{T}$ than vice versa. Intermediate cuts $\sim$ 10–15 GeV keep the peak and mostly lead to a suppression in the tail, while the effect of cuts $\gtrsim 40\,\mathrm{GeV}$ is almost negligible in the q_T and $\mathcal{T}$ ranges of interest.

5 Conclusions

In this paper we calculated the Drell-Yan cross section double-differential in the transverse momentum q_T of the lepton pair and the 0-jettiness $\mathcal{T}$. Both $\mathcal{T}$ and q_T probe the initial state radiation, leading to Sudakov double logarithms of $\mathcal{T}/Q$ and q_T/Q in the cross section. We performed, for the first time, the simultaneous resummation of both kinds of logarithms, achieving next-to-next-to-leading logarithmic accuracy and matching the result to next-to-leading fixed order. We accomplish this resummation by using $\mathrm{SCET_I}$ and $\mathrm{SCET_{II}}$ to describe the regions $\mathcal{T} \ll q_T \sim \sqrt{\mathcal{T}Q}$ and $\mathcal{T} \sim q_T \ll \sqrt{\mathcal{T}Q}$, respectively, and $\mathrm{SCET_+}$ to describe the bulk of phase space in between these boundaries [51].

Obtaining reliable numerical predictions required several nontrivial steps: (1) Matching several factorized cross sections for the different regions of phase space, for which we use a Venn-diagram method to avoid double counting. (2) Choosing appropriate profile scales for the various ingredients in the factorization formulas that respect all relevant canonical scaling relations and at the same time smoothly interpolate between the different regions of phase space, and varying these scales to estimate perturbative uncertainties. This is significantly more involved than in the usual single-differential case, and is further complicated by the requirement to choose scales in impact parameter (b_T) space for $\mathrm{SCET_{II}}$. For example, the rapidity scale for the collinear-soft function in $\mathrm{SCET_+}$ has a canonical scaling that does not coincide with any scale on the $\mathrm{SCET_I}$ and $\mathrm{SCET_{II}}$ boundaries. (3) Ensuring

JHEP03(2019)124

that scales and scale variations are still, to the extent possible, inherited from the single-differential resummation of $\mathcal{T}$ and q_T. This makes our setup flexible enough to incorporate other procedures for estimating the uncertainty in the individual resummations. (4) To handle the transition between $\mathrm{SCET_I}$, $\mathrm{SCET_+}$ and $\mathrm{SCET_{II}}$, we introduced profile scales in terms of a regime parameter a, designed such that $a = 1$ for $\mathrm{SCET_I}$ and $a = 2$ for $\mathrm{SCET_{II}}$. The precise transition points in a were chosen by comparing the various singular and nonsingular cross section, and are varied as part of the uncertainty estimate. (5) We also introduced a new hybrid (i.e., q_T and b_T dependent) scale choice for q_T resummation, allowing the resummation to strictly take place in b_T space, while turning the resummation on and off using q_T.

We demonstrated that our simultaneous resummation of $\mathcal{T}$ and q_T yields the correct resummed single-differential cross sections after integrating over either $\mathcal{T}$ or q_T. This requires choosing scales at the level of the differential or integrated (cumulative) cross section as appropriate, which we discussed in detail.

While the predictions obtained here are of some direct phenomenological interest, as $\mathcal{T}$ has been measured in bins of q_T [48], our analysis is also an important step towards precise *and* differential predictions for LHC cross sections in general. Specifically, the Monte Carlo event generator GENEVA [49, 50] is based on a NNLL$'$ resummed prediction for the cross section differential in $\mathcal{T}$, and would benefit from the simultaneous resummation of q_T. Indeed, our NNLL results clearly indicate that only resumming the logarithms of either $\mathcal{T}$ or q_T gives a poor description of the double-differential cross section. Our methods apply at any order and for any color-singlet production process, allowing for a straightforward extension once the relevant perturbative ingredients become available. We hope that our analysis can pave the way for going beyond single-differential resummations in many other contexts as well.

Acknowledgments

We thank Goutam Das, Markus Diehl, and Markus Ebert for discussions. We would also like to thank Markus Ebert for his contributions to `SCETlib`. This work is supported by the ERC grant ERC-STG-2015-677323 and the D-ITP consortium, a program of the Netherlands Organization for Scientific Research (NWO) that is funded by the Dutch Ministry of Education, Culture and Science (OCW). FT and JM thank Nikhef for hospitality. GL thanks DESY for hospitality and the DESY theory group thanks GL for an ample supply of Dutch pepernoten.

A Plus distributions and Fourier transform

We use the following standard plus distributions with dimensionless arguments,

$$\mathcal{L}_n(x) \equiv \left[\frac{\theta(x)\ln^n x}{x}\right]_+ = \lim_{\beta\to 0}\left[\frac{\theta(x-\beta)\ln^n x}{x} + \delta(x-\beta)\,\frac{\ln^{n+1}\beta}{n+1}\right], \tag{A.1}$$

$$\mathcal{L}^a(x) \equiv \left[\frac{\theta(x)}{x^{1-a}}\right]_+ = \lim_{\beta\to 0}\left[\frac{\theta(x-\beta)}{x^{1-a}} + \delta(x-\beta)\frac{x^a-1}{a}\right]. \tag{A.2}$$

JHEP03(2019)124

In intermediate steps we need a two-dimensional plus distribution originally defined in ref. [51],

$$\mathcal{L}_\Delta(x_1,x_2) \equiv \lim_{\beta\to 0} \frac{\mathrm{d}}{\mathrm{d}x_1}\frac{\mathrm{d}}{\mathrm{d}x_2}\Big[\theta(x_2-x_1^2)\theta(x_1-\beta)\ln x_1\,(\ln x_2-\ln x_1) + \frac{1}{4}\,\theta(x_1^2-x_2)\theta(x_2-\beta^2)\ln^2 x_2\Big]\,. \tag{A.3}$$

Our shorthands for distributions with dimensionful arguments in one spatial dimension are

$$\mathcal{L}_n(k,\mu) \equiv \frac{1}{\mu}\mathcal{L}_n\left(\frac{k}{\mu}\right)\,, \qquad \mathcal{L}^a(k,\mu) \equiv \frac{1}{\mu}\mathcal{L}^a\left(\frac{k}{\mu}\right)\,. \tag{A.4}$$

In terms of the second class of (power-like) plus distributions, we further define

$$\mathcal{V}_a(x) \equiv \frac{e^{-\gamma_E a}}{\Gamma(1+a)}\big[a\mathcal{L}^a(x)+\delta(x)\big]\,, \qquad \mathcal{V}_a(k,\mu) \equiv \frac{1}{\mu}\mathcal{V}_a\left(\frac{k}{\mu}\right)\,, \tag{A.5}$$

which have a group property, assuming identical boundary condition μ,

$$\int \mathrm{d}\ell\,\mathcal{V}_a(\ell,\mu)\,\mathcal{V}_b(k-\ell,\mu) = \mathcal{V}_{a+b}(k,\mu)\,, \qquad \mathcal{V}_0(k,\mu)=\delta(k)\,. \tag{A.6}$$

Shifting the boundary condition of $\mathcal{V}_a(k,\mu)$ from μ to μ' is also straightforward,

$$\mathcal{V}_a(k,\mu) = \left(\frac{\mu'}{\mu}\right)^a \mathcal{V}_a(k,\mu')\,. \tag{A.7}$$

We use the conventions from appendix C of ref. [77] for logarithmic plus distributions in two integer spatial dimensions, with $k_T^2 \equiv \vec{k}_T^2 \geq 0$,

$$\delta(\vec{k}_T) = \frac{1}{\pi}\delta(k_T^2)\,, \qquad \mathcal{L}_n(\vec{k}_T,\mu) \equiv \frac{1}{\pi\mu^2}\left[\frac{\mu^2}{k_T^2}\ln^n\left(\frac{k_T^2}{\mu^2}\right)\right]_+^\mu \equiv \frac{1}{\pi\mu^2}\mathcal{L}_n\left(\frac{k_T^2}{\mu^2}\right)\,. \tag{A.8}$$

Our convention for the two-dimensional Fourier transform also follows ref. [77],

$$\frac{\mathrm{d}f}{\mathrm{d}\vec{p}_T} = \int\frac{\mathrm{d}^2\vec{b}_T}{(2\pi)^2}\,e^{+i\vec{p}_T\cdot\vec{b}_T}\,\tilde{f}(\vec{b}_T)\,, \qquad \tilde{f}(\vec{b}_T) = \int \mathrm{d}^2\vec{p}_T\,e^{-i\vec{p}_T\cdot\vec{b}_T}\,\frac{\mathrm{d}f}{\mathrm{d}\vec{p}_T}\,. \tag{A.9}$$

Here we make the mass dimension of $\mathrm{d}f/\mathrm{d}\vec{p}_T = \mathrm{d}f/(\mathrm{d}p_x\,\mathrm{d}p_y)$ explicit. If f is azimuthally symmetric, i.e., if for $p_T \equiv |\vec{p}_T|, b_T \equiv |\vec{b}_T|$,

$$\frac{\mathrm{d}f}{\mathrm{d}\vec{p}_T} = \frac{1}{2\pi p_T}\frac{\mathrm{d}f}{\mathrm{d}p_T}\,, \qquad \tilde{f}(\vec{b}_T) = \tilde{f}(b_T)\,, \tag{A.10}$$

the azimuthal integral can be performed, leaving

$$\frac{\mathrm{d}f}{\mathrm{d}p_T} = p_T\int_0^\infty \mathrm{d}b_T\,b_T\,J_0(b_T p_T)\,\tilde{f}(b_T)\,, \qquad \tilde{f}(b_T) = \int_0^\infty \mathrm{d}p_T\,J_0(b_T p_T)\frac{\mathrm{d}f}{\mathrm{d}p_T}\,, \tag{A.11}$$

where $J_0(x)$ is the zeroth-order Bessel function of the first kind. Integrating the first expression in eq. (A.11) by parts, the cumulant in p_T is given by

$$\int_0^{p_T^{\mathrm{cut}}}\mathrm{d}p_T\,\frac{\mathrm{d}f}{\mathrm{d}p_T} = p_T^{\mathrm{cut}}\int_0^\infty \mathrm{d}b_T\,J_1(b_T p_T^{\mathrm{cut}})\,\tilde{f}(b_T)\,, \tag{A.12}$$

JHEP03(2019)124

where $J_1(x)$ is the first-order Bessel function of the first kind. Fourier transforms of $\mathcal{L}_n(\vec{p}_T,\mu)$ can be found in table 5 of ref. [77], and are most conveniently expressed in terms of

$$L_b \equiv \ln\frac{b_T^2\mu^2}{b_0^2}\,, \qquad b_0 \equiv 2e^{-\gamma_E} \approx 1.12291\ldots\,. \tag{A.13}$$

B Perturbative ingredients

B.1 Anomalous dimensions

We expand the β function of QCD as

$$\mu\frac{\mathrm{d}\alpha_s(\mu)}{\mathrm{d}\mu} = \beta[\alpha_s(\mu)]\,, \qquad \beta(\alpha_s) = -2\alpha_s\sum_{n=0}^{\infty}\beta_n\left(\frac{\alpha_s}{4\pi}\right)^{n+1}\,. \tag{B.1}$$

The coefficients in the $\overline{\text{MS}}$ scheme are, up to three loops [93, 94],

$$\begin{aligned}
\beta_0 &= \frac{11}{3}C_A - \frac{4}{3}T_F\,n_f\,, \qquad \beta_1 = \frac{34}{3}C_A^2 - \left(\frac{20}{3}C_A + 4C_F\right)T_F\,n_f\,, \\
\beta_2 &= \frac{2857}{54}C_A^3 + \left(C_F^2 - \frac{205}{18}C_FC_A - \frac{1415}{54}C_A^2\right)2T_F\,n_f + \left(\frac{11}{9}C_F + \frac{79}{54}C_A\right)4T_F^2\,n_f^2\,.
\end{aligned} \tag{B.2}$$

We work with $n_f = 5$ light flavors. The cusp and noncusp anomalous dimensions are expanded as

$$\Gamma^i_{\text{cusp}}(\alpha_s) = \sum_{n=0}^{\infty}\Gamma^i_n\left(\frac{\alpha_s}{4\pi}\right)^{n+1}\,, \qquad \gamma(\alpha_s) = \sum_{n=0}^{\infty}\gamma_n\left(\frac{\alpha_s}{4\pi}\right)^{n+1}\,. \tag{B.3}$$

The coefficients of the $\overline{\text{MS}}$ cusp anomalous dimension to three loops are [95–97]

$$\begin{aligned}
\Gamma^i_0 &= 4C_i\,, \\
\Gamma^i_1 &= 4C_i\left[C_A\left(\frac{67}{9} - \frac{\pi^2}{3}\right) - \frac{20}{9}T_F\,n_f\right] = \frac{4}{3}C_i\left[(4-\pi^2)C_A + 5\beta_0\right]\,, \\
\Gamma^i_2 &= 4C_i\left[C_A^2\left(\frac{245}{6} - \frac{134\pi^2}{27} + \frac{11\pi^4}{45} + \frac{22\zeta_3}{3}\right) + C_A\,T_F\,n_f\left(-\frac{418}{27} + \frac{40\pi^2}{27} - \frac{56\zeta_3}{3}\right)\right. \\
&\quad \left. + C_F\,T_F\,n_f\left(-\frac{55}{3} + 16\zeta_3\right) - \frac{16}{27}T_F^2\,n_f^2\right]\,,
\end{aligned} \tag{B.4}$$

where here and in the following $C_i = C_F\,(C_A)$ for $i = q\,(g)$. The fixed-order boundary condition of the resummed rapidity anomalous dimension eq. (2.26) reads, through NNLL,

$$\tilde{\gamma}^i_{\nu,\text{FO}}(b_T,\mu) = \frac{\alpha_s(\mu)}{4\pi}\left[-2\Gamma^i_0L_b\right] + \frac{\alpha_s^2(\mu)}{(4\pi)^2}\left[-\Gamma^i_0\beta_0L_b^2 - 2\Gamma^i_1L_b + \gamma^i_{\nu\,1}\right] + \mathcal{O}(\alpha_s^3)\,, \tag{B.5}$$

where we have already used that $\gamma^i_{\nu\,0} = 0$. For our choice of regulator, the two-loop boundary condition is given by [70]

$$\gamma^i_{\nu\,1} = C_i\left[-C_A\left(\frac{128}{9} - 56\zeta_3\right) - \beta_0\frac{112}{9}\right]\,. \tag{B.6}$$

JHEP03(2019)124

Hard function. The hard function $H_\kappa(Q,\mu)$ is proportional to the square of the hard matching coefficient [see eq. (B.21)]. The hard matching coefficient for $q\bar{q} \to Z/\gamma^*$ is renormalized as

$$\begin{aligned}\mu\frac{\mathrm{d}}{\mathrm{d}\mu}C_{q\bar{q}}^{V,A}(Q^2,\mu) &= \gamma_{q\bar{q}}^{V,A}(Q^2,\mu)\, C_{q\bar{q}}^{V,A}(Q^2,\mu)\,,\\ \gamma_{q\bar{q}}^{V,A}(Q^2,\mu) &= \Gamma_{\mathrm{cusp}}^{q}\big[\alpha_s(\mu)\big]\ln\frac{-Q^2-\mathrm{i}0}{\mu^2} + 2\gamma_C^q\big[\alpha_s(\mu)\big]\,.\end{aligned} \tag{B.7}$$

The coefficients of the quark noncusp anomalous dimension up to two loops are

$$\begin{aligned}\gamma_{C\,0}^q &= -3C_F\,,\\ \gamma_{C\,1}^q &= -C_F\left[C_A\left(\frac{41}{9}-26\zeta_3\right)+C_F\left(\frac{3}{2}-2\pi^2+24\zeta_3\right)+\beta_0\left(\frac{65}{18}+\frac{\pi^2}{2}\right)\right].\end{aligned} \tag{B.8}$$

Beam functions and PDFs. In b_T space, the TMD beam function is renormalized as

$$\begin{aligned}\mu\frac{\mathrm{d}}{\mathrm{d}\mu}\tilde{B}_q(\omega,b_T,\mu,\nu) &= \tilde{\gamma}_B^q(\omega,\mu,\nu)\,\tilde{B}_q(\omega,b_T,\mu,\nu)\,,\\ \nu\frac{\mathrm{d}}{\mathrm{d}\nu}\tilde{B}_q(\omega,b_T,\mu,\nu) &= -\frac{1}{2}\tilde{\gamma}_\nu^q(b_T,\mu)\,\tilde{B}_q(\omega,b_T,\mu,\nu)\,,\\ \tilde{\gamma}_B^q(\omega,\mu,\nu) &= 2\Gamma_{\mathrm{cusp}}^q[\alpha_s(\mu)]\ln\frac{\nu}{\omega}+\tilde{\gamma}_B^q[\alpha_s(\mu)]\,.\end{aligned} \tag{B.9}$$

We include a tilde to indicate that $\tilde{\gamma}_B^q$ is related to the $\mathrm{SCET_{II}}$ beam function, even though it does not depend on b_T. Its coefficients through two loops are [70]

$$\begin{aligned}\tilde{\gamma}_{B\,0}^q &= 6C_F\,,\\ \tilde{\gamma}_{B\,1}^q &= C_F\left[(2-24\zeta_3)C_A+(3-4\pi^2+48\zeta_3)C_F+\left(1+\frac{4\pi^2}{3}\right)\beta_0\right].\end{aligned} \tag{B.10}$$

The resummed rapidity anomalous dimension $\tilde{\gamma}_\nu^i(b_T,\mu)$ is given in eq. (2.26).

The double-differential beam function satisfies the same RGE as the inclusive $\mathrm{SCET_I}$ beam function,[6]

$$\begin{aligned}\mu\frac{\mathrm{d}}{\mathrm{d}\mu}B_q(t,x,\vec{k}_T,\mu) &= \int\mathrm{d}t'\,\gamma_B^q(t-t',\mu)\,B_q(t',x,\vec{k}_T,\mu)\,,\\ \gamma_B^q(t,\mu) &= -2\Gamma_{\mathrm{cusp}}^q(\alpha_s)\,\mathcal{L}_0(t,\mu^2)+\gamma_B^q[\alpha_s(\mu)]\,\delta(t)\,.\end{aligned} \tag{B.11}$$

The coefficients of the $\mathrm{SCET_I}$ quark beam anomalous dimension are [60, 98]

$$\begin{aligned}\gamma_{B\,0}^q &= 6C_F\,,\\ \gamma_{B\,1}^q &= C_F\left[\left(\frac{146}{9}-80\zeta_3\right)C_A+(3-4\pi^2+48\zeta_3)C_F+\left(\frac{121}{9}+\frac{2\pi^2}{3}\right)\beta_0\right].\end{aligned} \tag{B.12}$$

[6] We note that ref. [51] incorrectly did not distinguish between $\gamma_B^i(\alpha_s)$ and $\tilde{\gamma}_B^i(\alpha_s)$. This lead to the noncusp contribution to the collinear-soft anomalous dimension being missing in their eq. (3.26), cf. our corrected eq. (B.18) and the nonvanishing two-loop noncusp coefficient in our eq. (B.19).

JHEP03(2019)124

We also require the one-loop coefficients of the PDF anomalous dimension,

$$\mu\frac{\mathrm{d}}{\mathrm{d}\mu}f_i(x,\mu) = \sum_j \int_x^1 \frac{\mathrm{d}z}{z}\, 2P_{ij}[\alpha_s(\mu),z]\, f_j\Big(\frac{x}{z},\mu\Big)\,,$$
$$P_{ij}(\alpha_s,z) = \sum_{n=0}^{\infty} P_{ij}^{(n)}(z)\left(\frac{\alpha_s}{4\pi}\right)^{n+1}\,. \tag{B.13}$$

Note that we expand $P_{ij}(\alpha_s,z)$ in $\alpha_s/(4\pi)$. The one-loop coefficients are

$$P_{qq}^{(0)}(z) = 2C_F\,\theta(z)P_{qq}(z)\,,\quad P_{qg}^{(0)}(z) = 2T_F\,\theta(z)P_{qg}(z)\,, \tag{B.14}$$

in terms of the standard color-stripped one-loop QCD splitting functions

$$P_{qq}(z) = 2\mathcal{L}_0(1-z) - \theta(1-z)(1+z) + \frac{3}{2}\delta(1-z) = \left[\theta(1-z)\frac{1+z^2}{1-z}\right]_+\,,$$
$$P_{qg}(z) = \theta(1-z)\big[1-2z(1-z)\big]\,. \tag{B.15}$$

Soft and collinear-soft functions. The RGE of the beam thrust soft function reads

$$\mu\frac{\mathrm{d}}{\mathrm{d}\mu}S_i(k,\mu) = \int \mathrm{d}k'\,\gamma_S^i(k-k',\mu)\,S_i(k',\mu)\,,$$
$$\gamma_S^i(k,\mu) = 4\Gamma^i_{\mathrm{cusp}}(\alpha_s)\,\mathcal{L}_0(k,\mu) + \gamma_S^i[\alpha_s(\mu)]\,\delta(k)\,. \tag{B.16}$$

For the double-differential soft function in b_T space we have

$$\mu\frac{\mathrm{d}}{\mathrm{d}\mu}\tilde{S}_i(k,b_T,\mu,\nu) = \tilde{\gamma}_S^i(\mu,\nu)\,\tilde{S}_i(k,b_T,\mu,\nu)\,,$$
$$\nu\frac{\mathrm{d}}{\mathrm{d}\nu}\tilde{S}_i(k,b_T,\mu,\nu) = \tilde{\gamma}_\nu^i(b_T,\mu)\,\tilde{S}_i(k,b_T,\mu,\nu)\,,$$
$$\tilde{\gamma}_S^i(\mu,\nu) = 4\Gamma^i_{\mathrm{cusp}}(\alpha_s)\,\ln\frac{\mu}{\nu} + \tilde{\gamma}_S^i[\alpha_s(\mu)]\,, \tag{B.17}$$

where we again use a tilde on the μ anomalous dimension to indicate that it relates to the $\mathrm{SCET_{II}}$ soft function. The RGE of the collinear-soft function in b_T space reads

$$\mu\frac{\mathrm{d}}{\mathrm{d}\mu}\tilde{\mathcal{S}}_i(k,b_T,\mu,\nu) = \int \mathrm{d}k'\,\gamma_{\mathcal{S}}^i(k-k',\mu,\nu)\,\tilde{\mathcal{S}}_i(k',b_T,\mu,\nu)\,,$$
$$\nu\frac{\mathrm{d}}{\mathrm{d}\nu}\tilde{\mathcal{S}}_i(k,b_T,\mu,\nu) = \frac{1}{2}\tilde{\gamma}_\nu^i(b_T,\mu)\,\tilde{\mathcal{S}}_i(k,b_T,\mu,\nu)\,,$$
$$\gamma_{\mathcal{S}}^i(k,\mu,\nu) = -2\Gamma^i_{\mathrm{cusp}}(\alpha_s)\,\mathcal{L}_0\left(k,\frac{\mu^2}{\nu}\right) + \gamma_{\mathcal{S}}^i[\alpha_s(\mu)]\delta(k)\,. \tag{B.18}$$

The soft and collinear-soft noncusp anomalous dimension coefficients are only nonzero starting at two loops and can be inferred from consistency,

$$\gamma_{S\,0}^i = \gamma_{\mathcal{S}\,0}^i = \tilde{\gamma}_{S\,0}^i = 0\,,$$
$$-\gamma_{S\,1}^i = \gamma_{\mathcal{S}\,1}^i = \tilde{\gamma}_{S\,1}^i = C_i\left[C_A\left(\frac{128}{9} - 56\zeta_3\right) - \beta_0\left(\frac{112}{9} - \frac{2\pi^2}{3}\right)\right]\,. \tag{B.19}$$

JHEP03(2019)124

B.2 Fixed-order ingredients

Hard process. The Born cross section for $q\bar{q} \to Z/\gamma^* \to \ell^+\ell^-$ is given by

$$\frac{\mathrm{d}\sigma_B^q}{\mathrm{d}Q} = \frac{8\pi\alpha_{\mathrm{em}}^2}{3N_c E_{\mathrm{cm}}^2 Q}\left[Q_q^2 + \frac{(v_q^2+a_q^2)(v_\ell^2+a_\ell^2) - 2Q_q v_q v_\ell (1-m_Z^2/Q^2)}{(1-m_Z^2/Q^2)^2 + m_Z^2\Gamma_Z^2/Q^4}\right], \tag{B.20}$$

where Q_q is the quark charge in units of $|e|$, $v_{\ell,q}$ and $a_{\ell,q}$ are the standard vector and axial couplings of the leptons and quarks, and m_Z and Γ_Z are the mass and width of the Z boson. The one-loop Wilson coefficient $C_{q\bar{q}}^{V,A}(Q^2,\mu)$ from matching the quark current in QCD onto SCET was computed in refs. [99, 100]. This leads to the following hard function [46],

$$\begin{aligned} H_{ij}(Q,\mu) &= \sum_q \frac{\mathrm{d}\sigma_B^q}{\mathrm{d}Q}\left(\delta_{iq}\delta_{j\bar{q}} + \delta_{i\bar{q}}\delta_{jq}\right)|C_{q\bar{q}}^{V,A}(Q^2,\mu)|^2\,, \\ |C_{q\bar{q}}^{V,A}(Q^2,\mu)|^2 &= 1 + 2\,\mathrm{Re}\left\{\frac{\alpha_s(\mu)}{4\pi}C_F\left[-\ln^2\frac{Q^2}{\mu^2} + 3\ln\frac{Q^2}{\mu^2} - 8 + \frac{7\pi^2}{6}\right]\right\} + \mathcal{O}(\alpha_s^2)\,, \end{aligned} \tag{B.21}$$

where Re denotes the real part.

Beam functions. The one-loop matching coefficients for the single-differential $\mathrm{SCET_{II}}$ beam function in b_T space are given by [70, 101]

$$\begin{aligned} &\tilde{\mathcal{I}}_{qj}(\omega, b_T, z, \mu, \nu) \\ &= \delta_{qj}\delta(1-z) + \frac{\alpha_s(\mu)}{4\pi}\left[\delta_{qj}\delta(1-z)\left(\Gamma_0^q \ln\frac{\nu}{\omega} + \frac{\gamma_{B,0}^q}{2}\right)L_b - L_b P_{qj}^{(0)}(z) + \tilde{I}_{qj}^{(1)}(z)\right] + \mathcal{O}(\alpha_s^2)\,, \end{aligned} \tag{B.22}$$

where L_b was defined in eq. (A.13) and the boundary conditions at $L_b = 0, \nu = \omega$ are

$$\begin{aligned} \tilde{I}_{qq}^{(1)}(z) &= C_F\;\theta(z)\theta(1-z)\,2(1-z)\,, \\ \tilde{I}_{qg}^{(1)}(z) &= T_F\,\theta(z)\theta(1-z)\,4z(1-z)\,. \end{aligned} \tag{B.23}$$

As for its anomalous dimension, we use a tilde to indicate that these boundary conditions are part of the $\mathrm{SCET_{II}}$ beam function, even though they do not depend on b_T.

It is convenient to decompose the matching coefficients for the double-differential $\mathrm{SCET_I}$ quark beam function as

$$\mathcal{I}_{qj}(t,z,\vec{k}_T,\mu) = \delta(\vec{k}_T)\,\mathcal{I}_{qj}(t,z,\mu) + \Delta\mathcal{I}_{qj}(t,z,\vec{k}_T,\mu)\,, \tag{B.24}$$

where $\mathcal{I}_{qj}(t,z,\mu)$ is the matching coefficient for the inclusive quark beam function [46, 60],

$$\begin{aligned} \mathcal{I}_{qj}(t,z,\mu) &= \delta_{qj}\,\delta(t)\delta(1-z) \\ &\quad + \frac{\alpha_s}{4\pi}\Big[\Gamma_0^q\delta_{qj}\,\mathcal{L}_1(t,\mu^2)\,\delta(1-z) + \mathcal{L}_0(t,\mu^2)\,\tilde{P}_{qj}^{(0)}(z) + \delta(t)\,I_{qj}^{(1)}(z)\Big] + \mathcal{O}(\alpha_s^2)\,, \end{aligned} \tag{B.25}$$

with the finite terms in this case given by

$$\begin{aligned} I_{qq}^{(1)}(z) &= 2C_F\,\theta(z)\left[\mathcal{L}_1(1-z)(1+z^2) - \frac{\pi^2}{6}\delta(1-z) + \theta(1-z)\left(1-z-\frac{1+z^2}{1-z}\ln z\right)\right], \\ I_{qg}^{(1)}(z) &= 2T_F\,\theta(z)\left[P_{qg}(z)\left(\ln\frac{1-z}{z} - 1\right) + \theta(1-z)\right], \end{aligned} \tag{B.26}$$

JHEP03(2019)124

and using the shorthand

$$\tilde{P}_{qj}^{(0)}(z) \equiv P_{qj}^{(0)}(z) - \delta_{qj}\delta(1-z)\frac{\gamma_{B\,0}^{q}}{2} = \begin{cases} 2C_F\mathcal{L}_0(1-z)(1+z^2)\,, & j=q\,, \\ 2T_F\Big[(1-z)^2+z^2\Big]\,, & j=g\,. \end{cases}$$

The $\Delta\mathcal{I}_{qj}$ piece can be interpreted as a correction over the limit $t \ll k_T^2$, where recoil from collinear radiation is power suppressed and the double-differential beam function becomes proportional to $\delta(\vec{k}_T)$. Specifically, it scales as

$$\Delta\mathcal{I}_{qj}(t,z,\vec{k}_T,\mu) \sim \left[\frac{1}{t}\right]_+\left[\frac{1}{k_T^2}\right]_+ \times \mathcal{O}\left(\frac{t}{k_T^2}\right) \quad \text{for} \quad t \ll k_T^2\,, \tag{B.27}$$

and by construction satisfies

$$\int \mathrm{d}^2\vec{k}_T\,\Delta\mathcal{I}_{qj}(t,z,\vec{k}_T,\mu) = 0\,. \tag{B.28}$$

At one loop it can be extracted from the full calculation of $\mathcal{I}_{qj}(t,z,\vec{k}_T,\mu)$ [59, 102] and has the compact form

$$\begin{aligned} \Delta\mathcal{I}_{qj}(t,z,\vec{k}_T,\mu) &= \frac{\alpha_s(\mu)}{4\pi}\Delta I_{qj}^{(1)}(t,z,\vec{k}_T) + \mathcal{O}(\alpha_s^2)\,, \\ \Delta I_{qj}^{(1)}(t,z,\vec{k}_T) &= \frac{\theta(t)}{t}\tilde{P}_{qj}^{(0)}(z)\left[\frac{1}{\pi}\delta\Big(k_T^2 - \frac{1-z}{z}t\Big) - \delta(\vec{k}_T)\right]. \end{aligned} \tag{B.29}$$

The second line is regular in t because the term in square brackets vanishes as $t \to 0$. After accumulating over the transverse plane up to $q_T^{\mathrm{cut}} > 0$, we have

$$\int \mathrm{d}^2\vec{k}_T\,\theta(q_T^{\mathrm{cut}} - |\vec{k}_T|)\,\Delta I_{qj}^{(1)}(t,z,\vec{k}_T) = -\frac{\theta(t)}{t}\tilde{P}_{qj}^{(0)}(z)\,\theta\left[(q_T^{\mathrm{cut}})^2 < \frac{1-z}{z}t\right]. \tag{B.30}$$

Soft and collinear-soft functions. The (beam) thrust soft function is [46, 103, 104]

$$S_i(k,\mu) = \delta(k) + \frac{\alpha_s(\mu)}{4\pi}\left[-4\Gamma_0^i\,\mathcal{L}_1(k,\mu) + \frac{\pi^2}{3}C_i\,\delta(k)\right] + \mathcal{O}(\alpha_s^2)\,. \tag{B.31}$$

The one-loop collinear-soft function in b_T space is [51]

$$\begin{aligned} \tilde{\mathcal{S}}_i(k,b_T,\mu,\nu) = \delta(k) + \frac{\alpha_s(\mu)}{4\pi}\left\{-\Gamma_0^i L_b\,\mathcal{L}_0(k,\mu) + \Gamma_0^i\left[-\frac{1}{2}L_b^2 - L_b\ln\frac{\nu}{\mu}\right]\delta(k) - \frac{\pi^2}{3}C_i\,\delta(k)\right\} \\ + \mathcal{O}(\alpha_s^2)\,. \end{aligned} \tag{B.32}$$

It is again convenient to decompose the double-differential soft function computed in ref. [51] into separate pieces with distinct power counting,

$$S_i(k,\vec{k}_T,\mu,\nu) = \delta(k)\,S_i(\vec{k}_T,\mu,\nu) + \Delta S_i(k,\vec{k}_T,\mu,\nu)\,. \tag{B.33}$$

Here $S_i(\vec{k}_T,\mu,\nu)$ is the standard single-differential q_T soft function, which in b_T space at one loop is given by [69]

$$\tilde{S}_i(b_T,\mu,\nu) = 1 + \frac{\alpha_s(\mu)}{4\pi}\left[-\frac{\Gamma_0^i}{2}L_b^2 + 2\Gamma_0^i L_b\ln\frac{\mu}{\nu} - \frac{\pi^2}{3}C_i\right]. \tag{B.34}$$

JHEP03(2019)124

The second term in eq. (B.33) can again be interpreted as a correction, in this case over the limit $k \gg \vec{k}_T$ where the contribution of soft radiation to the $\mathcal{T} = k$ measurement becomes power suppressed. In momentum space this term satisfies

$$\int \mathrm{d}k\, \Delta S_i(k, \vec{k}_T, \mu, \nu) = 0\,,$$
$$\Delta S_i(k, \vec{k}_T, \mu, \nu) \sim \left[\frac{1}{k}\right]_+ \left[\frac{1}{k_T^2}\right]_+ \times \mathcal{O}\left(\frac{k_T^2}{k^2}\right) \quad \text{for} \quad k_T^2 \ll k^2\,. \tag{B.35}$$

Equivalently, in position space we have

$$\int \mathrm{d}k\, \Delta \tilde{S}_i(k, b_T, \mu, \nu) = 0\,,$$
$$\Delta \tilde{S}_i(k, b_T, \mu, \nu) \sim \left[\frac{1}{k}\right]_+ \times \mathcal{O}\left(\frac{1}{b_T^2 k^2}\right) \quad \text{for} \quad \frac{1}{b_T^2} \ll k^2\,. \tag{B.36}$$

At one loop, ΔS_i is given by

$$\Delta S_i(k, \vec{k}_T, \mu, \nu) = \frac{\alpha_s(\mu)}{4\pi} \Delta S_{i,1}(k, \vec{k}_T) + \mathcal{O}(\alpha_s^2)\,,$$
$$\Delta S_{i,1}(k, \vec{k}_T) = 4C_i \left[\frac{2}{\pi\mu^3} \mathcal{L}_\Delta\left(\frac{k}{\mu}, \frac{k_T^2}{\mu^2}\right) - \delta(k) \mathcal{L}_1(\vec{k}_T, \mu)\right]. \tag{B.37}$$

The second line is not yet manifestly independent of μ, but can be simplified noting that

$$\mathcal{L}_\Delta(x_1, x_2) - \delta(x_1)\mathcal{L}_1(x_2) = \frac{\mathrm{d}}{\mathrm{d}x_1} \frac{\mathrm{d}}{\mathrm{d}x_2} \theta(x_2 - x_1^2) \left[-\frac{1}{2} \ln^2 \frac{x_1^2}{x_2}\right]. \tag{B.38}$$

It is straightforward to show this by writing all three distributions in terms of $\theta(x_1 - \beta)$ and $\theta(x_2 - \beta^2)$ for infinitesimal β, collecting terms, and noting that the result is finite as $\beta \to 0$. From eq. (B.38) we can immediately read off the fixed-order double cumulant of $\Delta S_{i,1}$ for $\mathcal{T}_{\text{cut}} > 0$, $q_T^{\text{cut}} > 0$,

$$\int^{\mathcal{T}_{\text{cut}}} \mathrm{d}k \int \mathrm{d}^2 \vec{k}_T\, \theta(q_T^{\text{cut}} - |\vec{k}_T|)\, \Delta S_{i,1}(k, \vec{k}_T) = 4C_F\, \theta(q_T^{\text{cut}} - \mathcal{T}_{\text{cut}}) \left[-2 \ln^2 \frac{\mathcal{T}_{\text{cut}}}{q_T^{\text{cut}}}\right], \tag{B.39}$$

where the dependence on μ drops out as expected. Inserting eq. (B.38) and integrating by parts also yields the cumulant up to $\mathcal{T}_{\text{cut}} > 0$ in position space,

$$\int^{\mathcal{T}_{\text{cut}}} \mathrm{d}k\, \Delta \tilde{S}_{i,1}(k, b_T) = 4C_F \left[\frac{1}{4} x^2\, {}_3F_4\left(1, 1, 1; 2, 2, 2, 2; -\frac{x^2}{4}\right) - 2 \ln^2 \frac{x e^{\gamma_E}}{2}\right], \tag{B.40}$$

where $x \equiv b_T \mathcal{T}_{\text{cut}}$ and ${}_iF_j(x_1, \ldots, x_i; y_1, \ldots, y_j; z)$ is the generalized hypergeometric function. The right hand side of eq. (B.40) asymptotes to $1/x^2$ as $x \to \infty$, as required by the scaling law in eq. (B.36). We also need the spectrum of $\Delta \tilde{S}_{i,1}$ at $\mathcal{T} > 0$ in position space,

$$\Delta \tilde{S}_{i,1}(\mathcal{T}, b_T) = 4C_F \frac{1}{\mathcal{T}} \left[\frac{1}{2} x^2\, {}_2F_3\left(1, 1; 2, 2, 2; -\frac{x^2}{4}\right) - 4 \ln \frac{x e^{\gamma_E}}{2}\right], \tag{B.41}$$

where this time $x \equiv b_T \mathcal{T}$ and the term in square brackets again asymptotes to $1/x^2$ as $x \to \infty$.

JHEP03(2019)124

B.3 Renormalization-group evolution

SCET$_{\rm I}$. The closed-form solution of eq. (B.11) is [64, 104]

$$B_q(t,x,\vec{k}_T,\mu) = \exp\Big[4K^q_\Gamma(\mu_B,\mu) + K^q_{\gamma_B}(\mu_B,\mu)\Big] \times \int \mathrm{d}t'\, \mathcal{V}_{-2\eta^q_\Gamma(\mu_B,\mu)}(t-t',\mu_B^2)\, B_q(t',x,\vec{k}_T,\mu_B)\,, \tag{B.42}$$

where $\mathcal{V}_\eta$ was defined in eq. (A.5). Similarly, the solution of eq. (B.16) is

$$S_i(k,\mu) = \exp\Big[-4K^i_\Gamma(\mu_S,\mu) + K^i_{\gamma_S}(\mu_S,\mu)\Big] \int \mathrm{d}k'\, \mathcal{V}_{4\eta^i_\Gamma(\mu_S,\mu)}(k-k',\mu_S)\, S_i(k',\mu_S)\,. \tag{B.43}$$

The definitions of η^i_Γ, K^i_Γ, and K_γ and their approximate analytical form at NNLL are given for example in appendix A.4 of ref. [105]. The solution of the hard RGE in eq. (B.7) in our notation is also found there.

SCET$_{\rm II}$. Evolving first in ν and then in μ (from right to left), the solution of eq. (B.9) is

$$\tilde{B}_q(\omega,b_T,\mu,\nu) = \exp\left[2\eta^q_\Gamma(\mu_B,\mu)\ln\frac{\nu}{\omega} + K^q_{\tilde{\gamma}_B}(\mu_B,\mu)\right] \times \exp\left[-\frac{1}{2}\ln\frac{\nu}{\nu_B}\,\tilde{\gamma}^q_\nu(b_T,\mu_B)\right]\, \tilde{B}_q(\omega,b_T,\mu_B,\nu_B)\,, \tag{B.44}$$

where the resummed rapidity anomalous dimension $\tilde{\gamma}^q_\nu(b_T,\mu_B)$ is given by eq. (2.26). For the double-differential soft function renormalized as in eq. (B.17), we have

$$\tilde{S}_i(k,b_T,\mu,\nu) = \exp\left[-4\eta^i_\Gamma(\mu_S,\mu)\ln\frac{\nu}{\mu_S} + 4K^i_\Gamma(\mu_S,\mu) + K^i_{\tilde{\gamma}_S}(\mu_S,\mu)\right] \times \exp\left[\ln\frac{\nu}{\nu_S}\,\tilde{\gamma}^i_\nu(b_T,\mu_S)\right]\, \tilde{S}_i(k,b_T,\mu_S,\nu_S)\,. \tag{B.45}$$

SCET$_{+}$. Again evolving first in ν and then in μ, the solution of the collinear-soft RGE in eq. (B.18) in b_T space is given by

$$\tilde{\mathcal{S}}_i(k,b_T,\mu,\nu) = \exp\Big[4K^i_\Gamma(\mu_{\mathcal{S}},\mu) + K^i_{\gamma_{\mathcal{S}}}(\mu_{\mathcal{S}},\mu)\Big] \int \mathrm{d}k'\, \mathcal{V}_{-2\eta^i_\Gamma(\mu_{\mathcal{S}},\mu)}\left(k-k',\frac{\mu_{\mathcal{S}}^2}{\nu}\right) \times \exp\left[\frac{1}{2}\ln\frac{\nu}{\nu_{\mathcal{S}}}\,\tilde{\gamma}^i_\nu(b_T,\mu_{\mathcal{S}})\right]\, \tilde{\mathcal{S}}_i(k',b_T,\mu_{\mathcal{S}},\nu_{\mathcal{S}})\,. \tag{B.46}$$

The rapidity evolution factor on the second line does not depend on k' and thus may be taken out of the convolution integral.

B.4 Beam function convolutions with RG kernels

In SCET$_{\rm I}$ the combined beam and soft renormalization group running in momentum space has the functional form $\mathcal{V}_\eta(k,\mu)$ [see eq. (A.5)], where the convolution variable k is ultimately fixed by the overall $\mathcal{T}$ measurement. To evaluate the resummed SCET$_{\rm I}$ cross section as a function of $\mathcal{T}$ ($\mathcal{T}_{\rm cut}$) we require convolutions of $\mathcal{V}_\eta$ with the double-differential

JHEP03(2019)124

beam function at finite $\mathcal{T}$ (integrated up to $\mathcal{T}_{\rm cut}$). Convolutions of $\mathcal{V}_\eta$ with the inclusive beam function reduce to a linear combination of

$$Q_i \int \mathrm{d}k'\, \mathcal{V}_\eta(k-k',\mu)\, \mathcal{L}_n(Q_i k',\mu^2) = \int \mathrm{d}k'\, \mathcal{V}_\eta(k-k',\mu)\, \mathcal{L}_n\left(k',\frac{\mu^2}{Q_i}\right), \tag{B.47}$$

with Q_i as in eq. (2.1), and are straightforward to evaluate using results in appendix B of ref. [64]. The same is true for convolutions of the evolution kernel with the single-differential $\mathcal{T}$ soft function and, in SCET$_+$, with the collinear-soft function. (Cross terms between beam, csoft, or soft functions are absent at one loop.) The only nontrivial ingredient are convolutions of $\mathcal{V}_\eta(k,\mu)$ with the one-loop $\Delta I^{(1)}_{qj}$ piece defined in eq. (B.29). Depending on the measurement, we distinguish the following four cases for the resulting Mellin kernel:

1. cumulant up to $\mathcal{T}_{\rm cut} > 0$, cumulant up to $q_T^{\rm cut} > 0$, $r \equiv (q_T^{\rm cut})^2/(Q_i \mathcal{T}_{\rm cut})$:

$$\begin{aligned} &Q_i \int \mathrm{d}k \int \mathrm{d}^2\vec{k}_T\, \theta(\mathcal{T}_{\rm cut}-k)\, \theta(q_T^{\rm cut}-|\vec{k}_T|) \int \mathrm{d}k'\, \mathcal{V}_\eta(k-k',\mathcal{T}_{\rm cut})\, \Delta I^{(1)}_{qj}(Q_i k',z,\vec{k}_T) \\ &= \theta\Big(r > \frac{1-z}{z}\Big) P^{(0)}_{qj}(z)\, \frac{e^{-\gamma_E \eta}}{\Gamma(1+\eta)} \Big[-B_{1-rz/(1-z)}(1+\eta,0)\Big], \end{aligned} \tag{B.48}$$

   where $B_x(a,b)$ is the incomplete Beta function,

$$B_x(a,b) = \int_0^x \mathrm{d}t\, t^{a-1}(1-t)^{b-1}. \tag{B.49}$$

2. spectrum at $\mathcal{T} > 0$, cumulant up to $q_T^{\rm cut} > 0$, $r \equiv (q_T^{\rm cut})^2/(Q_i \mathcal{T})$:

$$\begin{aligned} &Q_i \int \mathrm{d}k \int \mathrm{d}^2\vec{k}_T\, \delta(\mathcal{T}-k)\, \theta(q_T^{\rm cut}-|\vec{k}_T|) \int \mathrm{d}k'\, \mathcal{V}_\eta(k-k',\mathcal{T})\, \Delta I^{(1)}_{qj}(Q_i k',z,\vec{k}_T) \\ &= \frac{1}{\mathcal{T}}\, \theta\Big(r > \frac{1-z}{z}\Big) P^{(0)}_{qj}(z)\, \frac{e^{-\gamma_E \eta}}{\Gamma(1+\eta)} \Big[-\eta B_{1-rz/(1-z)}(1+\eta,0) - \Big(1-\frac{rz}{1-z}\Big)^\eta\Big]. \end{aligned} \tag{B.50}$$

3. cumulant up to $\mathcal{T}_{\rm cut}$, spectrum at $q_T > 0$, $r \equiv (q_T)^2/(Q_i \mathcal{T}_{\rm cut})$:

$$\begin{aligned} &Q_i \int \mathrm{d}k \int \mathrm{d}^2\vec{k}_T\, \theta(\mathcal{T}_{\rm cut}-k)\, \delta(q_T-|\vec{k}_T|) \int \mathrm{d}k'\, \mathcal{V}_\eta(k-k',\mathcal{T}_{\rm cut})\, \Delta I^{(1)}_{qj}(Q_i k',z,\vec{k}_T) \\ &= \frac{2}{q_T}\, \theta\Big(r > \frac{1-z}{z}\Big) P^{(0)}_{qj}(z)\, \frac{e^{-\gamma_E \eta}}{\Gamma(1+\eta)} \Big(1-\frac{rz}{1-z}\Big)^\eta. \end{aligned} \tag{B.51}$$

4. spectrum at $\mathcal{T} > 0$, spectrum at $q_T > 0$, $r \equiv (q_T)^2/(Q_i \mathcal{T})$:

$$\begin{aligned} &Q_i \int \mathrm{d}k \int \mathrm{d}^2\vec{k}_T\, \delta(\mathcal{T}-k)\, \delta(q_T-|\vec{k}_T|) \int \mathrm{d}k'\, \mathcal{V}_\eta(k-k',\mathcal{T})\, \Delta I^{(1)}_{qj}(Q_i k',z,\vec{k}_T) \\ &= \frac{2}{q_T}\frac{1}{\mathcal{T}}\, P^{(0)}_{qj}(z)\, \mathcal{V}_\eta\Big(1-\frac{rz}{1-z}\Big) \end{aligned} \tag{B.52}$$

In the first three cases the overall θ function cuts off the final PDF integral at

$$z < z_{\rm cut} \equiv \frac{1}{1+r}, \tag{B.53}$$

JHEP03(2019)124

and the Mellin kernel is regular up to and including z_{cut}. In the last case we instead find a singularity at $z = z_{\text{cut}}$, i.e., the subtraction from $\mathcal{V}_\eta$ now acts directly on the PDF integral. In either case we have exploited that terms proportional to $\delta(1-z)$ are cut off since $r > 0$, so we could replace $\tilde{P}_{qj}^{(0)}$ by $P_{qj}^{(0)}$ throughout. We have also set $\mu = \mathcal{T}\,(\mathcal{T}_{\text{cut}})$ in the boundary condition of $\mathcal{V}_\eta$ on the left-hand side, which can always be achieved by a shift in μ. This ensures that the right-hand side depends only on the dimensionless parameters r and η, up to an overall dimensionful prefactor. It is straightforward to check that for $\eta \to 0$ (at fixed order), the above results reduce to cumulants (spectra) of $\Delta I_{qj}^{(1)}$ itself.

JHEP03(2019)124

References

[1] T. Sjöstrand, S. Mrenna and P.Z. Skands, *PYTHIA 6.4 Physics and Manual*, *JHEP* **05** (2006) 026 [hep-ph/0603175] [INSPIRE].

[2] T. Sjöstrand et al., *An Introduction to PYTHIA 8.2*, *Comput. Phys. Commun.* **191** (2015) 159 [arXiv:1410.3012] [INSPIRE].

[3] M. Bahr et al., *HERWIG++ Physics and Manual*, *Eur. Phys. J.* **C 58** (2008) 639 [arXiv:0803.0883] [INSPIRE].

[4] J. Bellm et al., *HERWIG 7.0/HERWIG++ 3.0 release note*, *Eur. Phys. J.* **C 76** (2016) 196 [arXiv:1512.01178] [INSPIRE].

[5] T. Gleisberg et al., *Event generation with SHERPA 1.1*, *JHEP* **02** (2009) 007 [arXiv:0811.4622] [INSPIRE].

[6] M. Dasgupta, F.A. Dreyer, K. Hamilton, P.F. Monni and G.P. Salam, *Logarithmic accuracy of parton showers: a fixed-order study*, *JHEP* **09** (2018) 033 [arXiv:1805.09327] [INSPIRE].

[7] J.C. Collins, D.E. Soper and G.F. Sterman, *Factorization for Short Distance Hadron-Hadron Scattering*, *Nucl. Phys.* **B 261** (1985) 104 [INSPIRE].

[8] J.C. Collins, D.E. Soper and G.F. Sterman, *Soft Gluons and Factorization*, *Nucl. Phys.* **B 308** (1988) 833 [INSPIRE].

[9] J.C. Collins, D.E. Soper and G.F. Sterman, *Factorization of Hard Processes in QCD*, *Adv. Ser. Direct. High Energy Phys.* **5** (1989) 1 [hep-ph/0409313] [INSPIRE].

[10] A. Banfi, G.P. Salam and G. Zanderighi, *Semi-numerical resummation of event shapes*, *JHEP* **01** (2002) 018 [hep-ph/0112156] [INSPIRE].

[11] A. Banfi, G.P. Salam and G. Zanderighi, *Principles of general final-state resummation and automated implementation*, *JHEP* **03** (2005) 073 [hep-ph/0407286] [INSPIRE].

[12] A. Banfi, H. McAslan, P.F. Monni and G. Zanderighi, *A general method for the resummation of event-shape distributions in e^+e^- annihilation*, *JHEP* **05** (2015) 102 [arXiv:1412.2126] [INSPIRE].

[13] W. Bizon, P.F. Monni, E. Re, L. Rottoli and P. Torrielli, *Momentum-space resummation for transverse observables and the Higgs $p_\perp$ at $N^3LL + NNLO$*, *JHEP* **02** (2018) 108 [arXiv:1705.09127] [INSPIRE].

[14] C.W. Bauer, S. Fleming and M.E. Luke, *Summing Sudakov logarithms in $B \to X_s\gamma$ in effective field theory*, *Phys. Rev.* **D 63** (2000) 014006 [hep-ph/0005275] [INSPIRE].

[15] C.W. Bauer, S. Fleming, D. Pirjol and I.W. Stewart, *An Effective field theory for collinear and soft gluons: Heavy to light decays*, *Phys. Rev.* **D 63** (2001) 114020 [hep-ph/0011336] [INSPIRE].

[16] C.W. Bauer and I.W. Stewart, *Invariant operators in collinear effective theory*, *Phys. Lett.* **B 516** (2001) 134 [hep-ph/0107001] [INSPIRE].

[17] C.W. Bauer, D. Pirjol and I.W. Stewart, *Soft collinear factorization in effective field theory*, *Phys. Rev.* **D 65** (2002) 054022 [hep-ph/0109045] [INSPIRE].

[18] C.W. Bauer, S. Fleming, D. Pirjol, I.Z. Rothstein and I.W. Stewart, *Hard scattering factorization from effective field theory*, *Phys. Rev.* **D 66** (2002) 014017 [hep-ph/0202088] [INSPIRE].

[19] M. Beneke, A.P. Chapovsky, M. Diehl and T. Feldmann, *Soft collinear effective theory and heavy to light currents beyond leading power*, *Nucl. Phys.* **B 643** (2002) 431 [hep-ph/0206152] [INSPIRE].

[20] H.-n. Li, *Unification of the k_T and threshold resummations*, *Phys. Lett.* **B 454** (1999) 328 [hep-ph/9812363] [INSPIRE].

[21] E. Laenen, G.F. Sterman and W. Vogelsang, *Recoil and threshold corrections in short distance cross-sections*, *Phys. Rev.* **D 63** (2001) 114018 [hep-ph/0010080] [INSPIRE].

[22] A. Kulesza, G.F. Sterman and W. Vogelsang, *Joint resummation in electroweak boson production*, *Phys. Rev.* **D 66** (2002) 014011 [hep-ph/0202251] [INSPIRE].

[23] A. Kulesza, G.F. Sterman and W. Vogelsang, *Joint resummation for Higgs production*, *Phys. Rev.* **D 69** (2004) 014012 [hep-ph/0309264] [INSPIRE].

[24] G. Lustermans, W.J. Waalewijn and L. Zeune, *Joint transverse momentum and threshold resummation beyond NLL*, *Phys. Lett.* **B 762** (2016) 447 [arXiv:1605.02740] [INSPIRE].

[25] S. Marzani and V. Theeuwes, *Vector boson production in joint resummation*, *JHEP* **02** (2017) 127 [arXiv:1612.01432] [INSPIRE].

[26] C. Muselli, S. Forte and G. Ridolfi, *Combined threshold and transverse momentum resummation for inclusive observables*, *JHEP* **03** (2017) 106 [arXiv:1701.01464] [INSPIRE].

[27] S. Marzani, *Combining Q_T and small-x resummations*, *Phys. Rev.* **D 93** (2016) 054047 [arXiv:1511.06039] [INSPIRE].

[28] C.W. Bauer, F.J. Tackmann, J.R. Walsh and S. Zuberi, *Factorization and Resummation for Dijet Invariant Mass Spectra*, *Phys. Rev.* **D 85** (2012) 074006 [arXiv:1106.6047] [INSPIRE].

[29] P. Pietrulewicz, F.J. Tackmann and W.J. Waalewijn, *Factorization and Resummation for Generic Hierarchies between Jets*, *JHEP* **08** (2016) 002 [arXiv:1601.05088] [INSPIRE].

[30] A.J. Larkoski, I. Moult and D. Neill, *Toward Multi-Differential Cross Sections: Measuring Two Angularities on a Single Jet*, *JHEP* **09** (2014) 046 [arXiv:1401.4458] [INSPIRE].

[31] M. Procura, W.J. Waalewijn and L. Zeune, *Joint resummation of two angularities at next-to-next-to-leading logarithmic order*, *JHEP* **10** (2018) 098 [arXiv:1806.10622] [INSPIRE].

[32] D.W. Kolodrubetz, P. Pietrulewicz, I.W. Stewart, F.J. Tackmann and W.J. Waalewijn, *Factorization for Jet Radius Logarithms in Jet Mass Spectra at the LHC*, *JHEP* **12** (2016) 054 [arXiv:1605.08038] [INSPIRE].

JHEP03(2019)124

[33] A. Hornig, D. Kang, Y. Makris and T. Mehen, *Transverse Vetoes with Rapidity Cutoff in SCET*, *JHEP* **12** (2017) 043 [arXiv:1708.08467] [INSPIRE].

[34] J.K.L. Michel, P. Pietrulewicz and F.J. Tackmann, *Jet Veto Resummation with Jet Rapidity Cuts*, arXiv:1810.12911 [INSPIRE].

[35] X. Liu, S.-O. Moch and F. Ringer, *Threshold and jet radius joint resummation for single-inclusive jet production*, *Phys. Rev. Lett.* **119** (2017) 212001 [arXiv:1708.04641] [INSPIRE].

[36] X. Liu, S.-O. Moch and F. Ringer, *Phenomenology of single-inclusive jet production with jet radius and threshold resummation*, *Phys. Rev.* **D 97** (2018) 056026 [arXiv:1801.07284] [INSPIRE].

[37] S. Fleming, A.H. Hoang, S. Mantry and I.W. Stewart, *Jets from massive unstable particles: Top-mass determination*, *Phys. Rev.* **D 77** (2008) 074010 [hep-ph/0703207] [INSPIRE].

[38] T.T. Jouttenus, I.W. Stewart, F.J. Tackmann and W.J. Waalewijn, *The Soft Function for Exclusive N-Jet Production at Hadron Colliders*, *Phys. Rev.* **D 83** (2011) 114030 [arXiv:1102.4344] [INSPIRE].

[39] D. Bertolini et al., *Soft Functions for Generic Jet Algorithms and Observables at Hadron Colliders*, *JHEP* **07** (2017) 099 [arXiv:1704.08262] [INSPIRE].

[40] M. Dasgupta and G.P. Salam, *Resummation of nonglobal QCD observables*, *Phys. Lett.* **B 512** (2001) 323 [hep-ph/0104277] [INSPIRE].

[41] A. Banfi, G. Marchesini and G. Smye, *Away from jet energy flow*, *JHEP* **08** (2002) 006 [hep-ph/0206076] [INSPIRE].

[42] Y. Hatta and T. Ueda, *Resummation of non-global logarithms at finite N_c*, *Nucl. Phys.* **B 874** (2013) 808 [arXiv:1304.6930] [INSPIRE].

[43] A.J. Larkoski, I. Moult and D. Neill, *Non-Global Logarithms, Factorization and the Soft Substructure of Jets*, *JHEP* **09** (2015) 143 [arXiv:1501.04596] [INSPIRE].

[44] S. Caron-Huot, *Resummation of non-global logarithms and the BFKL equation*, *JHEP* **03** (2018) 036 [arXiv:1501.03754] [INSPIRE].

[45] T. Becher, M. Neubert, L. Rothen and D.Y. Shao, *Effective Field Theory for Jet Processes*, *Phys. Rev. Lett.* **116** (2016) 192001 [arXiv:1508.06645] [INSPIRE].

[46] I.W. Stewart, F.J. Tackmann and W.J. Waalewijn, *Factorization at the LHC: From PDFs to Initial State Jets*, *Phys. Rev.* **D 81** (2010) 094035 [arXiv:0910.0467] [INSPIRE].

[47] I.W. Stewart, F.J. Tackmann and W.J. Waalewijn, *N-Jettiness: An Inclusive Event Shape to Veto Jets*, *Phys. Rev. Lett.* **105** (2010) 092002 [arXiv:1004.2489] [INSPIRE].

[48] ATLAS collaboration, *Measurement of event-shape observables in $Z \to \ell^+\ell^-$ events in pp collisions at $\sqrt{s} = 7$ TeV with the ATLAS detector at the LHC*, *Eur. Phys. J.* **C 76** (2016) 375 [arXiv:1602.08980] [INSPIRE].

[49] S. Alioli et al., *Combining Higher-Order Resummation with Multiple NLO Calculations and Parton Showers in GENEVA*, *JHEP* **09** (2013) 120 [arXiv:1211.7049] [INSPIRE].

[50] S. Alioli, C.W. Bauer, C. Berggren, F.J. Tackmann and J.R. Walsh, *Drell-Yan production at $NNLL' + NNLO$ matched to parton showers*, *Phys. Rev.* **D 92** (2015) 094020 [arXiv:1508.01475] [INSPIRE].

[51] M. Procura, W.J. Waalewijn and L. Zeune, *Resummation of Double-Differential Cross Sections and Fully-Unintegrated Parton Distribution Functions*, *JHEP* **02** (2015) 117 [arXiv:1410.6483] [INSPIRE].

JHEP03(2019)124

[52] J.R. Gaunt and M. Stahlhofen, *The Fully-Differential Quark Beam Function at NNLO*, *JHEP* **12** (2014) 146 [arXiv:1409.8281] [INSPIRE].

[53] I.W. Stewart, F.J. Tackmann and W.J. Waalewijn, *The Beam Thrust Cross Section for Drell-Yan at NNLL Order*, *Phys. Rev. Lett.* **106** (2011) 032001 [arXiv:1005.4060] [INSPIRE].

[54] M.A. Ebert et al., *SCETlib: A C++ Package for Numerical Calculations in QCD and Soft-Collinear Effective Theory*, DESY-17-099 (2018).

[55] J.M. Campbell and R.K. Ellis, *An Update on vector boson pair production at hadron colliders*, *Phys. Rev.* **D 60** (1999) 113006 [hep-ph/9905386] [INSPIRE].

[56] J.M. Campbell, R.K. Ellis and C. Williams, *Vector boson pair production at the LHC*, *JHEP* **07** (2011) 018 [arXiv:1105.0020] [INSPIRE].

[57] J.M. Campbell, R.K. Ellis and W.T. Giele, *A Multi-Threaded Version of MCFM*, *Eur. Phys. J.* **C 75** (2015) 246 [arXiv:1503.06182] [INSPIRE].

[58] L.A. Harland-Lang, A.D. Martin, P. Motylinski and R.S. Thorne, *Parton distributions in the LHC era: MMHT 2014 PDFs*, *Eur. Phys. J.* **C 75** (2015) 204 [arXiv:1412.3989] [INSPIRE].

[59] A. Jain, M. Procura and W.J. Waalewijn, *Fully-Unintegrated Parton Distribution and Fragmentation Functions at Perturbative k_T*, *JHEP* **04** (2012) 132 [arXiv:1110.0839] [INSPIRE].

[60] I.W. Stewart, F.J. Tackmann and W.J. Waalewijn, *The Quark Beam Function at NNLL*, *JHEP* **09** (2010) 005 [arXiv:1002.2213] [INSPIRE].

[61] J.R. Gaunt, *Glauber Gluons and Multiple Parton Interactions*, *JHEP* **07** (2014) 110 [arXiv:1405.2080] [INSPIRE].

[62] M. Zeng, *Drell-Yan process with jet vetoes: breaking of generalized factorization*, *JHEP* **10** (2015) 189 [arXiv:1507.01652] [INSPIRE].

[63] I.Z. Rothstein and I.W. Stewart, *An Effective Field Theory for Forward Scattering and Factorization Violation*, *JHEP* **08** (2016) 025 [arXiv:1601.04695] [INSPIRE].

[64] Z. Ligeti, I.W. Stewart and F.J. Tackmann, *Treating the b quark distribution function with reliable uncertainties*, *Phys. Rev.* **D 78** (2008) 114014 [arXiv:0807.1926] [INSPIRE].

[65] R. Abbate, M. Fickinger, A.H. Hoang, V. Mateu and I.W. Stewart, *Thrust at N^3LL with Power Corrections and a Precision Global Fit for $\alpha_s(m_Z)$*, *Phys. Rev.* **D 83** (2011) 074021 [arXiv:1006.3080] [INSPIRE].

[66] S. Gangal, M. Stahlhofen and F.J. Tackmann, *Rapidity-Dependent Jet Vetoes*, *Phys. Rev.* **D 91** (2015) 054023 [arXiv:1412.4792] [INSPIRE].

[67] I.W. Stewart, F.J. Tackmann, J.R. Walsh and S. Zuberi, *Jet p_T resummation in Higgs production at $NNLL' + NNLO$*, *Phys. Rev.* **D 89** (2014) 054001 [arXiv:1307.1808] [INSPIRE].

[68] J.-y. Chiu, A. Jain, D. Neill and I.Z. Rothstein, *The Rapidity Renormalization Group*, *Phys. Rev. Lett.* **108** (2012) 151601 [arXiv:1104.0881] [INSPIRE].

[69] J.-Y. Chiu, A. Jain, D. Neill and I.Z. Rothstein, *A Formalism for the Systematic Treatment of Rapidity Logarithms in Quantum Field Theory*, *JHEP* **05** (2012) 084 [arXiv:1202.0814] [INSPIRE].

[70] T. Lübbert, J. Oredsson and M. Stahlhofen, *Rapidity renormalized TMD soft and beam functions at two loops*, *JHEP* **03** (2016) 168 [arXiv:1602.01829] [INSPIRE].

JHEP03(2019)124

[71] J.C. Collins and D.E. Soper, *Parton Distribution and Decay Functions*, *Nucl. Phys.* **B 194** (1982) 445 [INSPIRE].

[72] J.C. Collins, D.E. Soper and G.F. Sterman, *Transverse Momentum Distribution in Drell-Yan Pair and W and Z Boson Production*, *Nucl. Phys.* **B 250** (1985) 199 [INSPIRE].

[73] T. Becher and M. Neubert, *Drell-Yan Production at Small q_T, Transverse Parton Distributions and the Collinear Anomaly*, *Eur. Phys. J.* **C 71** (2011) 1665 [arXiv:1007.4005] [INSPIRE].

[74] M.G. Echevarria, A. Idilbi and I. Scimemi, *Factorization Theorem For Drell-Yan At Low q_T And Transverse Momentum Distributions On-The-Light-Cone*, *JHEP* **07** (2012) 002 [arXiv:1111.4996] [INSPIRE].

[75] S. Frixione, P. Nason and G. Ridolfi, *Problems in the resummation of soft gluon effects in the transverse momentum distributions of massive vector bosons in hadronic collisions*, *Nucl. Phys.* **B 542** (1999) 311 [hep-ph/9809367] [INSPIRE].

[76] P.F. Monni, E. Re and P. Torrielli, *Higgs Transverse-Momentum Resummation in Direct Space*, *Phys. Rev. Lett.* **116** (2016) 242001 [arXiv:1604.02191] [INSPIRE].

[77] M.A. Ebert and F.J. Tackmann, *Resummation of Transverse Momentum Distributions in Distribution Space*, *JHEP* **02** (2017) 110 [arXiv:1611.08610] [INSPIRE].

[78] G. Parisi and R. Petronzio, *Small Transverse Momentum Distributions in Hard Processes*, *Nucl. Phys.* **B 154** (1979) 427 [INSPIRE].

[79] J.C. Collins and D.E. Soper, *Back-To-Back Jets in QCD*, *Nucl. Phys.* **B 193** (1981) 381 [*Erratum ibid.* **B 213** (1983) 545] [INSPIRE].

[80] J.C. Collins and D.E. Soper, *Back-To-Back Jets: Fourier Transform from B to K-Transverse*, *Nucl. Phys.* **B 197** (1982) 446 [INSPIRE].

[81] M.A. Ebert, I.W. Stewart and Y. Zhao, *Determining the Nonperturbative Collins-Soper Kernel From Lattice QCD*, *Phys. Rev.* **D 99** (2019) 034505 [arXiv:1811.00026] [INSPIRE].

[82] D. Neill, I.Z. Rothstein and V. Vaidya, *The Higgs Transverse Momentum Distribution at NNLL and its Theoretical Errors*, *JHEP* **12** (2015) 097 [arXiv:1503.00005] [INSPIRE].

[83] U. D'Alesio, M.G. Echevarria, S. Melis and I. Scimemi, *Non-perturbative QCD effects in q_T spectra of Drell-Yan and Z-boson production*, *JHEP* **11** (2014) 098 [arXiv:1407.3311] [INSPIRE].

[84] A.V. Manohar, T. Mehen, D. Pirjol and I.W. Stewart, *Reparameterization invariance for collinear operators*, *Phys. Lett.* **B 539** (2002) 59 [hep-ph/0204229] [INSPIRE].

[85] C. Marcantonini and I.W. Stewart, *Reparameterization Invariant Collinear Operators*, *Phys. Rev.* **D 79** (2009) 065028 [arXiv:0809.1093] [INSPIRE].

[86] P.V. Landshoff and J.C. Polkinghorne, *Calorimeter Triggers for Hard Collisions*, *Phys. Rev.* **D 18** (1978) 3344 [INSPIRE].

[87] C. Goebel, F. Halzen and D.M. Scott, *Double Drell-Yan Annihilations in Hadron Collisions: Novel Tests of the Constituent Picture*, *Phys. Rev.* **D 22** (1980) 2789 [INSPIRE].

[88] F. Takagi, *Multiple Production of Quark Jets Off Nuclei*, *Phys. Rev. Lett.* **43** (1979) 1296 [INSPIRE].

[89] H.D. Politzer, *Power Corrections at Short Distances*, *Nucl. Phys.* **B 172** (1980) 349 [INSPIRE].

JHEP03(2019)124

[90] J. Gaunt, M. Stahlhofen, F.J. Tackmann and J.R. Walsh, *N-jettiness Subtractions for NNLO QCD Calculations*, *JHEP* **09** (2015) 058 [arXiv:1505.04794] [INSPIRE].

[91] L.G. Almeida, S.D. Ellis, C. Lee, G. Sterman, I. Sung and J.R. Walsh, *Comparing and counting logs in direct and effective methods of QCD resummation*, *JHEP* **04** (2014) 174 [arXiv:1401.4460] [INSPIRE].

[92] D. Bertolini, M.P. Solon and J.R. Walsh, *Integrated and Differential Accuracy in Resummed Cross Sections*, *Phys. Rev.* **D 95** (2017) 054024 [arXiv:1701.07919] [INSPIRE].

[93] O.V. Tarasov, A.A. Vladimirov and A. Yu. Zharkov, *The Gell-Mann-Low Function of QCD in the Three Loop Approximation*, *Phys. Lett.* **93B** (1980) 429 [INSPIRE].

[94] S.A. Larin and J.A.M. Vermaseren, *The Three loop QCD β-function and anomalous dimensions*, *Phys. Lett.* **B 303** (1993) 334 [hep-ph/9302208] [INSPIRE].

[95] G.P. Korchemsky and A.V. Radyushkin, *Renormalization of the Wilson Loops Beyond the Leading Order*, *Nucl. Phys.* **B 283** (1987) 342 [INSPIRE].

[96] S. Moch, J.A.M. Vermaseren and A. Vogt, *The Three loop splitting functions in QCD: The Nonsinglet case*, *Nucl. Phys.* **B 688** (2004) 101 [hep-ph/0403192] [INSPIRE].

[97] A. Vogt, S. Moch and J.A.M. Vermaseren, *The Three-loop splitting functions in QCD: The Singlet case*, *Nucl. Phys.* **B 691** (2004) 129 [hep-ph/0404111] [INSPIRE].

[98] J.R. Gaunt, M. Stahlhofen and F.J. Tackmann, *The Quark Beam Function at Two Loops*, *JHEP* **04** (2014) 113 [arXiv:1401.5478] [INSPIRE].

[99] A.V. Manohar, *Deep inelastic scattering as $x \to 1$ using soft collinear effective theory*, *Phys. Rev.* **D 68** (2003) 114019 [hep-ph/0309176] [INSPIRE].

[100] C.W. Bauer, C. Lee, A.V. Manohar and M.B. Wise, *Enhanced nonperturbative effects in Z decays to hadrons*, *Phys. Rev.* **D 70** (2004) 034014 [hep-ph/0309278] [INSPIRE].

[101] M. Ritzmann and W.J. Waalewijn, *Fragmentation in Jets at NNLO*, *Phys. Rev.* **D 90** (2014) 054029 [arXiv:1407.3272] [INSPIRE].

[102] S. Mantry and F. Petriello, *Transverse Momentum Distributions from Effective Field Theory with Numerical Results*, *Phys. Rev.* **D 83** (2011) 053007 [arXiv:1007.3773] [INSPIRE].

[103] M.D. Schwartz, *Resummation and NLO matching of event shapes with effective field theory*, *Phys. Rev.* **D 77** (2008) 014026 [arXiv:0709.2709] [INSPIRE].

[104] S. Fleming, A.H. Hoang, S. Mantry and I.W. Stewart, *Top Jets in the Peak Region: Factorization Analysis with NLL Resummation*, *Phys. Rev.* **D 77** (2008) 114003 [arXiv:0711.2079] [INSPIRE].

[105] M.A. Ebert, J.K.L. Michel and F.J. Tackmann, *Resummation Improved Rapidity Spectrum for Gluon Fusion Higgs Production*, *JHEP* **05** (2017) 088 [arXiv:1702.00794] [INSPIRE].

JHEP03(2019)124